From the Institute of Biochemistry

of the University of Lübeck

Director: Prof. Dr. rer. nat. Dr. h.c. Rolf Hilgenfeld

Structural Studies of Hypusination

Dissertation

in Fulfillment of

Requirements

for the Doctoral Degree

of the University of Lübeck

From the Department of Natural Sciences

Submitted by

Zhenggang Han

from Wei-nan, China

Lübeck, 2015

First referee: Prof. Dr. Rolf Hilgenfeld

Second referee: Prof. Dr. Thomas Peters

Date of oral examination: 22.07.2015

Approved for printing. Lübeck, 27.07.2015

TABLE OF CONTENTS

1. Introduction ……1

1.1 Eukaryotic translation initiation factor 5A……1

1.1.1 Structure of eIF-5A……....1

1.1.2 eIF-5A isoforms: eIF5-A1 and eIF-5A2…….....3

1.1.3 Oligomeric state of eIF-5A……4

1.1.4 Posttranslational modification of eIF-5A: hypusination……5

1.1.5 eIF-5A, a bimodular protein…….……8

1.1.6 Functions of eIF-5A……..…….9

1.1.6.1 Protein synthesis……..…...10

1.1.6.2 eIF-5A and cancer……..….....13

1.1.6.3 eIF-5A and RNA nucleocytoplasmic export……...15

1.2 Deoxyhypusine synthase ……...17

1.2.1 Structure of DHS……17

1.2.2 Catalytic mechanism of DHS…….…19

1.2.3 The complex of DHS and eIF-5A precursor……..…….. 20

1.3 Deoxyhypusine hydroxylase…….……21

1.3.1 Overview of DOHH……..…21

1.3.2 Biochemical and structural properties of DOHH……..…..22

1.3.3 The active site of DOHH and the DOHH - Dhp-eIF-5A interaction…….……..….24

1.3.4 Diiron center and mechanism and of DOHH……..25

1.4 Objective and achievement of this thesis……28

2. Materials and Methods……....30

2.1. Materials…….……..…30

2.1.1 Equipments……..……...30

2.1.2 Consumables……..……..31

2.1.3 Chemicals…….…31

2.2. Methods……..32

2.2.1 Cloning……...32

2.2.2 Recombinant protein overexpression……35
2.2.3 Protein purification……..35
2.2.3.1 GST-tagged protein purification……..35
2.2.3.2 His-tagged protein purification……..……..36
2.2.4 Native electrophoresis……36
2.2.5 Atomic absorption spectra……37
2.2.6 UV/Vis spectra……..……..37
2.2.7 Mössbauer spectra……37
2.2.8 Crystallization, crystal optimization, diffraction data collection, structure determination, refinement, and validation……..38
2.2.8.1 hsDOHH……..……38
2.2.8.2 scDOHH……..…39
2.2.8.3 pvDOHH……..……40
2.2.8.4 eIF-5A2……41
2.2.8.5 DHS – eIF-5A1-N complex……...42
2.2.9 Density functional theory (DFT) calculations……..…42
2.2.10 Automated docking……..……...42
3. Results and Discussions……44
3.1 Human deoxyhypusine hydroxylase……44
3.1.1 His-tagged recombinant hsDOHH production and crystallization……..……..…44
3.1.2 GST-tagged recombinant hsDOHH production and crystallization……..……46
3.1.3 Spectroscopic studies of hsDOHH……..50
3.1.4 Structure determination and refinement……..54
3.1.5 Overall structure of hsDOHH……56
3.1.6 Diiron core of hsDOHH……....58
3.1.7 Density function theory study of hsDOHH……..…63
3.1.8 Secondary coordination sphere of diiron site in hsDOHH……...66
3.1.9 The substrate-binding cavity of hsDOHH……...68

3.1.10 A model for Dhp - eIF-5A binding to hsDOHH……..71
3.2 Yeast deoxyhypusine hydroxylase……74
3.2.1 Protein production and purification……...76
3.2.2 UV/Vis spectroscopy……..……77
3.2.3 scDOHH crystallization, crystal optimization, and structure determination……78
3.2.4 Overall structure of scDOHH……80
3.2.5 Diiron site of scDOHH……..…81
3.2.6 Secondary coordination sphere of scDOHH……...84
3.2.7 Substrate-binding pocket of scDOHH and scDOHH – Dhp-eIF5A interaction……....84
3.3 Structure of *Plasmodium* deoxyhypusine hydroxylase……...88
3.3.1 Recombinant *Plasmodium falciparum* DOHH production and crystallization……88
3.3.2 *Plasmodium vivax* production and crystallization……..90
3.3.3 Spectroscopic studies……92
3.3.4 Overall structure of pvDOHH……..……..93
3.3.5 Diiron site of pvDOHH……..…..…95
3.3.6 Secondary coordination sphere of pvDOHH……..97
3.3.7 Substrate-binding site of pvDOHH……..…..…98
3.4 Discussion of the DOHH results……...100
3.4.1 Non-heme diiron proteins: diverse functions and similar diiron-core topology…….....100
3.4.2 Nature of the peroxo-diiron(III) intermediate……103
3.4.3 Crystallographic studies of the peroxo-diiron(III) intermediate..107
3.4.4 Base of the extreme longevity of peroxo-diiron(III) intermediate in DOHH……....109
3.4.5 DOHH, an incomplete system……115
3.4.5.1 Resting state of DOHH……....116
3.4.5.2 Reduction system for DOHH……..117

3.4.5.3 High-oxidation state diiron species of DOHH……..118
3.5 Structure of human eukaryotic translation initiation factor 5A-2……..119
3.5.1 Crystallization and structure determination……...119
3.5.2 Structure of human eIF-5A2……121
3.5.3 Comparison of dimeric eIF-5A2 and eIF-5A1……...123
3.5.4 Comparison with other dimeric forms of eIF-5A
derived from crystal structures……126
3.5.5 Gel filtration analysis of recombinant human eIF-5A2
and eIF-5A1……..……127
3.5.6 Biological implications of the human eIF-5A dimer……....128
3.6 Purification and crystallization of the human DHS – eIF-5A
complex……..……..…130
3.6.1 Protein production……...130
3.6.2 The formation of the enzyme – substrate complex……....130
3.6.3 Purification of the DHS - eIF-5A1 complex……..…133
3.6.4 Crystallization of the DHS – eIF-5A1 complex……..……..134
4. Summary……..……..139
5. References…….……141
6. Acknowledgements……..……168

ABBREVIATIONS

ADO	aldehyde-deformylating oxygenase
ADP	adenosine diphosphate
aIF-5A	archaeal translation initiation factor 5A
AMD1	adenosylmethionine decarboxylase 1
AurF	*p*-aminobenzoate *N*-oxygenase
CRM1	chromosome region maintenance 1
DC	dendritic cell
Δ^9D	stearoyl-acyl carrier protein Δ^9-desaturase
DFT	density functional theory
Dhp	deoxyhypusine
DHS	deoxyhypusine synthase
DLS	dynamic light-scattering
DNA	deoxyribonucleic acid
DOHH	deoxyhypusine hydroxylase
eIF-5A	eukaryotic translation initiation factor 5A
eIF-5A1	eukaryotic translation initiation factor 5A isoform 1
eIF-5A2	eukaryotic translation initiation factor 5A isoform 2
EF-P	elongation factor P
fMet	N-formylmethionine
GLC	structure of human DOHH in complex with glycerol
GSH	glutathione
GST	glutathione S-transferases
HCC	hepatocellular carcinoma
HEAT	**H**untingtin, elongation factor 3 (**E**F3), protein phosphatase 2A (PP2**A**), and yeast kinase **T**OR1
Hpu	hypusine
Hr	hemerythrin
hsDOHH	human DOHH
ICP-MS	inductively coupled plasma-high resolution mass spectrometry
IFNα	interferon-α
kDa	kiloDalton
MALDI-TOF-MS	matrix-assisted laser desorption-ionization time-of-flight mass spectrometry
mRNA	messenger RNA
NAD^+	nicotinamide adenine dinucleotide (oxidized)
NADH	nicotinamide adenine dinucleotide (reduced)
NES	nuclear export signal
oxyHr	oxyhemerythrin
PCR	polymerase chain reaction
PDB	Protein Data Bank
pfDOHH	*Plasmodium falciparum* DOHH
POX	structure of human DOHH in peroxo intermediate

PTC	peptidyl transferase center
pvDOHH	*Plasmodium vivax* DOHH
QM/MM	quantum mechanics/molecular mechanics
RRE	Rev response element
RNA	ribonucleic acid
RNAi	RNA interference
RNR-R2	ribonucleotide reductase subunit R2
SAXS	small-angle X-ray scattering
scDOHH	*Saccharomyces cerevisiae* DOHH
SDS-PAGE	sodium dodecyl sulfate polyacrylamide gel electrophoresis
SELEX	systematic evolution of ligands by exponential enrichment
shRNA	short-hairpin RNAs
sMMO	soluble methane monooxygenase
sMMOH	soluble methane monooxygenase hydroxylase
snRNA	small nuclear RNA
T4moH	toluene 4-monooxygenase hydroxylase
ToMOH	toluene/o-xylene monooxygenase hydroxylase
tRNA	transfer RNA
tTG	tissue transglutaminase
vRNA	viral RNA
XPO4	exportin 4

1. Introduction

1.1 Eukaryotic translation initiation factor 5A

Eukaryotic translation initiation factor 5A (eIF-5A), formerly termed IF-M2Bα or eIF4D, is a ubiquitous protein of monomeric molecular mass around 18 kDa, which is present in archaea (where it is called aIF-5A) and eukaryotes but not in prokaryotes (Park, 2006). eIF-5A was initially isolated from rabbit reticulocyte ribosomes (Kemper *et al*., 1976; Schreier *et al*., 1977; Thomas *et al*., 1979). It was considered to be a translation initiation factor, since eIF-5A stimulates the formation of a peptide bond between fMet-tRNA^{fMet} and puromycin (Benne & Hershey, 1978), a reaction mimicking the formation of the first peptide bond in polypeptide synthesis. Amino-acid sequence alignment showed that eIF-5A is highly conserved among eukaryotes (about 60% identity), but the identity level between eIF-5A and aIF-5A is relatively low (~35% for yeast eIF-5A and aIF-5A) (Zanelli & Valentini, 2007). eIF-5A was found to be essential for cell growth and it can be functionally substituted *in vivo* by the protein from other eukaryotes (Magdolen *et al*., 1994; Park *et al*., 2010). Elongation factor P (EF-P), a prokaryotic protein homologous to eIF-5A, was also found to be important for synthesis of the first peptide bond in translation (Glick & Ganoza, 1975; Benne & Hershey, 1978). Although the amino-acid sequence similarity between eIF-5A and EF-P is only about 20%, the two proteins share significant structural similarity (Kyrpides & Woese, 1998; Hanawa-Suetsugu *et al*., 2004).

1.1.1 Structure of eIF-5A

Crystal structures of eIF-5A have been determined for human eIF-5A (PDB code: 3CPF; Tong *et al*., 2009), yeast eIF-5A (PDB code: 3ER0), *Arabidopsis* eIF-5A (PDB code: 3HKS; Teng *et al*., 2009), and *Leishmania* eIF-5A (PDB codes: 1X6O, 1XTD). Several X-ray structures of aIF-5A have also been reported as well (PDB codes: 1EIF, 2EIF, 1IZ6, 1BKB; Kim *et al*., 1998; Yao *et al*., 2003). These structures revealed that both eIF-5A and aIF-5A consist of

two predominantly β-sheet domains, a basic N-terminal domain and an acidic C-terminal domain (Fig. 1.1 A & B) (Kim *et al*., 1998; Yao *et al*., 2003; Teng *et al*., 2009; Tong *et al*., 2009). The N-terminal domain, consisting of six β-strands and a one-turn 3_{10}-helix, is highly conserved between eukaryotes and archaea. The C-terminal domain, resembling the oligonucleotide-binding fold found in RNA-binding proteins, is less conserved than the N-terminal domain (Zanelli & Valentini, 2007). A three-turn α-helix connecting β9 and β10 in the C-terminal domain of eIF-5A does not exist in aIF-5A (Fig. 1.1 A & B). Another common feature of eIF-5A and aIF-5A is that there is an extremely basic exposed loop linking β3 and β4 in the N-terminal domain (Fig. 1.1 A & B). A lysine residue located at the tip of this exposed loop is subject to a unique posttranslational modification (see below). This loop is only partially visible in several X-ray structures indicating that it is flexible.

Compared to eIF-5A and aIF-5A, EF-P contains an additional domain (in total, three domains). Located at the N-terminus of EF-P, domain I shares the same topology with the N-terminal domain of eIF-5A and aIF-5A. Domains II and III of EF-P, which likely derived from gene duplication, display a topology similar to the C-terminal domain of aIF-5A. A highly basic exposed loop is also present in domain I of EF-P and a lysine residue in this loop is subject to a unique posttranslational modification (see below). Many properties of EF-P remarkably resemble transfer RNAs (tRNAs), such as molecular dimension, “L” shape, and largely negatively charged surface (Hanawa-Suetsugu *et al*., 2004) (Fig. 1.1 C). In contrast, eIF-5A and aIF-5A do not mimic the “L” shape of tRNA due to the absence of the additional domain (domain III in EF-P).

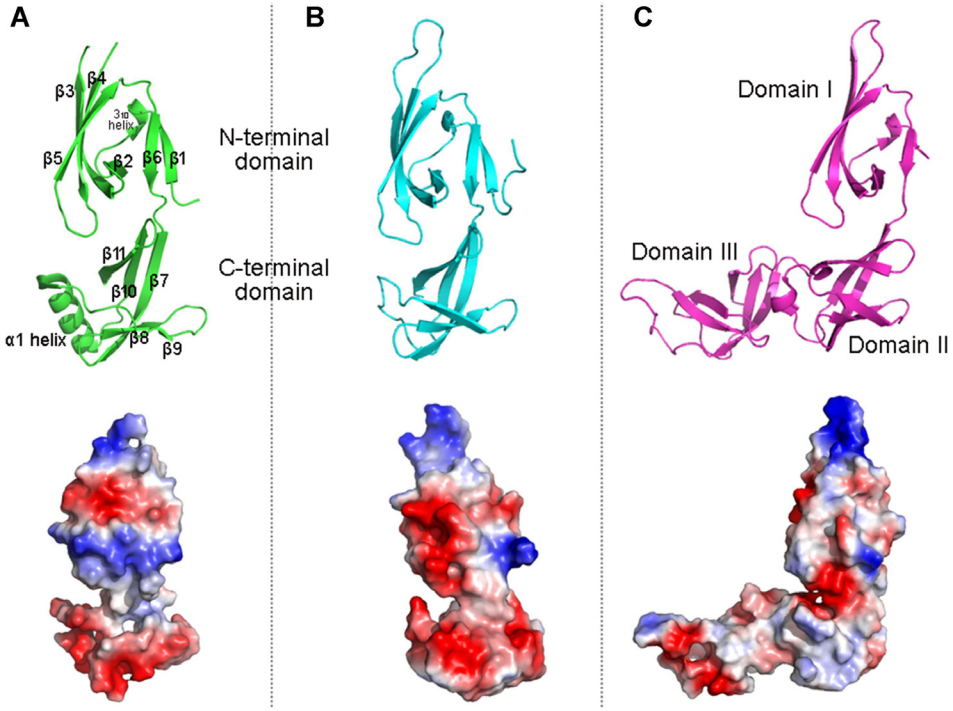

Fig. 1.1 Structures of eIF-5A, aIF-5A, and EF-P. Top: cartoon presentation; bottom: surface electrostatic potential colored from red (negative charge) to blue (positive charge).
(A) Structure of human eIF-5A (isoform 1) (PDB code: 3CPF; Tong *et al*., 2009). Human eIF-5A isoform 1 consists of eleven β-strands, a one-turn 3_{10}-helix, and a three-turn α-helix. The exposed loop connecting β3 and β4 is disordered in the structure. β-strands and α-helices are labeled.
(B) Structure of aIF-5A from *Methanocaldococcus jannaschii* (PDB code: 2EIF, cyan; Kim *et al*., 1998).
(C) Structure of EF-P from *Thermus thermophilus* (PDB code: 1UEB; Hanawa-Suetsugu *et al*., 2004). EF-P consists of three domains.

1.1.2 eIF-5A isoforms: eIF5-A1 and eIF-5A2

In many eukaryotes, there are two genes encoding two isoforms of eIF-5A, which share high amino-acid sequence identity (> 80%). In yeast, the two isoforms of eIF-5A are encoded by *HYP1* and *HYP2* (Schnier *et al*., 1991; Magdolen *et al*., 1994). Transcription of these genes is regulated by oxygen (*HYP*1: anaerobiosis; *HYP2*: anaerobiosis and aerobiosis) (Mehta *et al*., 1990; Wöhl *et al*., 1993; Magdolen *et al*., 1994). In man, two genes, *EIF5A1* and *EIF5A2*, encode eIF-5A1 and eIF-5A2, respectively (Smit-McBride *et al*., 1989).

EIF5A1 and *EIF5A2* are located in different regions of the genome. *EIF5A1* maps to chromosome 17p12-13 (Steinkasserer *et al*., 1995), whereas *EIF5A2* is localized at chromosome 3q25-q27 (Jenkins *et al*., 2001).

EIF5A1 is constitutively expressed in normal cells and over-expressed in tumor cells (Cracchiolo *et al*., 2004; Clement *et al*., 2006). In contrast, *EIF5A2* is expressed in a tissue-specific manner. It is predominately expressed in transformed cell lines and several special tissues, such as testis and brain (Jenkins *et al*., 2001; Clement *et al*., 2003, 2006; Guan *et al*., 2004; Chen *et al*., 2009). Numerous studies suggest that eIF-5A2 is an oncoprotein because of its tumor-specific expression profile and ability to trigger cellular transformation (Guan *et al*., 2001, 2004; Zender *et al*., 2008) and to promote tumor metastasis (Xie *et al*., 2008; Yang *et al*., 2009; Chen *et al*., 2009; Tang *et al*., 2010; Wang *et al*., 2013).

The different biological functions observed for human eIF-5A1 and eIF-5A2 are surprising, as the amino-acid sequences of these two isoforms are 84% identical (Clement *et al*., 2003). One possible explanation is that the major sequence variations between these two isoforms, which are located in the C-terminal domain of the proteins (Clement *et al*., 2003), influence the interaction of the eIF-5A isoforms with their biological partners. For instance, eIF-5A1 and eIF-5A2 display different affinities to deoxyhypusine synthase (DHS) (see below) and different kinetic properties (as the substrates of DHS, K_m = ~ 1 μM for eIF-5A1, K_m = ~ 8 μM for eIF-5A2). A structural comparison of human eIF-5A1 and eIF-5A2 should be able to find some clues relevant to the functional difference between these two isoforms but no three-dimensional structure is available for human eIF-5A2.

1.1.3 Oligomeric state of eIF-5A

An early study found that the molecular mass of native eIF-5A from human red

blood cells was 25.8 and 34.1 kDa, as determined by size-exclusion chromatography and equilibrium sedimentation, respectively. On the other hand, the values obtained by using the same methods but under denaturing conditions were 18.0 and 17.5 kDa, suggesting that human eIF-5A is a dimer (Chung *et al*., 1991). Two recent studies of recombinant yeast eIF-5A also suggest that the protein behaves as a dimer and that dimerization is dependent on the binding of RNA (Gentz *et al*., 2009; Dias *et al*., 2013). In addition, Gentz *et al*. (2009) found that hypusination (posttranslational modification of eIF-5A, see below) is required for dimerization, whereas Dias *et al*. (2013) demonstrated that this requirement is not essential. Small-angle X-ray scattering (SAXS) showed that the yeast eIF-5A dimer resembles tRNA and EF-P in shape and size (Dias *et al*., 2013).

1.1.4 Posttranslational modification of eIF-5A: hypusination

Hundreds of proteins are subject to covalent modifications by which the biological functions of the proteins can be modulated (Walsh *et al*., 2005). Generally, protein posttranslational modifications such as phosphorylation, acetylation, glycosylation, methylation, and ubiquitylation occur with many proteins. However, there are three types of unique modifications each of which is observed for only one protein (Greganova *et al*., 2011; Mittal *et al*., 2013). These are ethanolamine phosphoglycerol modification of elongation factor 1A (eEF1A), diphthamide modification of elongation factor 2 (eEF2), and hypusination of eIF-5A. In addition, the recently identified lysyllysine modification is probably unique to EF-P (Yanagisawa *et al*., 2010). Remarkably, all of these proteins are involved in protein synthesis.

Hypusine (Hpu) [N^{ε}-(4-amino-2-hydroxybutyl)-lysine] is a natural amino acid first reported in 1971 (Shiba *et al*., 1971). Subsequent studies revealed that Hpu is present in a cellular protein and that spermidine is required for its biosynthesis (Park *et al*., 1981; Cooper *et al*., 1982). Later, eIF-5A was found

to be the protein carrying Hpu (Cooper *et al*., 1982, 1983). The Hpu residue is afforded by two consecutive modifications of a key lysine residue in eIF-5A (Park *et al*., 1982; Murphey *et al*., 1987; Park, 2006) (Fig. 1.2 A). In the first catalytic step, deoxyhypusine synthase (DHS) [EC 2.5.1.46] converts the lysine residue to an intermediate form, deoxyhypusine (Dhp) [N^{ε}-(4-aminobutyl)-lysine]; the second catalytic reaction is performed by deoxyhypusine hydroxylase (DOHH) [EC 1.14.99.29]. The highly conserved lysine residue to be hypusinated (Lys50 in human eIF-5A and Lys51 in yeast eIF-5A) is located on an exposed loop in the N-terminal domain of eIF-5A (Fig. 1.1) (Wolff *et al*., 2007). The other residues in this loop are also mainly basic and strictly conserved ($KTGK_{50}HGHAK$ in human eIF-5A) (Cano *et al*., 2008; Park *et al*., 2010). Site-directed mutagenesis experiments revealed that the residues in the Hpu-containing loop are critical for the proper function of eIF-5A (Cano *et al*., 2008).

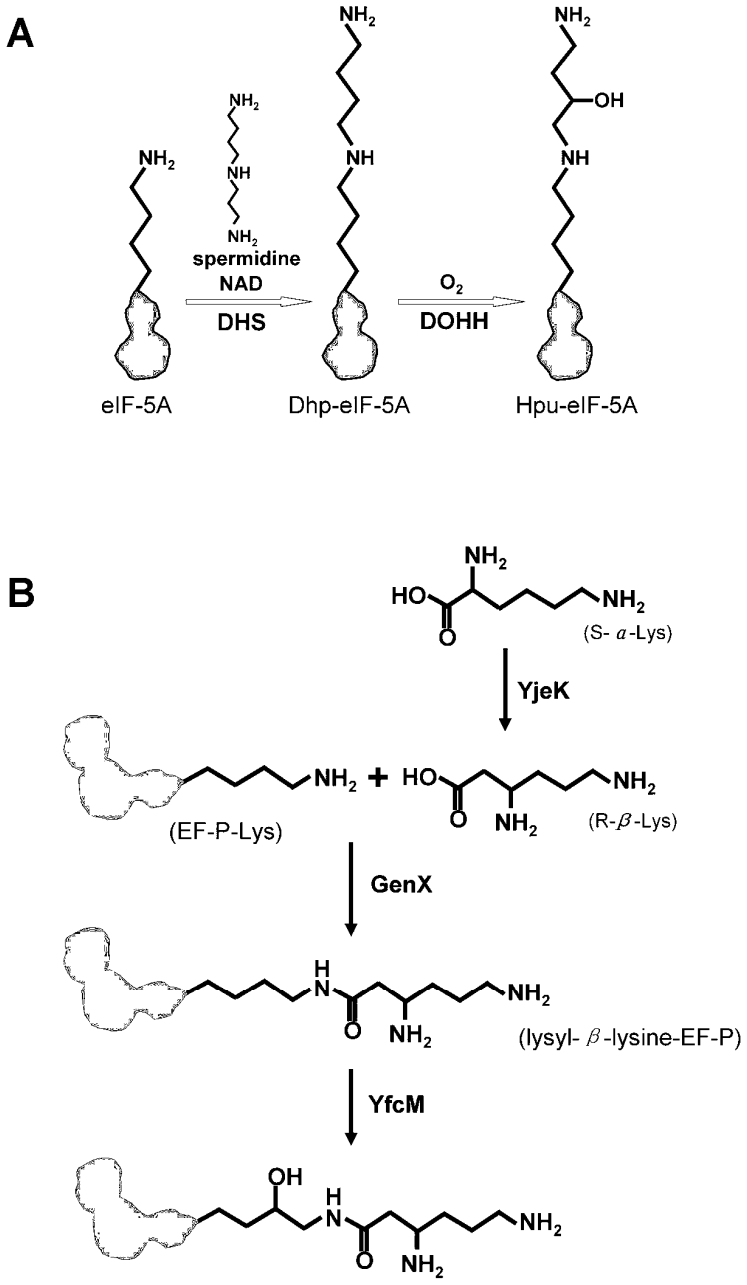

Fig. 1.2 Schemes of posttranslational modification of eIF-5A and EF-P.
(A) Two-step reaction for Hpu biosynthesis. In presence of the cofactor NAD and the cosubstrate spermidine, deoxyhypusine synthase (DHS) catalyzes the formation of Dhp-eIF-5A by transferring a butyl-amine moiety to a lysine residue of the eIF-5A precursor; deoxyhypusine hydroxylase (DOHH) catalyzes the formation of Hpu-eIF-5A.
(B) Posttranslational modification of EF-P. R-*β*-Lys is converted from S-*α*-Lys by a bacterial enzyme, YjeK; GneX catalyzes the formation of a lysyllysine residue by transferring R-*β*-Lys to a lysine residue in the EF-P precursor; finally, YfcM hydroxylases a carbon, putatively at the C5 position.

Interestingly, the homolog of eIF-5A in prokaryotes, EF-P, undergoes a similar posttranslational modification. It is also achieved by a two-step modification of a key lysine residue (Lys34 in *Escherichia coli* EF-P) (Fig. 1.2 B). YjeK, a lysine 2,3-aminomutase, converts S-*α*-lysine to R-*β*-lysine, which is used as substrate for the following step (Behshad *et al*., 2006); GenX, a homolog of class II lysine-tRNA synthetase, catalyzes the formation of a lysyllysine residue by transfering the R-*β*-lysine to the lysine residue in EF-P (Yanagisawa *et al*., 2010); YfcM, a hydroxylase distinct from DOHH, mediates the final maturation step (Peil *et al*., 2012).

The posttranslational modifications of eIF-5A and EF-P are critical for the biological functions of the proteins, which are discussed in the following sections.

1.1.5 eIF-5A, a bimodular protein

Many studies have shown that eIF-5A interacts with both RNAs and proteins. In addition to the proteins performing posttranslational modification (DHS, DOHH), a large number of interaction partners of eIF-5A have been identified, such as the general nuclear export receptor CRM1 (Rosorius *et al*., 1999), ribosomal protein L5 (Schatz *et al*., 1998), HIV Rev (Ruhl *et al*., 1993), nucleoporins (Hofmann *et al*., 2001), and nuclear actin (Hofmann *et al*., 2001). It is worth noting that all of these proteins found to interact with eIF-5A are related to leucine-rich nuclear export signal (NES)-dependent nuclear-cytoplasmic transport.

On the other hand, it has been confirmed that eIF-5A directly interacts with RNAs. In a Dhp/Hpu-dependent manner, eIF-5A directly binds to the HIV Rev response element (REE) and U6 snRNA (Liu *et al*., 1997). By using a systematic evolution of ligands by exponential enrichment (SELEX) approach, it has been shown that Hpu-eIF-5A binds to the synthetic RNA motifs UAACCA

and AAUGUCACAC, which are found in more than 400 human expressed sequence tags (Xu & Chen, 2001). Affinity purification and differential polymerase chain reaction (PCR) showed that eIF-5A also binds to certain cellular mRNAs *in vitro*, such as mRNAs encoding ribosomal L35a and ADP-ribose pyrophosphatase (Xu *et al.*, 2004). However, the biological significance of these interactions is unclear. In addition to direct binding of RNAs, the studies on yeast models suggested a role for eIF-5A in mRNA decay. Inactivation of a temperature-sensitive eIF-5A mutant resulted in accumulation of uncapped mRNAs and certain short-lived mRNAs (Zuk & Jacobson, 1998; Valentini *et al.*, 2002; Schrader *et al.*, 2006). eIF-5A influences the lifetime of mRNAs probably through shielding mRNAs in stress granules (Li *et al.*, 2010).

The bimodular feature of eIF-5A probably allows the protein to function as a steric modulator or adaptor in giant RNA-protein complexes, such as the protein synthesis machinery or the nuclear transport complex (e.g. CRM1-NES-RanGTP-cargo(RNA)), which are associated with a role for eIF-5A in translation and nuclear export of certain RNAs (see below).

1.1.6 Functions of eIF-5A

Studies focusing on the role of eIF-5A and Hpu biosynthesis have been carried out for more than 30 years; however, a consensus function of this protein still has not been confirmed. Depletion or inactivation of eIF-5A and enzymes involved in Hpu biosynthesis (DHS or DOHH) turned out to be lethal in many systems, indicating the essential nature of eIF-5A and its unique posttranslational modification (Schnier *et al.*, 1991; Wöhl *et al.*, 1993; Park *et al.*, 1998; Patel *et al.*, 2009). eIF-5A seems to be a multifunctional protein, involved in protein synthesis, mRNA decay, mRNA nuclear export (related to HIV replication, dendritic cell (DC) maturation, and diabetes), cell proliferation, and apoptosis. eIF-5A-related functions have been reviewed by Zanelli &

Valentini (2007) and others (Maier *et al*., 2010a; Hauber, 2010; Kaiser, 2012; Caraglia *et al*., 2013; Wang *et al*., 2013; Rossi *et al*., 2014).

1.1.6.1 Protein synthesis

Protein synthesis at ribosomes largely consists of three steps, initiation, elongation, and termination. In each of these, step-specific translation factors are involved. eIF-5A was found to be a translation factor involved in both initiation and elongation steps (Benne & Hershey, 1978; Kyrpides & Woese, 1998; Saini *et al*., 2009). Initially, eIF-5A was considered a translation initiation factor according to its ability to facilitate methionyl-puromycin synthesis (Benne & Hershey, 1978). In yeast, depletion or inactivation of eIF-5A by temperature-sensitive mutation led to a moderate decline of overall protein production (20 – 30%) (Kang & Hershey, 1994; Zuk & Jacobson, 1998). Deletion of eIF-5A (Chatterjee *et al*., 2006), or chemical blocking of DHS (Shi *et al*., 1996) or DOHH (Hanauske-Abel *et al*., 1994), led to inhibition of cell cycle progression at the G1/S boundary. These observations did not support a role for eIF-5A as a general translation factor but suggested that eIF-5A is critical for translation of a subgroup of mRNAs encoding proteins controlling the cell cycle (Hanauske-Abel *et al*., 1995).

Subsequent studies suggested a role for eIF-5A in translation elongation. Depletion of eIF-5A or blocking Hpu biosynthesis caused translational pause and significant decrease of overall protein production (Saini *et al*., 2009; Gregio *et al*., 2009). These consequences are similar to the effects of blocking protein synthesis at the elongation step by using cycloheximide or sordarin (Saini *et al*., 2009). Overexpression of eEF2 could compensate the depletion or inactivation of eIF-5A (Dias *et al*., 2012). All of these observations suggested that eIF-5A plays a role in ribosomal translocation. However, Henderson's and Hershey's study using a yeast system with different genetic backgrounds revealed that eIF-5A stimulates protein synthesis in both initiation

and elongation (Henderson & Hershey, 2011a, b), demonstrating that the function of eIF-5A in translation is still controversial.

A series of recent studies defined a new concept for eIF-5A in translation. Gutierrez *et al*. (2013) found that eIF-5A is required for synthesis of proteins containing consecutive proline residues *in vitro* and *in vivo*. The same observations were also made for EF-P (Doerfel *et al*., 2013; Ude *et al*., 2013; Woolstenhulme *et al*., 2013). These findings are in agreement with the fact that incorporation of proline into the polypeptide chain during translation is much slower than that of the other 19 amino acids and that ribosomes always pause at polyproline regions (Pavlov *et al*., 2009; Woolstenhulme *et al*., 2013). Proteome-wide analysis revealed that polyproline-rich proteins are widely present in eukaryotes, in particular man (Mandal *et al*., 2014). These polyproline-rich proteins play a role in many important biological processes such as RNA metabolism, DNA transcription, and cell signaling.

Remarkably, structural information of EF-P and eIF-5A bound to the ribosome is available. A crystal structure of the ribosome-EF-P-fMet-tRNA$_i^{fMet}$ complex showed that EF-P is located between the P-site and the E-site, and interacts with the backbone of the P-site initiator tRNA (Blaha *et al*., 2009). Specifically, the basic exposed loop in domain I of EF-P interacts with the 3'-CCA end and domain III is located next to the anticodon loop of the P-site initiator tRNA. The specific interaction mode of EF-P on the ribosome implies that EF-P adjusts the position of the fMet-tRNA$_i^{fMet}$ in the P-site. Blaha *et al*. also modeled the binding mode of Hpu-eIF-5A on the ribosome, revealing that the Hpu residue interacts with the ribosomal peptidyl transferase center (PTC). By using a hydroxyl radical probing approach, Gutierrez *et al*. (2013) found that Dhp-eIF-5A is located near the E-site, with the Hpu residue interacting with the acceptor stem of the P-site tRNA.

On the basis of these findings, for the time being, a model for the function of eIF-5A/EF-P in translation can be proposed as shown in Fig. 1.3. In this model, eIF-5A/EF-P serves as a steric modulator on the ribosome. The ribosome stalls when it encounters consecutive codons for proline. eIF-5A/EF-P binds to the ribosome and takes up the position between the E-site and the P-site. eIF-5A/EF-P interacts with the backbone of the P-site peptidyl-tRNA and the Hpu/lysyllysine residue inserts into the PTC. Incorporation of eIF-5A/EF-P improves the interactions of peptidyl-Pro-tRNA in the P-site and enhances the peptidyl transferase activity of ribosomes. Without the assistance of eIF-5A/EF-P, the steric restrictions of the proline side-chain hinder the formation of a peptide bond between peptidyl-Pro-tRNA in the P-site and Pro-tRNA in the A-site (Gutierrez *et al*., 2013; Ude *et al*., 2013).

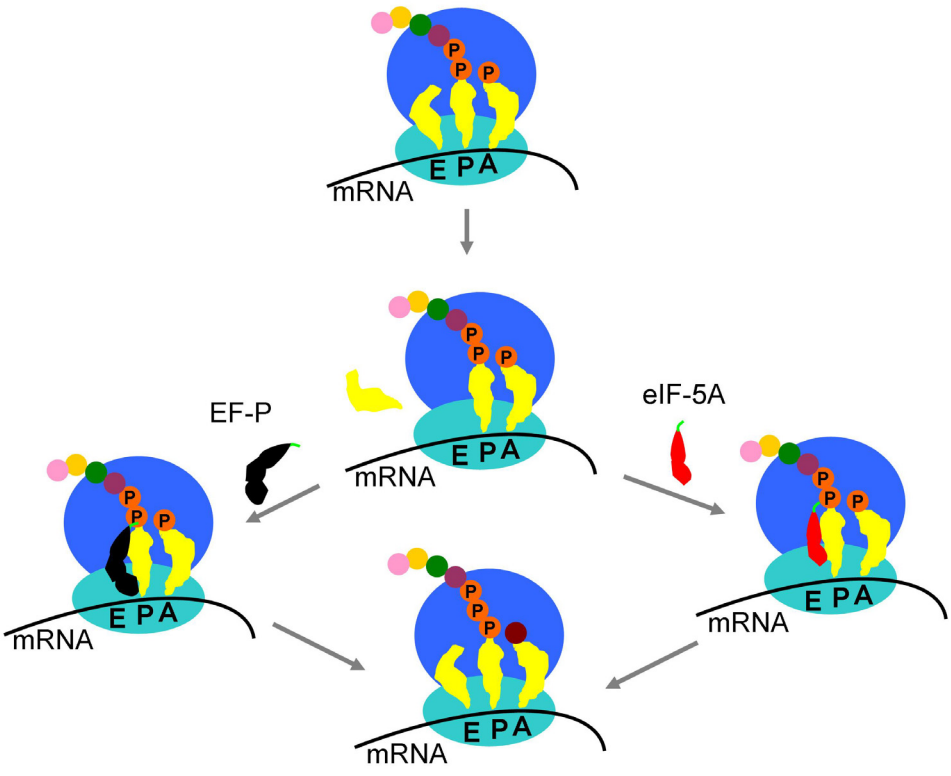

Fig. 1.3 A model of eIF-5A/EF-P in translation. After incorporation of two consecutive prolines into the polypeptide, the ribosome pauses if the next incoming residue is proline as well. In this situation, eIF-5A/EF-P is required as a steric modulator to help incoming P-site peptidyl-Pro-tRNA to adopt a favorable geometry for peptide bond formation. Lysyllysine and Hpu residues are presented as a short green line.

In this model, the monomeric form of eIF-5A is assumed to be the functional unit. Compared to EF-P, eIF-5A in the model cannot interact with the anticodon loop of the P-site tRNA due to lack of the additional carboxyl-terminal domain. Perhaps this interaction is not essential in eukaryotes, or eIF-5A acts as a dimer, thereby acquiring a similar shape and size as EF-P. In order to better understand the function of eIF-5A in translation, the oligomeric state of eIF-5A needs to be investigated.

1.1.6.2 eIF-5A and cancer

It is not surprising that a protein factor involved in protein synthesis is related to tumorigenesis. There is a new understanding of the relationship between translation and cancer development (Silvera *et al*., 2010; Ruggero, 2013). Many translation factors manipulate cell transformation, invasion, and metastasis through enhancing translational efficiency of certain tumor-specific mRNAs (Silvera *et al*., 2010). For instance, eIF4E, eIF4F, and eIF4G were found to be pro-oncoproteins (Fukuchi-Shimogori *et al*., 1997; De Benedetti & Harris, 1999; Silvera *et al*., 2010).

Human eIF-5A, in particular eIF-5A2, is specifically overexpressed in tumor cells (Clement *et al*., 2006). Therefore, eIF-5A is viewed as pro-oncoprotein (Caraglia *et al*., 2013). Many studies have shown that eIF-5A is essential for cell proliferation (Hanauske-Abel *et al*., 1994, 1995; Dong *et al*., 2005). It was proposed that eIF-5A enhances cell proliferation by facilitating the translation of a subclass of mRNAs that are critical for DNA replication (Hanauske-Abel *et al*., 1995; Silvera *et al*., 2010). Genome- and proteome-wide analysis of cancer cells (HeLa cells), in which eIF-5A or DOHH was silenced by RNAi, revealed that Hpu-eIF-5A manipulates a tumor-related gene network at the levels of transcription and translation (Mémin *et al*., 2014).

Two fundamental studies demonstrated a more detail role for eIF-5A in tumorigenesis. Using the short-hairpin RNA (shRNA) screen approach, Zender *et al*. (2008) identified an oncogenic signaling circuit consisting of exportin 4 (XPO4) and eIF-5A in a murine hepatocellular carcinoma (HCC) model. In this study, XPO4, a specific transporter for eIF-5A (Lipowsky *et al*., 2000), was identified as a tumor suppressor (Zender *et al*., 2008). Overexpression of eIF-5A2, rather than eIF-5A1, is essential for proliferation of XPO4-deficient tumor cells. XPO4 presumably suppresses cell proliferation through restricting the function of eIF-5A2 as a nuclear export adaptor for tumor-related mRNAs. A related study using a similar technique in a mouse lymphoma model found two tumor suppressors, adenosylmethionine decarboxylase 1 (AMD1) and eIF-5A, both of which are involved in Hpu biosynthesis (Scuoppo *et al*., 2012). Deletions of the two genes often occur simultaneously in human lymphomas and suppressions of both of genes trigger tumor development. Therefore, as tumor suppressors, AMD1 and eIF-5A act in concert. A particular role for eIF-5A2 was not observed in this study (Scuoppo *et al*., 2012). It can be seen that the function of eIF-5A in these two studies is distinct (oncoprotein versus tumor suppressor). The reason for this contradiction probably lies in the usage of the different cancer models (Zender *et al*., 2008; Scuoppo *et al*., 2012), or in the fact that the degree of hypusination *in vivo* was not taken into account in these two studies.

It has been proposed that the degree of cellular Hpu mediates the balance between proliferation and apoptosis (Tome & Gerner, 1997; Caraglia et al., 2001, 2013). The eIF-5A precursor is found to induce cell apoptosis. Cell apoptosis can be induced through transfection of ornithine decarboxylase (Tome & Gerner, 1997), tissue transglutaminase (tTG) (Beninati *et al*., 1998), or interferon-α (IFNα) (Caraglia *et al*., 1997, 2003), all of which decrease cellular Hpu content (reviewed by Caraglia *et al*., 2013). The product of ornithine decarboxylase, putrescine, is a competitive substrate for DHS; tTG

impairs posttranslational modification of eIF-5A by formation of γ-glutamyl-Hpu (Beninati *et al*., 1995, 1998); IFNα is also found to be a strong inhibitor for hypusination (Caraglia *et al*., 1997). On the basis of these findings, it can be appreciated that the function of eIF-5A in tumorigenesis is dependent on hypusination. The eIF-5A precursor and Hpu-eIF-5A trigger cell apoptosis and proliferation, respectively.

It has been shown that inhibition of the Hpu biosynthetic pathway is an effective anticancer or antiproliferation approach in several cancer models and cell lines, such as chronic myeloid leukemia (CML) (Balabanov *et al*. 2007; Ziegler *et al*., 2012), melanoma (Jasiulionis *et al*., 2007), mouse multiple myeloma (Taylor *et al*., 2012), colon cancer cells (Ignatenko *et al*., 2009), HCC cell line (Lee *et al*., 2010; Shek *et al*., 2012), glioblastoma (Preukschas *et al*., 2012), and human umbilical vein endothelial cells (Clement *et al*., 2002). In addition, the unique posttranslational modification pathway of eIF-5A (hypusination) supplies more targets and potential combinatory effects for cancer therapy.

1.1.6.3 eIF-5A and RNA nucleocytoplasmic export

It has been found that eIF-5A is a cellular cofactor for nucleocytoplasmic translocation of HIV-specific viral RNAs (Ruhl *et al*., 1993), mRNA of CD83 (a surface protein in dendritic cells) (Kruse *et al*., 2000), and iNOS-encoding mRNA (Maier *et al*., 2010b), which are crucial for HIV-1 replication, DC maturation, and islet *β* cells function, respectively.

eIF-5A is one of many host proteins, such as CRM1, importin-*β*, nucleoporins, hRIP, Sam68, and RNA helicases, found to serve as cofactor for Rev-mediated nuclear export (Suhasini & Reddy, 2009; Liu *et al*., 2011; Fernandes *et al*., 2012). Nonfunctional mutants of eIF-5A suppress HIV-1 replication through blocking Rev-mediated nuclear export (Bevec *et al*., 1996). It has been shown

that eIF-5A binds to the nuclear export signal (NES) of Rev (Ruhl *et al*., 1993), RRE-containing vRNAs (Liu *et al*., 1997), and CRM1 (Rosorius *et al*., 1999). These interactions with multiple components of the nuclear export complex imply that eIF-5A may serve as an adaptor in RanGTP-CRM1-Rev(NES)-vRNA(REE) complex (Suhasini & Reddy, 2009) (Fig. 1.4).

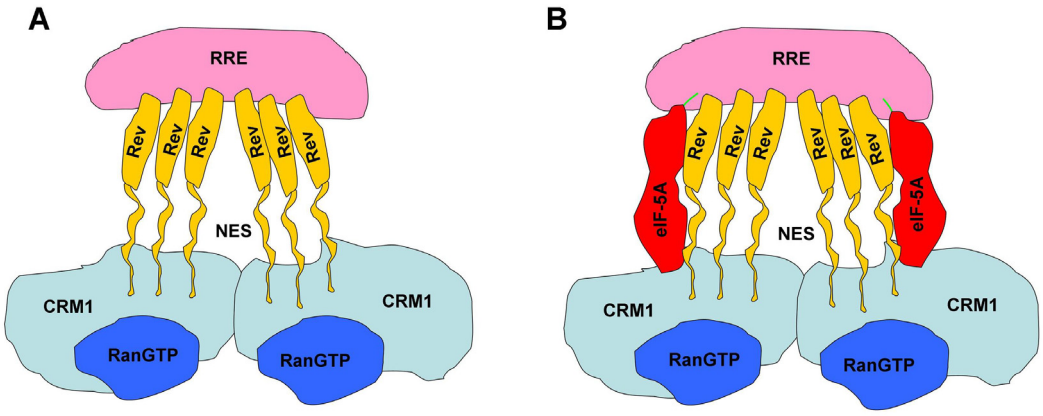

Fig. 1.4 A model for the role of eIF-5A in RNA nucleocytoplasmic export.
(A) The "Jelly-fish" model for Rev-mediated HIV mRNA nuclear export was proposed on the base of crystal structures of Rev (Daugherty *et al*., 2010) and CRM1–RanGTP (Monecke *et al*., 2009). The Rev-response element (RRE) offers a scaffold to assemble the Rev hexamer. Nuclear export signal (NES) located in the C-terminal non-structured region of Rev binds to CRM1.
(B) eIF-5A interacts with REE, NES, and CRM1. Two molecules of eIF-5A are shown in the model. Hpu (presented as a green line) is essential for eIF-5A binding to the REE (Liu *et al*., 1997).

It has been shown that inhibitors targeting Hpu biosynthesis block HIV replication. Targeting DHS, CNI-1493 (N,N'-bis[3,5-bis[1(aminoiminomethyl) hydrazonoethyl] phenyl] decanediamide tetrahydrochloride) (Hommes *et al*., 2002), efficiently suppresses HIV-1 replication (Hauber *et al*., 2005). Iron chelators such as mimosine (a natural amino acid), ciclopirox (CPX) (a topical antifungal), and deferiprone, all of them targeting DOHH, inhibit HIV-1 gene expression (Andrus *et al*., 1998; Goebel *et al*., 2008; Hoque *et al*., 2009). These studies suggested that eIF-5A and its posttranslational modification pathway are druggable targets for HIV-1 therapy.

Inducible nitric oxide synthase (iNOS) catalyzes the production of nitric oxide (NO), which induces islet *β* cell necrosis by shrinking ATP production (Leist *et al*., 1999). eIF-5A was found to be essential for nucleocytoplasmic export of iNOS mRNA (Maier *et al*., 2010b). Therefore, eIF-5A plays an important role in diabetes (Maier *et al*., 2010a). It has been shown that depletion of eIF-5A or inhibition of the Hpu biosynthesis pathway protects against glucose intolerance in the models of diabetes in inflammatory mouse and *β* cell line (Maier et al., 2010b; Robbins *et al*., 2010). The mechanism for eIF-5A in nucleocytoplasmic export of iNOS mRNA is not known. Perhaps, eIF-5A plays a similar role as in HIV Rev-mediated vRNA transport.

1.2 Deoxyhypusine synthase

Deoxyhypusine synthase (DHS) is the first enzyme in Hpu biosynthesis pathway (Park, 2006) (Fig. 1.2). The enzyme is present in both archaea and eukaryotes (Park *et al*., 2010). DHS is highly conserved among eukaryotes; for instance, DHS from man and *Saccharomyces cerevisiae* share 68% amino-acid sequence identity (Wolff *et al*., 2007).

1.2.1 Structure of DHS

Size-exclusion chromatography and dynamic light-scattering (DLS) suggested that DHS exists as a tetramer of total molecular mass ~160 kDa (Wolff *et al*., 1990, 1995; Kang *et al*., 1995). Crystal structures of DHS (PDB codes: 1DHS, 1ROZ, 1RQD; Liao *et al*., 1998; Umland *et al*., 2004) revealed that the DHS tetramer is composed of two types of dimer, a1/a2 and a1/b1 as shown in Fig. 1.5. Two antiparallelly arranged substrate-binding tunnels are located in the interfaces of molecule a1 and a2 or b1 and b2 (Fig. 1.5 A, B & C). Thus, the DHS tetramer harbors four equal active sites (Liao *et al*., 1998; Umland *et al*., 2004). The active sites are blocked by an N-terminal ball-and-chain motif (two-turn α-helix) in the structure of crystals obtained at low pH (PDB code: 1DHS; Liao *et al*., 1998). In contrast, the N-terminal ball-and-chain motif is

disordered when crystals grew at high pH and low ionic strength (Umland *et al*., 2004).

Asp243 and Lys329, located at the entrance of the substrate-binding tunnels, were found to be critical for enzymatic activity, but not important for interaction with eIF-5A (Umland *et al*., 2004) (Fig. 1.5 D). Asp313, located at the bottom of the tunnel, is crucial for eIF-5A binding (Fig. 1.5 D).

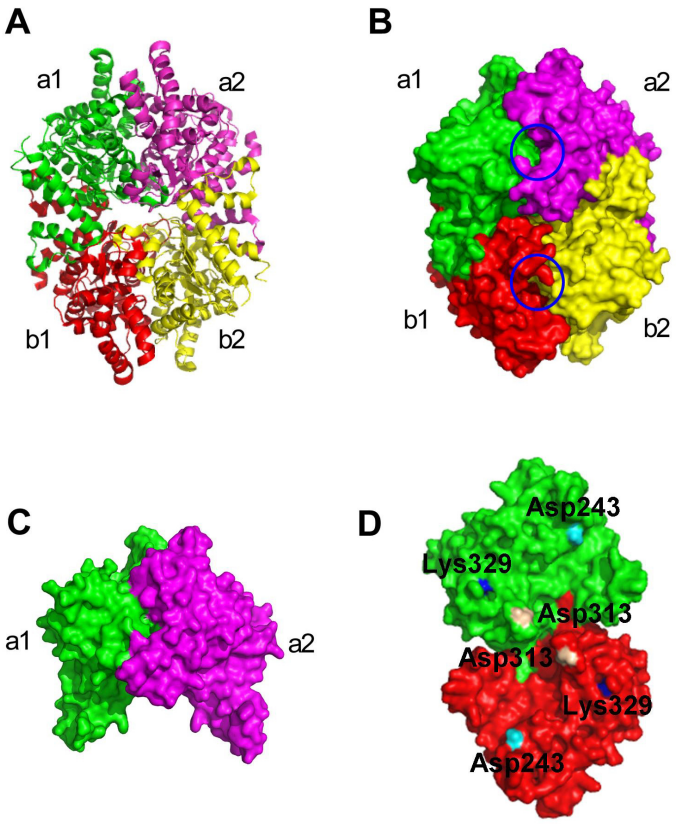

Fig. 1.5 Structure of DHS. DHS monomers in the tetrameric structure are labeled as a1, a2, b1, and b2 and shown in green, magenta, red, and yellow, respectively (PDB code:1RQD; Umland *et al*., 2004).
(A) Cartoon presentation of the DHS tetramer.
(B) Surface presentation of the DHS tetramer. Entrances of active-sites are marked with blue circles.
(C) DHS dimer form 1: a1/a2.
(D) DHS dimer form 2: a1/b1. Active site residues: D243 (cyan surface), D313 (pink surface), and K329 (blue surface).

1.2.2 Catalytic mechanism of DHS

In the presence of NAD^+, spermidine, and eIF-5A, DHS catalyzes the formation of Dhp-eIF-5A (Park, 2006). As shown in Fig.1.6, the catalytic process of DHS is a four-step reaction: 1) DHS-bound spermidine is dehydrogenated (Wolff *et al*., 1990); 2) butyl-amine from dehydrospermidine is transferred to a lysine residue in the active site of DHS (Lys329 in human DHS) (Wolff *et al*., 1997); 3) The DHS-bound butyl-amine is further transferred to a lysine residue in the eIF-5A precursor (Lys50 in human eIF-5A) (Wolff *et al*., 2000); 4) The Dhp residue is formed by a NADH-dependent reduction step. The DHS reaction is reversible. In presence of NAD^+ and 1,3-diaminopropane, DHS catalyzes the formation of spermidine (Park *et al*., 2003). In some plants, putrescine is an alternate butyl-amine acceptor in the DHS reaction, in which case homospermidine is generated (Ober & Hartmann, 1999; Ober *et al*., 2003) (Fig. 1.6). However, as a substrate of DHS, the K_m value for eIF-5A is ~ 700 times lower than for putrescine (Park *et al*., 2003).

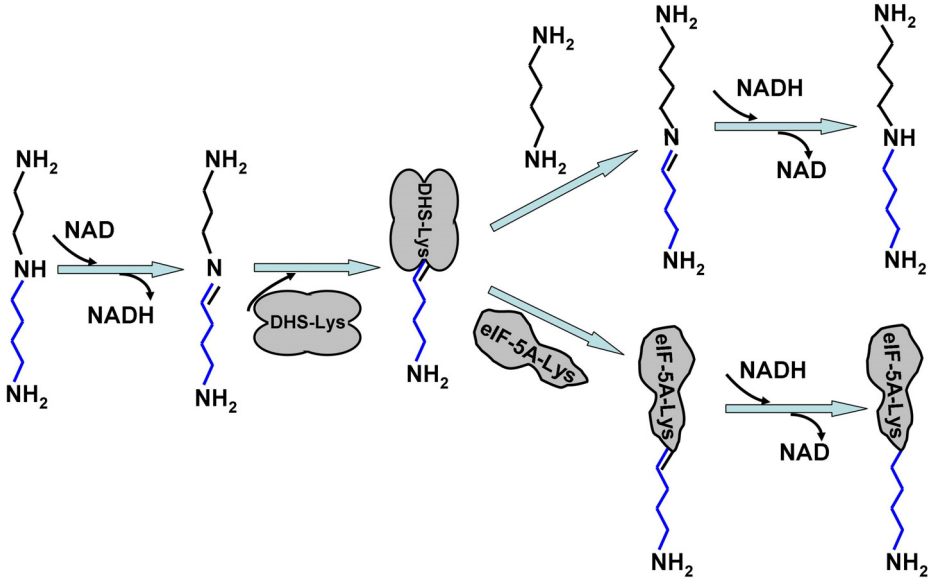

Fig. 1.6 Scheme of the DHS reaction. DHS catalyzes the dehydrogenation and cleavage of spermidine in the absence of the eIF-5A precursor; the butyl-amine moiety is transferred from spermidine to a lysine residue in the active site of DHS; the subsequent reactions are dependent on the type of substrate present. Both putrescine and eIF-5A can accept the DHS-bound butyl-amine moiety and generate homospermidine and Dhp-eIF-5A, respectively. The butyl-amine moiety transferred to the substrates is shown in blue.

1.2.3 The complex of DHS and eIF-5A precusor

An enzyme-substrate complex is formed when recombinant DHS and the eIF-5A precursor are incubated together (K_d < 0.5 nM) (Lee *et al*., 1999). The DHS-eIF-5A complex shows an obvious electrophoretic mobility-shift in native electrophoresis (Lee *et al*., 1999). NAD^+ or spermidine are not essential for complex formation (Lee *et al*., 1999). Unusually, even if Dhp-eIF-5A is generated, the complex does not disassemble (Lee *et al*., 1999). The data from native PAGE and equilibrium ultracentrifugation suggested that the binding stoichiometry of the components in the DHS - eIF-5A complex is one DHS tetramer bound to one eIF-5A monomer (Lee *et al*., 1999). This stoichiometry of binding is difficult to understand because there are four equal active sites in the DHS tetramer. An acceptable explanation may be that the binding of the first eIF-5A precursor to the DHS tetramer triggers a rearrangement of subunits in the DHS tetramer; the adjusted conformation of the DHS tetramer suppresses incorporation of additional eIF-5A precursors into the other three potential active sites; after completion of modification, incorporation of another eIF-5A molecule into one of the other active sites of the DHS tetramer facilitates the release of product, Dhp-eIF-5A. A crystal structure of DHS in complex with eIF-5A is necessary to understand the unique interaction between the enzyme and its substrate.

DHS in complex with different human eIF-5A isoforms (DHS-eIF-5A1 and DHS-eIF-5A2) display different mobilities in native electrophoresis (Clement *et al*., 2003), implying that the interaction modes for these two isoforms are different. According to amino-acid sequences, the major divergences between human eIF-5A1 and eIF-5A2 are located in their C-terminal domains (Clement *et al*., 2003). Therefore, it is likely that the C-terminal domain of eIF-5A is also involved in enzyme-substrate binding, although the minimum fragment required for the DHS reaction contains residues 30 - 80 in the N-terminal

domain of human eIF-5A (Joe & Park, 1994).

1.3 Deoxyhypusine hydroxylase

1.3.1 Overview of DOHH

DOHH is the second and last enzyme carrying out the posttranslational modification of eIF-5A. The enzyme is present in all eukaryotes (Park *et al*., 2010). DOHH was initially characterized from rat testis (Abbruzzese *et al*., 1986) and brain (Abbruzzese, 1988). The first DOHH gene, *YJR070C* encoding *Saccharomyces cerevisiae* DOHH (scDOHH), was identified by using a yeast two-hybrid system (Thompson *et al*., 2003). Subsequently, DOHH from many other organisms were also reported, such as human DOHH (hsDOHH) (Park *et al*., 2006), bovine DOHH (btDOHH) (Huang *et al*., 2007), *Plasmodium falciparum* DOHH (pfDOHH) (Frommholz *et al*., 2009), *Leishmania donovani* (ldDOHH) (Chawla *et al*., 2012), and *Plasmodium vivax* (pvDOHH) (Atemnkeng *et al*., 2013). scDOHH (325 residues) and hsDOHH (302 residues) share 48% amino-acid sequence identity (Park *et al*., 2006). The identity between *Plasmodium* DOHH and hsDOHH is much lower (less than 30%) (Frommholz *et al*., 2009). Archaeal DOHH has not been identified so far; however, Hpu was found in the archaeal kingdom (Bartig *et al*., 1990). Some archaeal species achieve hydroxylation of Dhp under anaerobic conditions, implying a mechanism different from eukaryotic DOHH at work in archaea for Hpu biosynthesis (Bartig *et al*., 1990).

Deletion of DOHH in yeast gave rise to a mild suppression of cell growth, implying that DOHH is probably not essential in yeast (Park *et al*., 2006). However, DOHH in multicellular organisms is Indispensable. Inactivation of DOHH by metal-chelating compounds in Chinese hamster ovary (CHO) cells led to cell-growth inhibition and cell-cycle arrest at the G1 phase (Hanauske-Abel *et al*., 1994). Lethal phenotypes were observed when DOHH was inactivated by using RNAi or *P*-element insertion in *Drosophila*

melanogaster (Spradling *et al*., 1999), *Caenorhabditis elegans* (Maeda *et al*., 2001), and *Drosophila melanogaster* (Patel *et al*., 2009). In addition, DOHH is critical for embryonic development and proliferation, as revealed in a DOHH knockout mouse (Sievert *et al*., 2014).

1.3.2 Biochemical and structural properties of DOHH

The crystal structure of DOHH has not been reported so far. The limited structural information available today on DOHH was obtained from sequence-based prediction, structure modeling, and spectroscopic studies. Circular dichroism spectroscopy revealed that DOHH is an α-helix-rich protein, with 77% and 59% α-helix in the human and yeast enzymes, respectively (Kim *et al*., 2006; Cano *et al*., 2010). It was predicted that DOHH belongs to the HEAT-repeat-containing protein family (Park *et al*., 2006). The HEAT-repeat has originally been identified in four distinct proteins (**H**untingtin, elongation factor 3 (**E**F3), protein phosphatase 2A (PP2**A**), and yeast kinase **T**OR1), which contain rod-like helical structures (Andrade & Bork, 1995). Structure modeling suggested that hsDOHH consists of 8 HEAT-repeats and an inter-domain loop linking HEAT-4 and HEAT-5 (Park *et al*., 2006). Four conserved histidine-glutamate motifs (HE motif) provide two potential metal coordination sites (Park *et al*., 2006).

hsDOHH specifically uses iron ions as its cofactor and one DOHH molecule contains two iron atoms as revealed by inductively coupled plasma-high resolution mass spectrometry (ICP-MS) (Kim *et al*., 2006). Other metal ions such as Cu^{2+}, Mg^{2+}, Mn^{2+}, Ni^{2+}, and Zn^{2+} could not be adopted by DOHH. Recombinant DOHH is partially metalated; therefore, the isolated enzyme is a mixture of holo-DOHH (iron-bound state) and apo-DOHH (iron-free state) (Fig. 1.7). Only holo-DOHH displays enzymatic activity. Holo-DOHH and apo-DOHH display different mobilities in native electrophoresis; holo-DOHH migrates faster than apo-DOHH. In addition, holo-DOHH exhibits a compact band,

whereas apo-DOHH shows a diffuse band in native electrophoresis (Kim *et al*., 2006; Cano *et al*., 2010). Size-exclusion chromatography showed that holo-DOHH is eluted earlier than apo-DOHH (Kim *et al*., 2006; Cano *et al*., 2010). These observations indicated that holo-DOHH features a homogenous architecture and the overall size of holo-DOHH is smaller than that of apo-DOHH. Small-angle X-ray scattering (SAXS) studies on scDOHH further confirmed that the holo-DOHH displays a compact and homogenous structure, whereas apo-DOHH is present in multiple conformations (Cano *et al*., 2010). The stability of holo-DOHH appears to be very limited. It has been shown that holo-DOHH starts to convert to apo-DOHH at ~35^{o}C or in the presence of 1 M guanidinium hydrochloride (Cano *et al*., 2010).

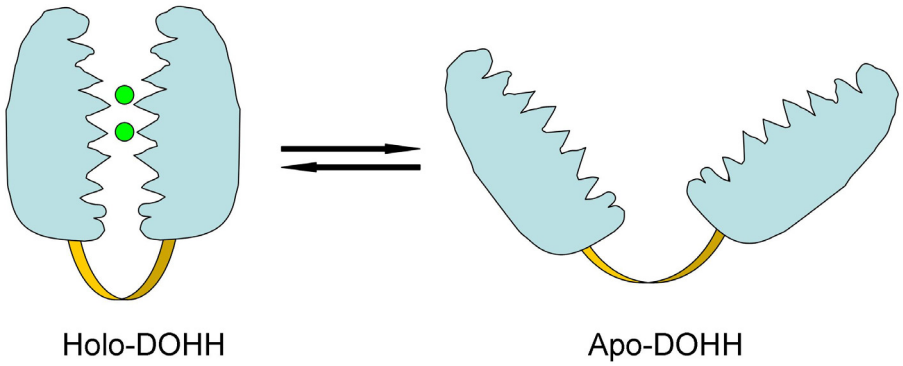

Fig. 1.7 Schematic structures of holo-hsDOHH and apo-hsDOHH. DOHH consists of N-terminal and C-terminal HEAT-repeats which are connected by an inter-domain loop (yellow). The overall structure of holo-DOHH is compact and two iron atoms (green balls) are located in the middle of the protein. In apo-DOHH, the N-terminal and C-terminal HEAT-repeats are separated from each other.

Alanine substitutions of the residues in the predicted HE motifs of hsDOHH led to loss of iron, suggesting that His56, His89, Glu90, His207, His240, and Glu241 are essential for iron-binding (Kim *et al*., 2006). A similar study on scDOHH revealed that H79, H112, E113, H237, H270, and E271 coordinate to the iron atoms (Cano et al., 2010).

The structural properties indicate that hDOHH is distinct from the group of Fe(II)/α-ketoglutarate-dependent hydroxylases, which catalyze the posttranslational modification of lysine/proline residues in collagen (Hausinger, 2004; Kim et al., 2006). The latter enzymes contain a β-strand jellyroll fold and a mononuclear iron center (Hausinger, 2004). DOHH does not use α-ketoglutarate and ascorbic acid as cofactors, implying that the catalytic mechanisms of DOHH and Fe(II)/α-ketoglutarate-dependent hydroxylases are different.

1.3.3 The active site of DOHH and the DOHH - Dhp-eIF-5A interaction

The active site of DOHH was first investigated by Abbruzzese *et al.* (1991), who used two inhibitory catechol peptides anchored to the metal ions through their dihydroxybenzene groups, to probe the active site of DOHH. It was estimated that a cavity of about 12 Å length accommodates the Dhp side-chain; the methylene to be hydoxylyzed should be close to the metal site, and its terminal amino group should contact one or more negatively charged side-chains of the enzyme (Abbruzzese *et al.*, 1991).

Numerous efforts have been made to characterize the interaction between DOHH and Dhp-eIF-5A. In an early study, a synthetic peptide (KTG-Dhp-HGHAK), sharing the same amino-acid sequence with the exposed loop in the N-terminal domain of eIF-5A, showed competitive inhibition of DOHH (Abbruzzese *et al*., 1989). The K_i value was 0.44 mM (Abbruzzese *et al*., 1989). No inhibitory activity was observed for free lysine or Dhp (Abbruzzese *et al*., 1989). More recently, a GST-pulldown experiment revealed that, compared to Dhp-eIF-5A, the eIF-5A precursor is devoid of binding affinity and Hpu-eIF-5A displays a weak interaction with hsDOHH (Kang *et al*., 2007). Polypeptides comprising at least residues 20 - 90 of the N-terminal domain of human eIF-5A are required for the binding to hsDOHH and used as effective substrates to be modified by hsDOHH (Kang *et al.*, 2007). These results

suggested that DOHH specifically recognizes Dhp-eIF-5A. The Dhp residue and the residues surrounding Dhp, as well as the N-terminal domain of eIF-5A, are involved in the interaction with DOHH.

Site-directed mutagenesis studies identified a number of residues (Glu57, Gly63, Glu90, Glu208, Gly214, Glu241) in hsDOHH that are critical for Dhp-eIF-5A binding (Kang *et al*, 2007). Alanine substitution of Glu90, Glu241, Gly63, or Gly214 led to significant loss of binding to Dhp-eIF-5A. In particular, two mutants of hsDOHH, E57A and E208A, totally lost substrate-binding ability and enzymatic activity. Aspartate substitutions of Glu57 and Glu208 (E57D and E208D) maintained partial binding to Dhp-eIF-5A and partial enzymatic activity, but mutants E57Q, E57N, E208Q, or E208N did not (Kang *et al*., 2007). A similar role as for Glu57 and Glu208 in hsDOHH was also observed for Glu116 and Glu274 in scDOHH (Cano *et al*., 2010). These mutagenesis studies suggested that two or more salt-bridges are critical for the DOHH - Dhp-eIF-5A interaction. It is likely that carboxyl groups of glutamate residues in DOHH (Glu57 and Glu208 in hsDOHH, Glu116 and Glu274 in scDOHH) act as the anchoring sites for the terminal amino group of the Dhp side-chain.

1.3.4 Diiron center and mechanism and of DOHH

Recombinant hsDOHH is bluish and contains two antiferromagnetically coupled, high-spin Fe(III) atoms, as revealed by Mössbauer spectroscopy studies (Vu *et al.*, 2009). The characteristic chromophore (two absorption bands, at λ_{max} ~320 nm and λ_{max} ~630 nm) is ascribed to the charge-transfer between Fe(III) and the O_2^{2-} ligand, suggesting that bluish hsDOHH is the peroxo-diiron(III) intermediate of the enzyme (Vu *et al.*, 2009). The peroxo-diiron(III) core changes to the diiron(II) form when the intermediate is treated with a chemical reductant such as sodium dithionite (Vu *et al.*, 2009). The peroxo-diiron(III) core is regenerated under aerobic conditions, indicating that DOHH is an O_2-activating diiron enzyme. Isolated and regenerated bluish

hsDOHH exhibits three bands, at 855, 493, and 473 cm^{-1}, in resonance Raman spectra (Vu *et al.*, 2009). No isotope effect between $^{16}O^{18}O$ and $^{18}O^{16}O$ was observed in the resonance Raman spectrum, indicating that the peroxo ligand binds to the diiron(III) core of hDOHH in a symmetric way (Vu *et al.*, 2009). Charge-transfer bands (630 - 725 nm) and Mössbauer parameters similar to those of hsDOHH have been found for the peroxo-diiron(III) intermediate of soluble methane monooxygenase hydroxylase (sMMOH) (Liu *et al.*, 1995a), ribonucleotide reductase subunit R2 (RNR-R2) (Moënne-Loccoz *et al.*, 1998), stearoyl-acyl carrier protein Δ^9-desaturase (Δ^9D) (Broadwater *et al.*, 1998), and ferritin (Bou-Abdallah *et al.*, 2005). The peroxo-diiron(III) intermediates in these enzymes have been assigned as end-on, bridging peroxo-diiron(III) species (*cis*-*μ*-1,2-peroxo-diiron(III)) (Model I in Fig. 1.8) based on the structures of biomimetic synthetic complexes displaying similar charge-transfer bands, Mössbauer parameters, and Raman bands (850 - 900 cm^{-1}) (Kim & Lippard, 1996; Zhang *et al.*, 2005). Therefore, it is proposed that the isolated bluish hsDOHH contains a *cis*-*μ*-1,2-peroxo-diiron(III) core (Vu *et al.*, 2009). However, the *μ*-1,2-peroxo geometry is still controversial, since Raman-spectroscopic studies cannot distinguish it from other symmetric arrangements of the peroxo ligand, such as a bridging side-on (η^2,η^2-1,2) coordination (Model III in Fig. 1.8), which is actually favored by quantum mechanics/molecular mechanics (QM/MM) studies in case of sMMOH (Gherman *et al.*, 2004; Rinaldo *et al.*, 2007). It has also been proposed that the peroxo-diiron(III) intermediate is present in the reaction cycle of toluene/o-xylene monooxygenase hydroxylase (ToMOH) (Murray *et al.*, 2007) and *p*-aminobenzoate N-oxygenase (AurF) (Korboukh *et al.*, 2009), although optical bands similar to those of ferritin or sMMOH are lacking in these systems. Possible peroxo-diiron(III) geometries for ToMOH and AurF are *μ*-1,1-peroxo-diiron(III) (Model IV in Fig. 1.8) (Murray *et al.*, 2007; Korboukh *et al.*, 2009). In addition, the peroxo-diiron(III) species is also present in hemerythrin (Hr), an O_2 carrier in marine invertebrates. However, an end-on

hydroperoxo ligand terminally binds to the diiron site in oxyhemerythrin (oxyHr) (Model VI in Fig. 1.8), leading to a charge-transfer band at λ_{max} ~500 nm (Dawson *et al.*, 1972; Klotz & Kurtz, 1984).

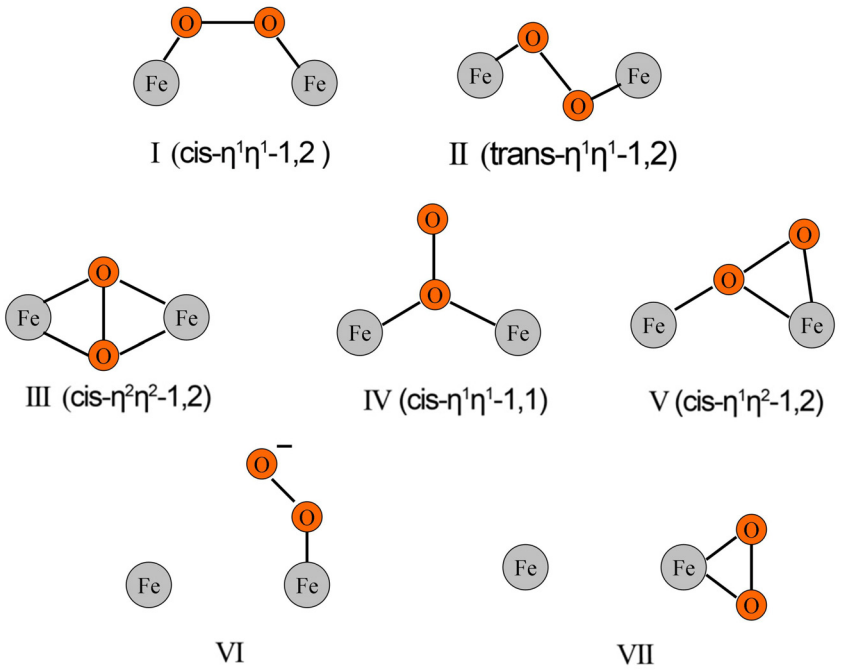

Fig. 1.8 Possible peroxo-diiron(III) geometries. The peroxo unit as bridging ligand for the diiron site: Models I – V; peroxo unit as terminal ligand: Models VI and VII. The nomenclature for peroxo-bridging diiron sites: η^1,η^1-1,2 (= μ-1,2), each oxygen binds to one iron only; η^2,η^2-1,2, each oxygen atom binds to two irons.

The peroxo-diiron(III) species detected in all these enzymes are present as transient intermediates with very short lifetimes. Therefore, characterization of the peroxo-diiron(III) species by crystallography is a challenge. After soaking crystals in H_2O_2 (a non-biological peroxide-shunt reaction), Bailey and Fox (2009) reported the structure of a peroxo intermediate of toluene 4-monooxygenase hydroxylase (T4moH) (in complex with effector protein). This structure may not represent the native state of the dioxygen-bound diiron core during O_2-actication, since the peroxo ligand was initially protonated, leading to differences in the proton balance within the active site (Bailey & Fox, 2009). Therefore, no protein structure containing a native

μ-1,2-peroxo-diiron(III) core has been reported so far, although a large number of biomimetic synthetic complexes containing this unit have been described (Ookubo *et al.*, 1996; Dong *et al.*, 1996; Kim & Lippard, 1996; Zhang *et al.*, 2005). In contrast, the peroxo-diiron(III) species in hsDOHH displays an extreme longevity, as it survives several days after protein purification, even at room temperature (Vu *et al.*, 2009). Therefore, hsDOHH is an excellent system to investigate the structural properties of the peroxo-diiron(III) intermediate in enzymes, thereby providing key information on the mechanisms of O_2-activating non-heme diiron enzymes. An atomic structure is essential to understand the structural properties of the transient intermediate as well as the interaction between hsDOHH and its specific substrate, Dhp-eIF-5A.

1.4 Objective and achievement of this thesis

eIF-5A is the only protein for which a posttranslational modification of a specific lysine residue to yield the amino acid Hpu has been demonstrated. This modification, which is essential for the functions of eIF-5A, is catalyzed by the enzymes DHS and DOHH. So far, the structures of eIF-5A from many species have been determined (PDB codes: 3CPF, 3ER0, 3HKS, 1X6O, 1XTD, 1EIF, 2EIF, 1IZ6, 1BKB; Tong *et al*., 2009; Teng *et al*., 2009; Kim *et al*., 1998; Yao *et al*., 2003); the structure and mechanism of DHS have also been extensively characterized (Park, 2006). However, no X-ray structure of DOHH is reported and the specific interactions between eIF-5A and DHS or DOHH are poorly understood. In addition, the structure of human eIF-5A2 has not been determined. In this thesis, X-ray crystallography is applied as the main approach to investigate the structures of individual proteins and the enzyme – substrate complexes on the entire pathway of hypusination.

First of all, three-dimensional structures of DOHH from man, yeast, and *Plasmodium vivax* are determined, in particular the structure of hsDOHH, which is extensively characterized in combination with spectroscopic

approaches and computational studies. Two crystal structures that correspond to two states of hsDOHH, the peroxo intermediate (POX) and a complex of the diiron core with glycerol (GLC) are determined at high resolution (both at 1.7 Å). The POX structure represents the first visualization of a native, biological *μ*-1,2-peroxo-diiron(III) core at atomic resolution. The structures of DOHH explain mechanisms for the unusual longevity of peroxo intermediate, namely a histidine-rich primary coordination sphere lacking bridging carboxylate ligands and a hydrophobic secondary coordination hemisphere. The crystal structures of DOHH help understand the specific interaction between the enzyme and Dhp-eIF-5A and provide a basis for the design of inhibitors that could be developed into drugs for the treatment of various diseases. Equally important, they will motivate more spectroscopic studies with this remarkable system. Because of the importance of the results on DOHH, they are presented first in this thesis.

In addition, the structure of human eIF-5A2 is determined experimentally and compared to eIF-5A1. The structure of human eIF-5A2 supplies many hints to understanding the distinct roles for the two isoforms of human eIF-5A in translation and tumorigenesis. The complex of human DHS and eIF-5A1 is crystallized, however the structure of this complex is not determined due to the poor diffraction of the crystals.

2. Materials and Methods

2.1. Materials

2.1.1 Equipments

The instruments used in this work are listed in Table 2.1.

Table 2.1 laboratory devices and manufacturers

Instrument	Manufacturer
Crystallization robot	Art-Robbins Instruments
Cryostream cooler	Oxford Cryosystems
Xcalibur PX Ultra X-radiation diffractometer	Oxford Diffraction
Microscope SZX 12	Olympus
PCR cycler	Biometra
Agarose gel electrophoresis system	Bio-Rad
PAGE gel electrophoresis system	Hoefer
Biophotometer (OD_{600})	Eppendorf
Atomic absorption spectrometer 180-80	Hitachi
Protein purification systems Äkta FPLC/Prime	GE Healthcare
Ultracentrifuge Centrikon T-2070	Kontron
Centrifuge Sigma 3-18K	Sigma
UV/Vis spectrophotometer Cary 50	Agilent
Dynamic light scattering	RiNA
pH-meter	Schott
Pipettes	Eppendorf
Sonificator W-250D	Branson
Thermomixer	Eppendorf
Innova 4230 refrigerated incubator shaker	New Brunswick Scientific
Synergy ultrapure water system	Merck Millipore
GSTrap™ FF (5 ml)	GE Healthcare
HisTrap™ FF (5 ml)	GE Healthcare
HiTrap™ Q FF (5 ml)	GE Healthcare
HiLoad Superdex™ 75 prep grade	GE Healthcare
HiLoad Superdex™ 200 prep grade	GE Healthcare

2.1.2 Consumables

The consumables used in this work are listed in Table 2.2.

Table 2.2 Columns and consumables

Material	Manufacturer
GeneRuler 1 kb DNA Ladder	Fermentas
Unstained protein molecular weight marker (#SM0431)	Fermentas
Dialysis bag	Spectrum Laboratories
AccuPrime *Pfx* polymerase kit	Invitrogen
GeneJet gel extraction kit	Thermo Fisher Scientific
GeneJet plasmid miniprep kit	Thermo Fisher Scientific
Rapid DNA ligation kit	Thermo Fisher Scientific
Crystallization screens	Hampton Research
Intelli-Plate-96-well	Art Robbins Instruments
Magnetic crystal caps	Hampton Research
Cryoloops	MiTeGen
microtools	Hampton Research
Cryschem M plate	Hampton Research

2.1.3 Chemicals

The chemicals used in this work are listed in Table 2.3.

Table 2.3 Chemicals used in this work

Chemical	Manufacturer
Ammonium chloride	Sigma-Aldrich
Ammonium sulfate	Merck
Ampicilline sodium	Gerbu Biotechnik
Bicine	Sigma-Aldrich
Bis-Tris	Sigma-Aldrich
Bis-Tris propane	Sigma-Aldrich
Dithiothreitol (DTT)	Gerbu Biotechnik
Glycerol	Gerbu Biotechnik
Guanidine hydrochloride	Sigma-Aldrich
HEPES	Roth
Imidazole	Merck
^{57}Iron foil	Provided by Prof. Alfred X. Trautwein
Iron(III) nitrate	Merck
Isopropyl -D-1-thiogalactopyranoside (IPTG)	Gerbu Biotechnik
Non-detergent sulfobetaines (NDSB-195)	Hampton Research
Polyethylene glycol (PEG) 3350, 6000	Sigma-Aldrich
Potassium formate	Merck
Reduced glutathione (GSH)	Sigma-Aldrich
Sodium chloride	Roth
Tris	Gerbu Biotechnik

2.2. Methods

2.2.1 Cloning

DNA templates used for gene amplifications are listed in Table 2.4. After double digestion with *Xho*I and *Bam*HI (*EcoR*I and *Not*I for scDOHH constructs) (Fermentas), DNA fragments were inserted into the digested pGEX-6P-1 vector

(GE Healthcare). Site-directed mutagenesis was carried out using *Pfx* polymerase (Invitrogen). All constructs were confirmed by sequencing (MWG Biotech). The primers (synthesized by MWG Biotech) used to construct the expression vectors and mutants are listed in Table 2.5.

Table 2.4 Source of DNA materials used as templates for DNA amplification

Gene	source
hsDOHH	pcDNA3.1/hsDOHH construct, provided by Prof. Joachim Hauber (Heinrich Pette Institute – Leibniz Institute for Experimental Virology, Hamburg, Germany)
scDOHH	pBlueScript II/scDOHH, purchased from Thermo Fisher Scientific
pfDOHH	pET28a/pfDOHH construct, provided by Prof. Annette Kaiser (University of Duisburg-Essen, Essen, Germany)
pvDOHH	pET28a/pvDOHH construct, provided by Prof. Annette Kaiser (University of Duisburg-Essen, Essen, Germany)
eIF-5A2	synthesized by MWG Biotech

Table 2.5 Primers used in this work

Primer	Sequence (5' to 3')
hsDOHH forward	taataGGATCCatggtgacggagcaggag
hsDOHH 283 reverse	taataCTCGAGctactggtgctcatacatgtccagagccac
hsDOHH 289 reverse	taataCTCGAGCTActggaaggcacgaccggtctcgtg
hsDOHH 292 reverse	taataCTCGAGCTAgtccgcgtactggaaggc
hsDOHH reverse	ggttgCTCGAGctaggaggggcccgcgcagctg
hsDOHH Y60A forward	gcacgagctggccgcgtgcctgggccagatg
hsDOHH Y60A reverse	catctggcccaggcacgcggccagctcgtgc
hsDOHH M86A forward	acccgtcaggagcccgcggtgcgccatgaggc
hsDOHH M86A reverse	gcctcatggcgcaccgcgggctcctgacgggt
hsDOHH M86L forward	cgtcaggagcccctggtgcgccatgag
hsDOHH M86L reverse	ctcatggcgcaccagggctcctgacg
hsDOHH Y211F forward	cacgaggtcggcttcgtcctgggacag
hsDOHH Y211F reverse	ctgtcccaggacgaagccgacctcgtg
hsDOHH M237L forward	accgagaacccctggtgcggcacgag
hsDOHH M237L reverse	ctcgtgccgcaccaggggttctcggt
hsDOHH E244A forward	gcacgagtgcgcggcggccctgggcgccattg
hsDOHH E244A reverse	caatggcgcccagggccgccgcgcactcgtgc
scDOHH forward	taataGAATTCatgtctactaactttgaaaaac
scDOHH reverse	taataGCGGCCGCctaattagcagttggagcatattc
pfDOHH forward	taataGGATCCatgggagaaaataacgacaac
pfDOHH reverse	taataCTCGAGctagtgaacctctatagatata
pfDOHH T17 forward	taataGGATCCggtgatagcagtaataaagtg
pfDOHH T41 forward	taataGGATCCagtacaaacaaagagttcattttg
pfDOHH T403 reverse	taataCTCGAGttaattttctgatatgtaatccaagcc
pfDOHH F391Y forward	catgaattagcttatgtattaggtcag
pfDOHH F391Y reverse	Ctgacctaatacataagctaattcatg
pvDOHH forward	taataGGATCCatgacaggaagtactcac
pvDOHH reverse	taataCTCGAGttaatttacttctattgc
pvDOHH T9 forward	taataGGATCCcgcctaatccagtatgaag
pvDOHH T17 forward	taataGGATCCagcaataaagagttcatcagg
pvDOHH T21 forward	taataGGATCCgagttcatcaggaaatac
pVDOHH T333 reverse	taataCTCGAGttaatccagtccaaccaggca
pVDOHH T340 reverse	taataCTCGAGttagtttaaattctcagctatg
eIF-5A2 forward	taataGGATCCatggcagatgaaattgacttc
eIF-5A2 reverse	taataCTCGAGttatttgcacggcttgattgc
eIF-5A2 T16 forward	taataGGATCCagcacctacccaatgcagtgc
eIF-5A1 forward	taataGGATCCatcaaaaggaatgacttccag
eIF-5A1 reverse	taataCTCGAGttatttttgccatggccttg
eIF-5A 1 T83 reverse	taataCTCGAGgttggggacatccatatt

hsDOHH: human DOHH; scDOHH: *Saccharomyces cerevisiae* DOHH; pfDOHH: *Plasmodium falciparum* DOHH; pvDOHH: *Plasmodium vivax* DOHH; uppercase letter in the sequences: restriction sites; red letter in the sequences: mutated codons.

2.2.2 Recombinant protein overexpression

Table 2.6 shows a summary of the optimized conditions for recombinant protein production. Normally, competent cells transformed with expression constructs were grown in 2x YT or LB medium containing 100 µg/mL ampicillin (100 µg/mL ampicillin + 50 µg/mL chloramphenicol when the Rosetta pLysS strain was used). Expression was induced with 0.3 – 1 mM IPTG until OD_{600} reached 0.6-0.8.

Table 2.6 Conditions for recombinant protein production

Construct	*Escherichia coli* strain	Medium	IPTG, mM	Temperature, ^{o}C	Time, h
pGEX-6P-1/hsDOHH	BL21-Gold	2 x YT	1.0	25	16
pGEX-6P-1/scDOHH	BL21-Gold	2 x YT	1.0	25	16
pGEX-6P-1/pfDOHH	Rosetta pLysS	2 x YT	0.3	20	16
pGEX-6P-1/pvDOHH	Rosetta pLysS	2 x YT	0.3	20	16
pGEX-6P-1/eIF-5A2	BL21-Gold	LB	1.0	37	4
pET-pre01/DOHH	BL21-Gold	LB	1.0	37	4
pET-pre01/DHS	BL21-Gold	LB	0.3	37	4

Constructs pET-pre01/DOHH and pET-pre01/DHS were provided by Dr. Sebastián Klinke. The pET-pre01 vector is a laboratory modified expression vector based on pET15b (Novagen). The vector features an N-terminal 6x His tag sequence followed by a PreScission Protease digestion site.

For the ^{57}Fe-hDOHH preparation, 20 mg ^{57}Fe metal foil was dissolved in 18% HCl. After removal of HCl, $^{57}Fe^{3+}$ dissolved in water was added to 2 L of M9 minimal medium.

2.2.3 Protein purification

2.2.3.1 GST-tagged protein purification

Protein purification was carried out at 4^{o}C for DOHH and room temperature for eIF-5A2. The bacterial pellet was lysed with a certain volume of lysis buffer

(PBS, 500 mM NaCl, pH 7.4, 2 mM DTT). Resuspended cells in lysis buffer were broken by sonication on ice. After ultracentrifugation for 1 h at 30,000 x *g* and 4^{o}C, the supernatant was loaded onto a GSTrap^{TM} column (GE Healthcare). The target protein was cleaved on the column by PreScission Protease (GE Healthcare) overnight and then eluted by gel filtration buffer (25 mM Tris-HCl, 150 mM NaCl, pH 7.5). The eluted protein was purified by repeated gel filtrations until the purity of the target protein (checked by SDS-PAGE or native PAGE) was satisfactory.

2.2.3.2 His-tagged protein purification

Protein purification was carried out at 4^{o}C for DOHH and room temperature for DHS. After completion of expression, the bacterial pellet was collected and suspended in a lysis buffer containing 500 mM NaCl, 20 mM Na_2HPO_4, 30 mM imidazole, and 1 mM DTT (pH 7.4). Cells in lysis buffer were broken by sonication on ice. After ultracentrifugation for 1 h at 30,000 x *g* and 4^{o}C, the supernatant was loaded onto a HisTrap^{TM} column (GE Healthcare). The target protein was eluted by an imidazole gradient (50 mM to 500 mM). The chromatographic fractions containing target protein were pooled and dialyzed against 1 L digestion buffer (150 mM NaCl, 50 mM Tris-HCl, pH 7.5, and 1 mM DTT) overnight. After dialysis, PreScission Protease (GE Healthcare) was added to the system. The cleavage was performed at 4°C for ~6 h. The PreScission Protease and uncleaved protein were removed by GSTrap^{TM} and HisTrap^{TM} columns. The purification procedure was completed by using a gel filtration column.

2.2.4 Native electrophoresis

All the native electrophoresis in this work was done by using 12% Tris-glycine polyacrylamide gels prepared in the laboratory. The electrophoresis was performed at 4°C and 100 V using Tris-glycine buffer (pH 8.0). For analysis of the DHS – eIF-5A complex, prior to being loaded to the native gel, the two

proteins were premixed and placed at room temperature for 30 min.

2.2.5 Atomic absorption spectra

The iron content of DOHH was analyzed by using an atomic absorption spectrometer (Hitachi). $Fe(NO_3)_3$ solution (Merck) was used for preparing a calibration curve. The protein was diluted with 0.5 M HNO_3. Each protein sample (at different concentration) and standard iron solutions were measured at least three times. The metal contents were calculated from the standard calibration curve.

2.2.6 UV/Vis spectra

A first measurement was carried out immediately after protein purification (after cleaving off the GST tag on the column) (at 4°C, 24 h after breaking the cells). Around 5 mg/ml wild-type DOHH in Tris-HCl buffer (25 mM Tris-HCl, 150 mM NaCl, pH 7.5) was used for time-dependent UV/Vis spectroscopic measurements. 1 ml protein solution in a quartz cuvette was covered by a layer of paraffin oil. The sample was stored at 10°C and measured every 2 h (in the first 12 h) or every 12 h (thereafter). Around 2 mg/ml protein in the same buffer was used for recording the UV/Vis spectra of wild-type and mutant enzymes shown in Fig. 3.14.

2.2.7 Mössbauer spectra

^{57}Fe-labeled hsDOHH in Tris-HCl buffer (see above) or in polycrystalline form was subjected to Mössbauer spectroscopy. Four different samples were measured: freshly isolated enzyme (prepared at 4°C), crystals grown from the fresh enzyme preparation (at 10°C, harvested 48 h after setting up the crystallization experiment), enzyme in glycerol-containing buffer (stored at 10°C for 48 h), and crystals grown in the presence of 10% glycerol (at 10°C, harvested 48 h after setting up the crystallization experiment). Crystals were grown by vapor diffusion in the Mössbauer cup at 10°C; 48 h after setting up

crystallization, liquid was taken out and crystals were washed three times with their crystallization buffers (see below). Crystals growing in the absence of glycerol did not attach to the bottom of the Mössbauer cup as tightly as those grown in the presence of glycerol; therefore, a considerate part of polycrystals was lost during the washing. Mössbauer spectra were recorded in a continuous-flow cryostat (Oxford Instruments) at 77 K in horizontal geometry using the constant acceleration mode. A proportional counter with argon-methane (9:1) filling was used. Spectra were recorded with a ^{57}Co source (ranging from ca. 0.3 GBq to 1.85 GBq, diffused in a Rh matrix) and calibrated against α-iron at room temperature. The experimental data were stored in a 512-channel analyzer and transferred to a PC where they were processed using the Vinda program package for Microsoft Excel developed by H.P. Gunnlaugsson (http://users-phys.au.dk/hpg/vinda.htm). Isomer shift (δ), quadrupole splitting (ΔE_Q), and line width Γ were obtained by least-square fits of Lorentzian lines to the experimental spectra using nested pairs. All values were rounded to the last given digit. Recording and analysis of Mössbauer spectra were carried out by Lars H. Böttger (Institute of Physics, University of Lübeck).

2.2.8 Crystallization, crystal optimization, diffraction data collection, structure determination, refinement, and validation

Crystallization screening was carried out by using a Phoenix crystallization robot (Art Robbins). Commercial kits from Sigma (basic and extension), Hampton Research (Crystal Screen I/II, PEGRx 1/2, PEG/Ion 1/2, SaltRx 1/2, and Index 1/2), and Qiagen (Complex Suite) were used for crystallization screening.

2.2.8.1 hsDOHH

Around 15 mg/ml hsDOHH (or truncated hsDOHH) was used for crystallization screening. Crystals of hsDOHH were observed under a condition composed of 30% PEG 6000 (w/v), 100 mM Bis-Tris propane (pH 9.0). Diffraction-quality

crystals were obtained from 30% PEG 6000 (w/v), 100 mM Bis-Tris propane (pH 7.2 - 7.4), 10 - 20% glycerol (in case of the GLC complex, see Section 3.1), and 400 mM guanidinium chloride (in case of the POX structure, Section 3.1). The crystals of the free enzyme (POX) grew within 6 h and those of the GLC complex within 36 h at 10^{o}C. 48 h after setting up the crystallization experiments, crystals were directly shock-cooled and stored in liquid nitrogen.

Diffraction data sets were collected at 100 K at beamline BL14.2 of BESSY II (Berlin, Germany) (Mueller *et al*., 2012) and processed with *iMOSFLM* (Battye *et al.*, 2011) (GLC structure, Section 3.1) or *autoPROC* (Vonrhein *et al*., 2011) (POX structure, Section 3.1) and scaled using *SCALA* (Evans, 2006). The structure of GLC was determined at 1.7 Å using the SAD method with anomalous dispersion from the iron atoms and the program *Auto-Rickshaw* (Panjikar *et al*., 2005); the structure of POX was solved at 1.7 Å by molecular replacement (Rossmann, 1990) using *MOLREP* (Vagin & Teplyakov, 1997) and GLC as the search model. Structure refinement was performed using *REFMAC5* (Murshudov *et al.*, 2011). For both the POX and GLC structures, no restraints were applied to the Fe-Fe and Fe-ligand distances and associated angles, but the O-O distance in the peroxo ligand in the POX structure and the geometry of glycerol in the GLC complex were restrained normally. Fe atoms, the sulfur atoms of M86 and M237, and ligating water molecules W1 - W3 (only in the POX structure) were refined with anisotropic temperature factors. During refinement, 5% of the reflections were set aside for the calculation of the free R-factor (Brünger, 1992). Model inspection and rebuilding were carried out manually using *Coot* (Emsley *et al*., 2010). Validation of the structural models was carried out by using *PROCHECK* (Laskowski *et al*., 1993) and *MolProbity* (Chen *et al*., 2010). Figures were prepared with PyMOL (Schrödinger).

2.2.8.2 scDOHH

20 mg/ml scDOHH was used for crystallization screening. Crystals of scDOHH

were observed under several similar conditions. Diffraction-quality crystals were obtained under an optimized condition consisting of 100 mM HEPES (pH 7.5), 200 mM $MgCl_2$, 25% PEG 4000, and 500 mM guanidinium chloride at 10^{o}C. One week after setting up the crystallization experiments, crystals were soaked in a cyro-solution consisting of 100 mM HEPES (pH 7.5), 200 mM $MgCl_2$, 27% PEG 4000, 500 mM guanidinium chloride, and 15% glycerol, and then shock-cooled and stored in liquid nitrogen.

Diffraction data were collected at beamline P11 of PETRA III (DESY, Hamburg, Germany) (Meents *et al*., 2013) at 100 K, processed with *XDSAPP* (Krug *et al*., 2012), and scaled using *SCALA* (Evans, 2006). The structure was determined at 2.1 Å by using molecular replacement with the hsDOHH POX structure as the search model. Model rebuilding and refinements were done with *Coot* (Emsley *et al*., 2010) and *REFMAC5* (Murshudov *et al*, 2011), respectively. Fe atoms were refined with anisotropic temperature factors. During refinement, 5% of the reflections were set aside for the calculation of the free R-factor (Brünger, 1992). Structural figures were prepared with PyMOL (Schrödinger).

2.2.8.3 pvDOHH

10 mg/ml pvDOHH was used for crystallization screening. Crystals of pvDOHH were observed under about 10 distinct conditions. Diffraction-quality crystals were obtained from 8% Tacsimate (a mixture of titrated organic acid salts) (pH 8.0), 18% PEG 3350, 1 mM $ZnCl_2$, and 800 mM NDSB-195 (dimethylethylammonium propane sulfonate) at 10^{o}C. The crystals appeared one week after starting the crystallization experiment. 10 days after setting up the crystallization experiments, crystals were soaked in a cryo-solution consisting of 8% Tacsimate (pH 8.0), 20% PEG 3350, 1 mM $ZnCl_2$, 800 mM NDSB-195, and 20% glycerol, and then shock-cooled and stored in liquid nitrogen.

Diffraction data were collected at beamline BL14.2 of BESSY II (Berlin, Germany) (Mueller *et al*., 2012) at 100 K, processed with *XDSAPP* (Krug *et al*., 2012), and scaled using *SCALA* (Evans, 2006). The structure was determined by using molecular replacement with the scDOHH structure as the search model. Model rebuilding and refinements were performed with *Coot* (Emsley *et al*., 2010) and *REFMAC5* (Murshudov *et al*, 2011), respectively. Fe atoms were refined with anisotropic temperature factors. During refinement, 5% of the reflections were set aside for the calculation of the free R-factor (Brünger, 1992). Structural figures were prepared with PyMOL (Schrödinger).

2.2.8.4 eIF-5A2

Truncated human eIF-5A2 (eIF-5A2-T16) (20 mg/ml) was used for crystallization screening. Diffraction-quality crystals were obtained under a condition consisting of 10% PEG 1500 and 100 mM Bicine (pH 8.6) at 10^{o}C. Before being cryo-cooled in liquid nitrogen, crystals were soaked in a cryo-solution consisting of 15% PEG 1500, 100 mM Bicine (pH 8.6), and 25% glycerol.

Diffraction data were collected at beamline P11 of PETRA III (DESY, Hamburg, Germany) (Meents *et al*., 2013) at 100K, processed with *XDSAPP* (Krug *et al*., 2012), and scaled using *SCALA* (Evans, 2006). The structure was determined by using molecular replacement with the N-terminal domain of eIF-5A1 (PDB code: 3CPF, Tong *et al*., 2009) as the search model. Model rebuilding and refinement were carried out using *Coot* (Emsley *et al*., 2010) and *REFMAC5* (Murshudov *et al*, 2011), respectively. During refinement, 5% of the reflections were set aside for the calculation of the free R-factor (Brünger, 1992). The dimerization interface of eIF-5A2 was analyzed using the PISA server (http://www.ebi.ac.uk/msd-srv/prot_int/, Krissinel & Henrick, 2007). Structural figures were prepared with PyMOL (Schrödinger).

2.2.8.5 DHS – eIF-5A1-N complex

A mixture of DHS (around 5 mg/ml) and eIF-5A1-N (at a molar ratio of one DHS tetramer : two eIF-5A1-N) in a low-ironic-strength buffer consisting of 20 mM NaCl, 10 mM Tris-HCl (pH 7.5), and 30% glycerol was used for crystallization. Crystals were obtained by using sitting-drop vapor diffusion at 4^{o}C with 500 mM NaCl as reservoir solution. In order to confirm that the crystals contained protein complex, 10% of the eIF-5A1-N was covalently labeled with a fluorescent probe (carboxyrhodamine, Molecular Dimensions).

Diffraction experiments were carried out at beamline P11 of PETRA III (DESY, Hamburg, Germany) (Meents *et al*., 2013) at 100 K.

2.2.9 Density functional theory (DFT) calculations

Density functional theory (DFT) calculations were carried out by Lars H. Böttger (Institute of Physics, University of Lübeck). The input models for the diiron core of hsDOHH were prepared on the basis of crystal structures of hsDOHH (POX and GLC). Both iron atoms and surrounding ligands were included in the model structures. The density functional theory (DFT) calculations were performed by using the *ORCA* program package (Neese, 2012). Geometry optimization procedure includes the quick and the accurate optimization by using TZV/BP86/SV (Perdew, 1986; Becke, 1988; Schäfer *et al*., 1992; Schäfer, 1994) and TZV/BP86/TZV(P)/TZV(2d). The Mössbauer parameters (isomer shift δ and quadrupole splitting ΔE_Q) and exchange coupling constant J (Noodleman, 1981) were calculated with the B3LYP function (Lee *et al*., 1988; Becke, 1993; Stephens, 1994) on the basis of geometry-optimized model structures.

2.2.10 Automated docking

The preparation of the target protein structure and the ligands was carried out by using AutoDock Tools (version 1.5.6) and docking was performed by

AutoDock (version 4.2) (Morris *et al*., 2009). The crystal structure of hsDOHH (POX) was used as the target protein. Iron ions were included in the docking grid, with their charges set to +1. Iron ligands His56, His89, His207, and His240 were deprotonated. The grid box included the entire inner cavity and part of the external cavity. Structures of Dhp and Hpu were created by using the *PRODRG* server (Schüttelkopf & van Aalten, 2004).

3. Results and Discussions

3.1 Human deoxyhypusine hydroxylase

The results of hsDOHH in the thesis have been published in part as:

Han, Z., Sakai, N., Böttger, L.H., Klinke, S., Hauber, J., Trautwein, A.X., Hilgenfeld, R. (2015). Crystal structure of the peroxo-diiron(III) intermediate of deoxyhypusine hydroxylase, an oxygenase involved in hypusination. *Structure* **23**, 882-892.

3.1.1 His-tagged recombinant hsDOHH production and crystallization

As shown in Fig. 3.1 A, a considerable amount of recombinant His-tagged hsDOHH was obtained. After cleaving off the His tag (Fig. 3.1 B), hsDOHH was analyzed by size-exclusion chromatography (Fig. 3.1 C). The protein from the main peak (peak 3, eluted last from the Superdex^{TM} 75 column) showed light blue color, indicating that the main peak contained holo-hsDOHH. Although an SDS-PAGE suggested that the protein from the main peak was pure (Fig. 3.1 D), it still contained a significant amount of apo-hsDOHH as revealed by native electrophoresis (Fig. 3.1 E). This isolated hsDOHH could not be crystallized, although it displayed a narrow size distribution in dynamic light-scattering (DLS) (Fig. 3.1 F). The failure to crystallize this protein was probably due to the proportion of holo-hsDOHH being too low to be separated from apo-hsDOHH.

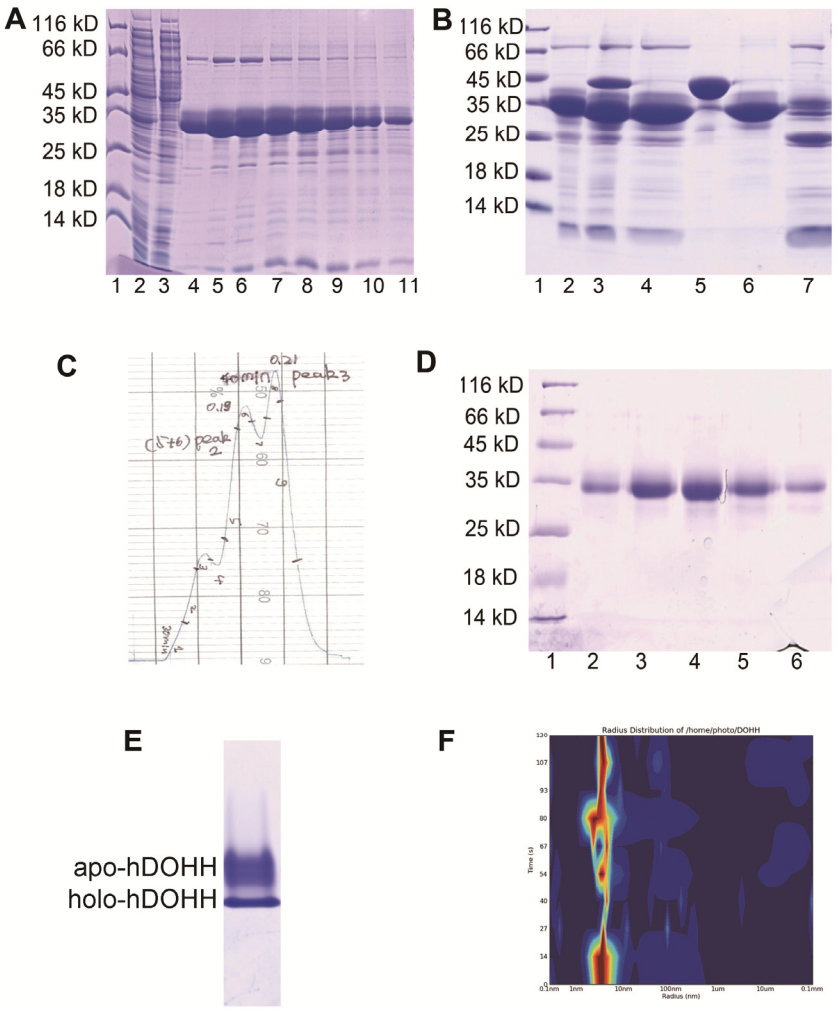

Fig. 3.1 Purification of His-tagged hsDOHH.
(A) Analysis of fractions from the HisTrap™ column by SDS-PAGE. Lane 1: protein marker; lane 2: supernatant of broken expression cells; lane 3: flow-through of HisTrap™ column; lanes 4 - 11: fractions eluted by imidazole gradient.
(B) Cleavage of the His tag and removal of the PreScission Protease (GST-fusion). Lane 1: protein marker; lane 2: His-tagged hsDOHH from HisTrap™ column; lane 3: hsDOHH after cleavage of His-tag; lane 4: hsDOHH after removal of PreScission Protease by GSTrap™ column; lane 5: PreScission Protease; lane 6: protein after removal of hsDOHH with uncleaved His-tag; lane 7: hsDOHH with uncleaved His-tag and impurities.
(C) Isolation of holo-hsDOHH on a Superdex™ 75 column. The protein in the main peak (peak 3) showed blue color.
(D) Analysis of protein in the main peak by SDS-PAGE.
(E) The final isolated holo-hsDOHH in native PAGE. Upper band: apo-hsDOHH; lower band: holo-hsDOHH.
(F) Dynamic light-scattering (DLS) result with final isolated hsDOHH.

3.1.2 GST-tagged recombinant hsDOHH production and crystallization

Since the His-tagged expression construct did not produce a high amount of holo-hsDOHH, a GST-tagged expression construct was applied for production of the enzyme. Fig. 3.2 A shows a gel filtration chromatogram of hsDOHH after cleavage of the GST tag. It can be seen that the recombinant protein contained a much larger proportion of iron-containing holo-hsDOHH (main peak, which eluted last) (Fig. 3.2 A, left) compared to the recombinant protein obtained from the His-tagged expression construct. The fractions containing holo-hsDOHH were collected for a second-round gel filtration experiment. In the latter, only one peak corresponding to holo-hsDOHH appeared, indicating that apo-hsDOHH had been almost totally removed (Fig. 3.2 A, right). An SDS-PAGE showed that the hsDOHH was highly pure (Fig 3.2 B, top) and only a small amount of apo-hsDOHH was present in the final purified enzyme as shown in native PAGE (Fig. 3.2 B, bottom). Unusually, there were two bands of similar size appearing in both the SDS-PAGE and the native PAGE (Fig. 3.2 B).

DLS analysis indicated that the quality of this purified hsDOHH was much higher than that of the protein from the His-tagged expression construct (Fig. 3.2 C). In addition, the newly purified hsDOHH displayed dark blue color (Fig. 3.2 D). A crystallization hit was obtained by screening with commercial kits (Fig. 3.2 E, left). The primary crystallization condition consisted of 100 mM Bis-Tris propane (pH 7.5) and 30% PEG 6000. The crystals were protein crystals as confirmed by using the Izit^{TM} crystal dye (differentiates biological macromolecule crystals from salt crystals) (Hampton Research) (Fig. 3.2 E, right). After several rounds of optimization, the crystals were still tiny and multi-crystals, even though 96 crystallization additives had been tried.

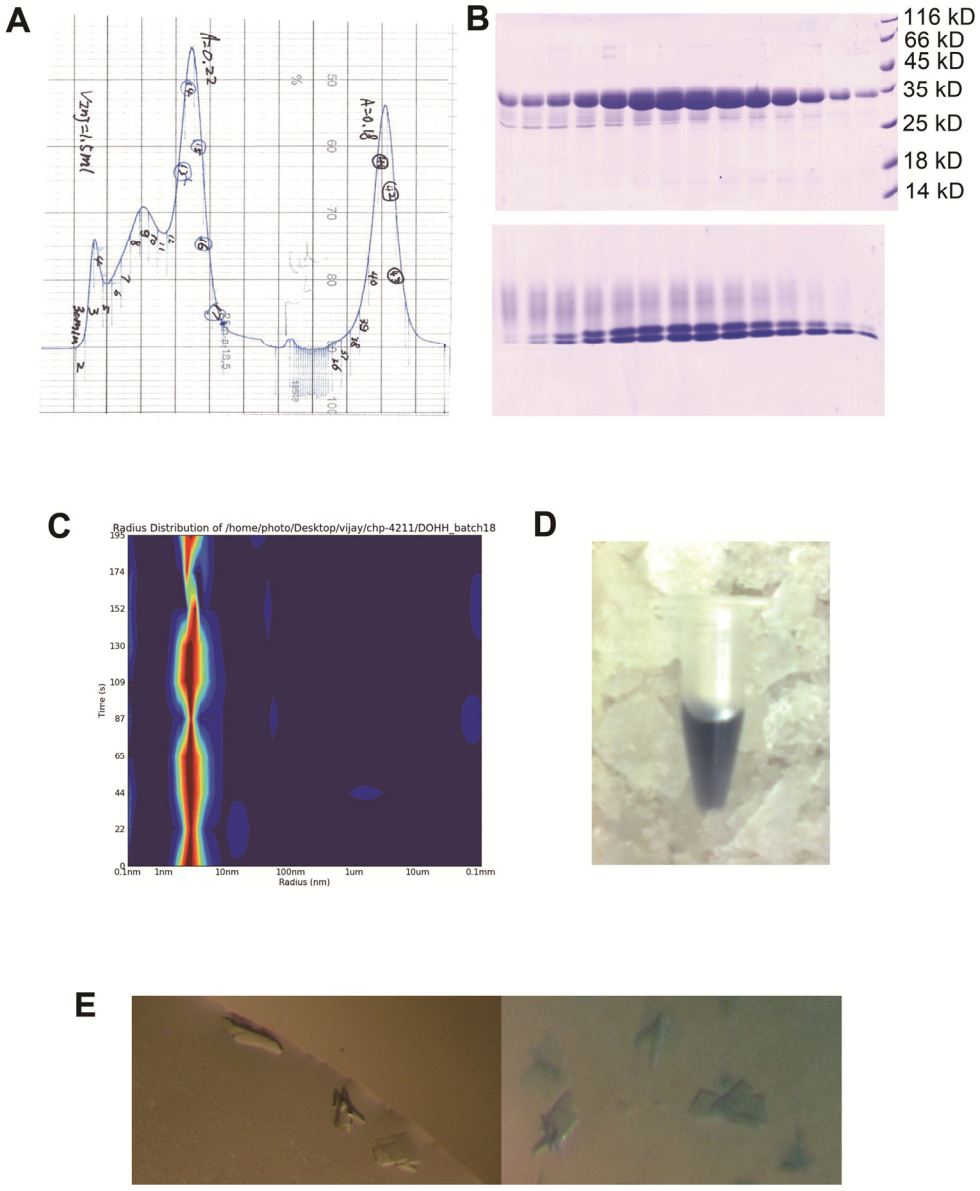

Fig. 3.2 Recombinant hsDOHH production with the GST-tagged expression construct, purification, and crystallization.
(A) Separation of holo-hsDOHH from apo-hsDOHH by gel filtration (Superdex^{TM} 75 column). Chromatographic fractions containing holo-hsDOHH from the first round of gel filtration were pooled and reloaded onto the column for a second round of purification. Right: first round; left: second round.
(B) The chromatographic fractions from the second round of gel filtration were analyzed by SDS-PAGE (top) and native PAGE (bottom).
(C) DLS analysis of purified hsDOHH.
(D) The color of purified hsDOHH.
(E) Crystals of hsDOHH before (left) and after (right) staining with Izit^{TM} crystal dye (Hampton Research) (protein crystal: blue; salt crystal: colorless).

The difficulties encountered in the crystal optimization step were likely caused

by heterogeneity in the size of purified hsDOHH as shown in Fig. 3.2 B. The two bands appearing in SDS-PAGE and native PAGE were very close to one another, therefore, they could not be separated. At least one of them corresponds to recombinant hsDOHH and the other one could be an impurity or recombinant hsDOHH of a different length. The proteins from each of the bands in the SDS-PAGE and the native PAGE (Fig. 3.3) were excised for N-terminal sequencing. The N-terminal sequencing showed that the proteins from all the bands were recombinant hsDOHH and shared an identical N-terminus. Further investigation by using matrix-assisted laser desorption-ionization time-of-flight mass spectrometry (MALDI-TOF-MS) revealed that the lower band (MW: 33.3085 kDa) corresponded to full-length recombinant hsDOHH (theoretical MW: 33.2 kDa), whereas the upper band (MW: 34850.3 kD) is larger than the full-length enzyme. The reason for production of the enlarged recombinant hsDOHH was probably that the ribosomes read through the stop codon (Fig. 3.4).

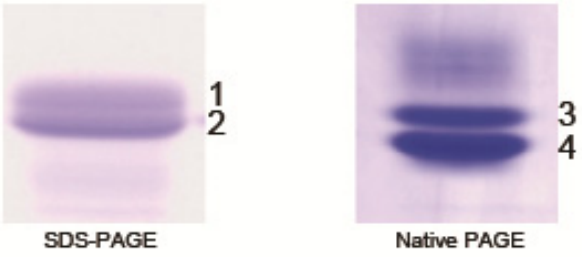

Fig. 3.3 Samples for N-terminal sequencing. Bands 1-4 were excised from the PAGE gel for individual sequencing (performed by Dr. Buko Lindner and his colleagues, Research Center Borstel, Borstel, Germany).

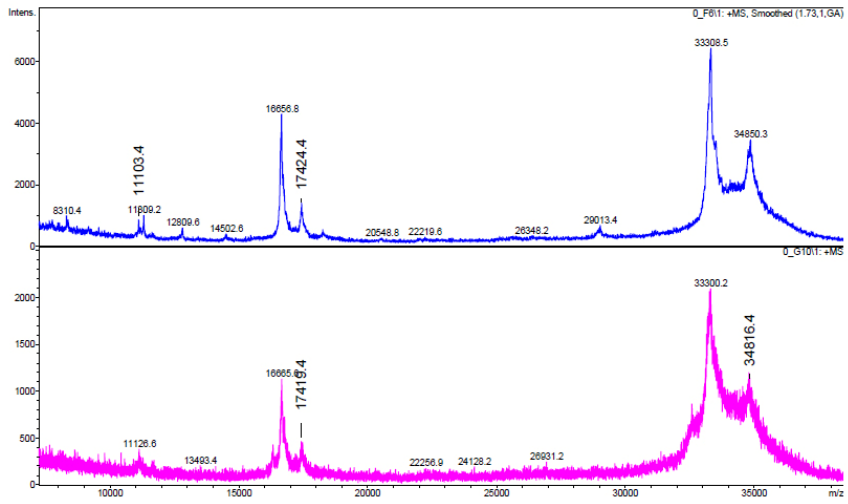

Fig. 3.4 MALDI-TOF mass spectrometry of recombinant hsDOHH (performed by Dr. Buko Lindner and his colleagues, Research Center Borstel, Borstel, Germany)**.**

Assuming that the heterogeneity problem occurred at the C-terminus of the protein, step-wise truncation of the C-terminus of hsDOHH was applied for enzyme production. All of the C-terminally truncated hsDOHH preparations did not show the double-band issue of full-length hsDOHH. Fig.3.5 shows the SDS-PAGE and native PAGE results for the truncated hsDOHH.

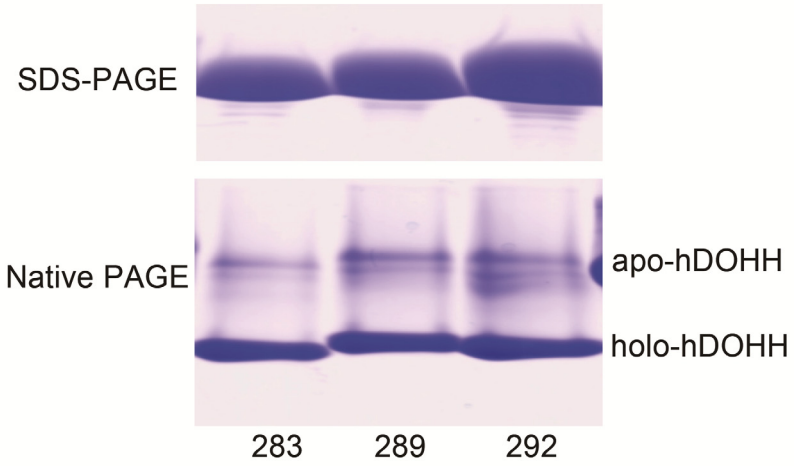

Fig. 3.5 Purified recombinant hsDOHH with different C-termini in SDS-PAGE and native PAGE. The hsDOHH was truncated at Glu283, Gln289, or Asp292.

A construct truncated at Gln289 gave rise to the best crystallization hit. This construct was used for protein crystallization and the following studies. The

primary crystallization condition was the same as the condition found for full-length hsDOHH. However, diffraction-quality crystals were obtained by using two crystallization additives. Crystals growing in 100 mM Bis-tris propane (pH 7.2), 30% PEG6000, and 400 mM guanidinium chloride were obtained within 6 h after setting up the crystallization experiment, grew to their maximum size within ~48 h, and were of weak blue color (Fig. 3.6 A). When the guanidinium chloride was replaced by 10 – 20% glycerol, the crystals grew much more slowly (obtained within 36 h) and were mostly colorless to light brownish (Fig. 3.6 B).

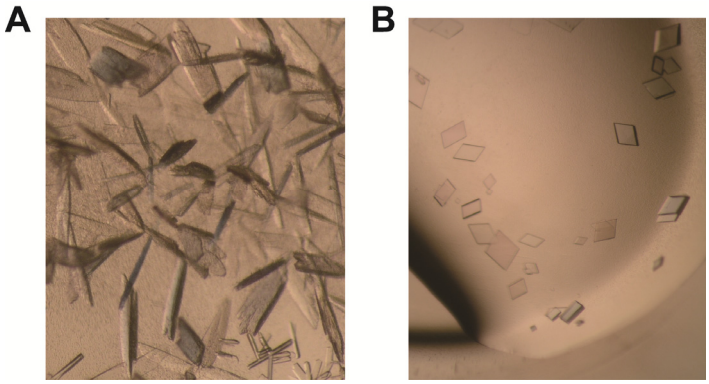

Fig. 3.6 Crystals of hsDOHH (truncated at Gln289). The images were taken three days after setting up the crystallization.
(A) Crystals obtained in 100 mM Bis-tris propane (pH 7.2), 30% PEG6000, and 400 mM guanidinium chloride.
(B) Crystals obtained in 100 mM Bis-tris propane (pH 7.2), 30% PEG6000, and 15% glycerol.

3.1.3 Spectroscopic studies of hsDOHH

The characteristic bluish color of hsDOHH (Vu *et al.*, 2009) showed up immediately after breaking the expression cells. The color persisted during the process of protein purification at 4^{o}C. Even if the protein purification time for individual batches varied from 2 to 5 days, the same profiles in the UV/Vis spectra were observed. Time-dependent UV/Vis spectra recorded at 10^{o}C (the temperature of crystallization) revealed that the absorption band at long wavelengths was blue-shifted from λ_{max} ~630 nm to λ_{max} ~ 600 nm within ~96 h,

concomitant with a reduction of molar absorptivity (Fig. 3.7 A); at room temperature, this effect was somewhat stronger. The persisting, albeit weaker, blue color of this hsDOHH solution indicated the continued presence of a peroxo-diiron(III) species. Similar blue-shifts of the maximum absorbance coupled with reduced molar absorptivity have been ascribed to changes in the protonation state or to a carboxylate shift in the peroxo-diiron(III) core, for instance in ferritin (Bou-Abdallah *et al.*, 2005) or in synthetic model compounds (Zhang *et al.*, 2005; Frisch *et al.*, 2009). From inspecting UV/Vis spectra, it is likely that due to a similar process, more than one peroxo-diiron(III) species is present in hsDOHH after activation by O_2.

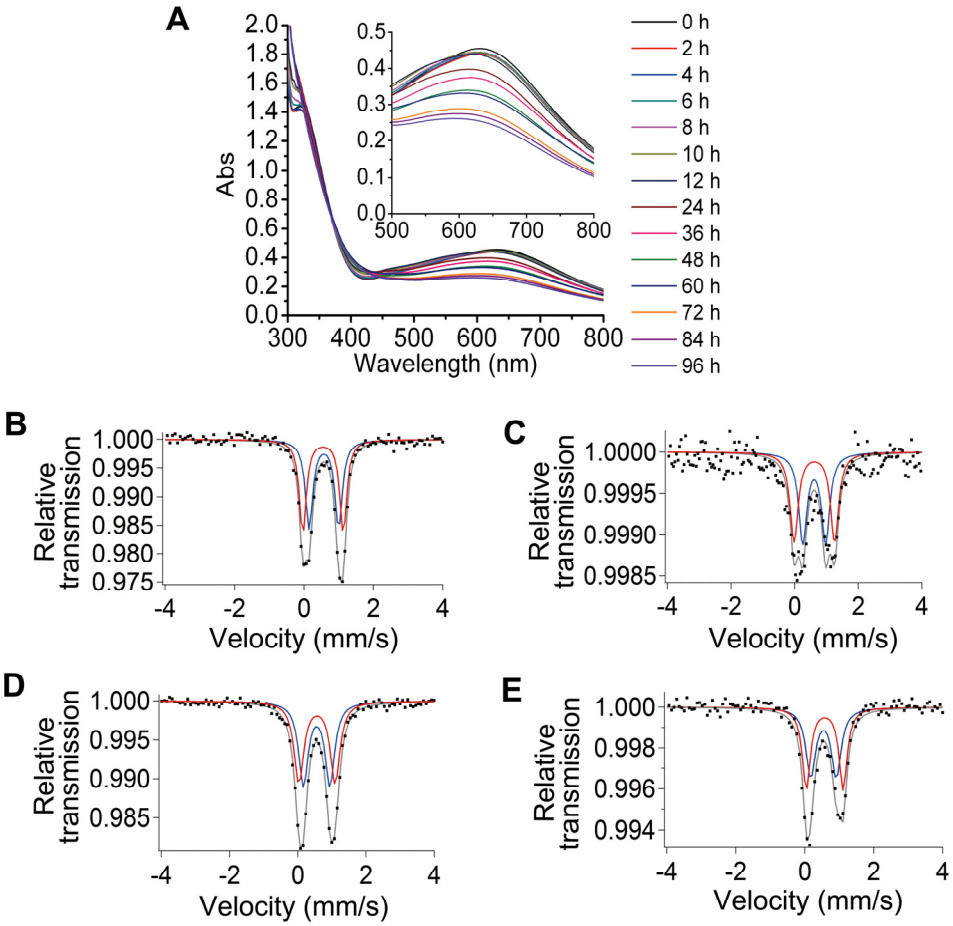

Fig. 3.7 Spectroscopic studies of hsDOHH.

(A) Time-dependent UV/Vis absorption spectra recorded at 10°C. The inset shows a magnification of the absorption peak at long wavelengths.

(B) Mössbauer spectrum of freshly isolated hsDOHH in solution. The Mössbauer parameters are almost identical to those reported by Vu *et al.* (2009): δ_1 = 0.57 mm s^{-1}, $\Delta E_{Q,1}$ = 0.85 mm s^{-1}, Γ_1 = 0.27 mm s^{-1}; δ_2 = 0.55 mm s^{-1}, $\Delta E_{Q,2}$ = 1.17 mm s^{-1}, Γ_2 = 0.24 mm s^{-1}.

(C) Mössbauer spectrum of hsDOHH polycrystals. The crystallization conditions were the same as for crystals used for X-ray diffraction (see Fig. 3.6 A). δ_1 = 0.62 mm s^{-1}, $\Delta E_{Q,1}$ = 0.71 mm s^{-1}, Γ_1 = 0.28 mm s^{-1}; δ_2 = 0.62 mm s^{-1}, $\Delta E_{Q,2}$ = 1.25 mm s^{-1}, Γ_2 = 0.26 mm s^{-1}.

(D) Mössbauer spectrum of hsDOHH in solution, in the presence of 10% glycerol. δ_1 = 0.55 mm s^{-1}, $\Delta E_{Q,1}$ = 0.77 mm s^{-1}, Γ_1 = 0.33 mm s^{-1}; δ_2 = 0.56 mm s^{-1}, $\Delta E_{Q,2}$ = 1.06 mm s^{-1}, Γ_2 = 0.34 mm s^{-1}.

(E) Mössbauer spectrum of hsDOHH polycrystals (crystallized in glycerol-containing conditions). The crystallization conditions were the same as for crystals used for X-ray diffraction (see Fig. 3.6 B). δ_1 = 0.54 mm s^{-1}, $\Delta E_{Q,1}$ = 0.74 mm s^{-1}, Γ_1 = 0.33 mm s^{-1}; δ_2 = 0.58 mm s^{-1}, $\Delta E_{Q,2}$ = 1.07 mm s^{-1}, Γ_2 = 0.28 mm s^{-1}.

In order to characterize possible changes at the diiron site in the crystalline state, polycrystals were prepared of the free enzyme as isolated and of the glycerol-containing sample and subjected to Mössbauer spectroscopy. Freshly isolated hsDOHH in solution was measured in parallel as a reference. The latter gave Mössbauer parameters δ_1 = 0.57 mm s^{-1}, $\Delta E_{Q,1}$ = 0.85 mm s^{-1}, Γ_1 = 0.27 mm s^{-1}; δ_2 = 0.55 mm s^{-1}, $\Delta E_{Q,2}$ = 1.17 mm s^{-1}, Γ_2 = 0.24 mm s^{-1} (Fig. 3.7 B), almost identical to the results reported by Vu *et al.* (2009). This spectrum shows very narrow line widths, suggesting that the purified hsDOHH sample contained a highly homogenous peroxo-diiron(III) species. Crystals grown of the recombinant enzyme as isolated gave rise to a Mössbauer spectrum slightly different from that obtained from freshly prepared hsDOHH in solution (Fig. 3.7 C): isomer shifts δ_1/δ_2 (0.62 mm s^{-1} / 0.62 mm s^{-1}, $\Delta E_{Q1/2}$ = 0.72 mm s^{-1} / 1.25 mm s^{-1}) were slightly larger than those from freshly prepared hsDOHH in solution; the narrow line widths, however, indicate that the investigated polycrystalline sample contained also a highly homogenous iron species. The procedure of growing crystals within a given time window (48 h) and subsequent washing of the crystals with buffer (see Materials and Methods) set limits to the measured signal-to-noise-effect (ca. 0.3%). The crystals grown in the presence of glycerol gave Mössbauer parameters almost identical to a sample of the enzyme in solution containing 10% glycerol (Fig. 3.7 D & E), which are, however, different from preparations of the free enzyme. The spectra shown in Fig. 3.7 D and E imply that glycerol likely induces some change at the diiron site of hsDOHH. Interestingly, glycerol has been found to accelerate the decay of the peroxo-diiron(III) species in sMMOH, but the reason is unclear (Lee & Lipscomb, 1999). The Mössbauer spectra of hsDOHH preparations in glycerol-containing conditions (in solution and crystals) also exhibit relatively narrow line widths, suggesting that an almost pure diiron species was present in the preparations. Although the Mössbauer spectra of samples in glycerol-containing conditions are different from freshly isolated hsDOHH in solution and in polycrystals obtained in absence of

glycerol, all of them suggest the presence of two antiferromagnetically coupled, high-spin Fe(III) atoms.

3.1.4 Structure determination and refinement

The structure of crystals grown from a glycerol-containing solution was determined by applying the single-wavelength anomalous dispersion (SAD) method using the anomalous signal from the iron atoms. The structure of crystals obtained from freshly prepared, recombinant enzyme was solved by molecular replacement using the former structure as the search model. Both structures have a resolution of 1.7 Å. The two crystal forms share the same space group but display different unit-cell parameters. The refined structures feature two different states of the diiron core, the peroxo-diiron(III) intermediate ("POX") in the freshly prepared recombinant enzyme and a glycerol-bound diiron complex ("GLC") in the crystals grown in the presence of glycerol. Table 3.1 shows a summary of diffraction data collection, phase determination, and structure refinement.

Table 3.1 Crystallographic data and refinement statistics

	Crystal 1 (GLC) (peak)	Crystal 2 (GLC)	Crystal 3 (POX)
Diffraction data statistics			
X-ray source	BL14.2, BESSY II	BL14.2, BESSY II	BL14.2, BESSY II
Wavelength, Å	1.73965	0.91841	0.91841
Space group	$P2_1$	$P2_1$	$P2_1$
Unit cell parameters, Å, deg.	a = 45.97, b = 70.22, c = 101.00, β =102.57	a = 46.05, b = 70.18, c = 101.28, β = 102.71	a = 45.93, b = 48.64, c = 124.09, β = 99.27
Resolution range, Å [1]	27.6-1.90 (2.00-1.90)	44.92-1.70 (1.79-1.70)	19.85-1.70 (1.79-1.70)
Reflections	328,812 (44,594)	269,456 (26,602)	193,329 (30,445)
Unique reflections	49,878 (7,266)	68,054 (8,949)	57,441(8,631)
R_{merge} [2]	0.075 (0.260)	0.037 (0.174)	0.049 (0.237)
R_{pim} [3]	0.031 (0.116)	0.021 (0.121)	0.032 (0.148)
$CC_{1/2}$ [4]	0.997 (0.894)	0.999 (0.962)	0.998 (0.938)
$I/\sigma(I)$	17.1 (6.9)	23.5 (6.0)	14.0 (4.3)
Redundancy	6.6 (6.1)	4.0 (3.0)	3.4 (3.5)
Completeness, %	99.8 (99.8)	98.2 (89.0)	96.2 (99.7)
Wilson B factor, Å^2	20.6	17.2	14.9
SigAno [5]	2.00		
FOM (DM FOM) [6]	0.694 (0.855)		
Refinement statistics			
Refinement resolution range, Å		19.95-1.70	19.85-1.70
No. reflections		64,571	54,485
R_{work}/R_{free} (% refls.) [7]		0.171/0.194 (5.0)	0.203/0.246 (5.0)
Average B factor, Å^2		20.67	18.90
No. of atoms			
Protein		4399	4410
Water		335	440
Other		37	28
R.m.s. deviations			
Bond lengths, Å		0.022	0.018
Bond angles, deg.		2.007	1.769
Ramachandran favored, %		100.00	99.30
Ramachandran outliers, %		0.00	0.00
MolProbity score [8]		1.58	1.78

[1] The highest resolution shell is shown in parenthesis.

[2] $R_{merge} = \Sigma_{hkl}\Sigma_i|I_i(hkl) - \langle I_i(hkl)\rangle| / \Sigma_{hkl}\Sigma_i\, {}^{Ii(hkl)}$

[3] Precision-indicating merging R factor. R_{pim} is defined as $\Sigma_{hkl}[1/(N-1)]^{1/2}\,\Sigma_i|I_i(hkl) - \langle i(hkl)\rangle| / \Sigma_{hkl}\Sigma_i\, {}^{Ii(hkl)}$, N is the redundancy (Weiss & Hilgenfeld, 1997).

[4] Correlation coefficient between two random-half data sets (Karplus & Diederichs, 2012).

[5] SigAno is defined as $[|F(+) - F(-)|] / \sigma$. F(+) and F(-) are structure factor estimates obtained from the merged intensity observations in each parity class.

[6] Figure of merit (FOM) before and after density modification (DM). FOM is defined as $|F_{hkl}(best)| / |F_{hkl}|$.

[7] $R_{work} = \sum_{hkl}|F_{obs} - F_{calc}| / \sum_{hkl}F_{obs}$. R_{free} serves as cross-validation of the R-factor. 5% of the reflections were set aside for the calculation of the free R-factor (Brünger, 1992).

[8] log-weighted combination of the clash-score, percentage of non-favored conformations according to the Ramachandran plot, and percentage of bad side-chain rotamers (Chen *et al.*, 2010).

3.1.5 Overall structure of hsDOHH

Both structures (POX and GLC) show an almost identical overall architecture. There are two hsDOHH monomers (A and B) per asymmetric unit. The overall structure of the hsDOHH monomer comprises a pseudosymmetric arrangement of an N-terminal and a C-terminal domain, each consisting of 4 HEAT repeats (α-hairpins), accounting for a total of 16 α-helices, as predicted by sequence analysis (Park *et al.*, 2006) (Fig. 3.8). There is no related structure in the Protein Data Bank with 4 + 4 HEAT repeats. In each of the two domains, the four HEAT motifs stack on top of each other, with odd-numbered α-helices (1, 3, 5, 7, and 9, 11, 13, 15) being arranged in parallel to one another and located towards the exterior of the protein, and even-numbered α-helices (2, 4, 6, 8, and 10, 12, 14, 16) also arranged in parallel to one another and located in the middle of the protein (Fig. 3.8).

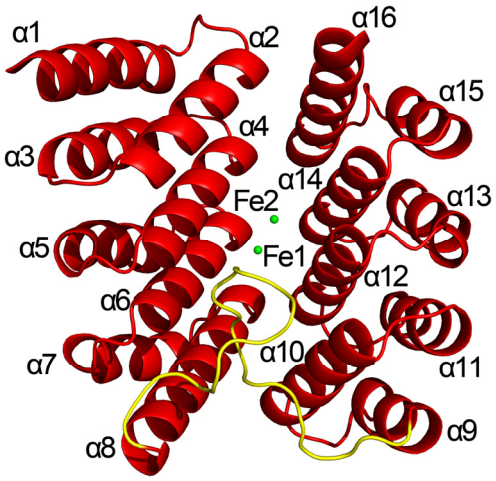

Fig. 3.8 Structure of hsDOHH. Helices are labeled. Yellow, inter-domain loop; green, iron atoms.

A significant deviation between the POX and GLC structures exists at the C-terminal helices, in particular α16 (Fig. 3.9). The reorientation of α16 by an angle of around 15° results in a difference of 6.07±0.15 Å for the C-terminal residue, Glu283, of this helix (for the Cα position; averaged between the two copies in the asymmetric unit).

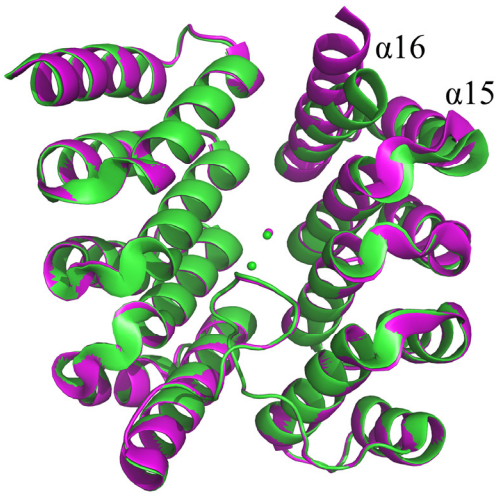

Fig. 3.9 Alignment of the POX and GLC structures. POX and GLC are presented in magenta and green, respectively.

The interior α-helix layers from the two domains pack against each other at an angle of approximately 45°, leaving an opening that runs along the interface in the middle of the protein. The N-terminal and the C-terminal domains share 36% sequence identity (53% similarity) (Fig. 3.10) and the structures of the two domains can be superimposed with an r.m.s. difference of about 0.95 Å (on Cα positions), strongly suggesting that hsDOHH evolved through gene duplication. The two domains are connected by a long loop (residues 136 - 157), the conformation of which is very well conserved between the four copies of hsDOHH (POX and GLC) elucidated within this study (Fig. 3.8). The loop invaginates into the interior of the protein where it is involved in several electrostatic interactions.

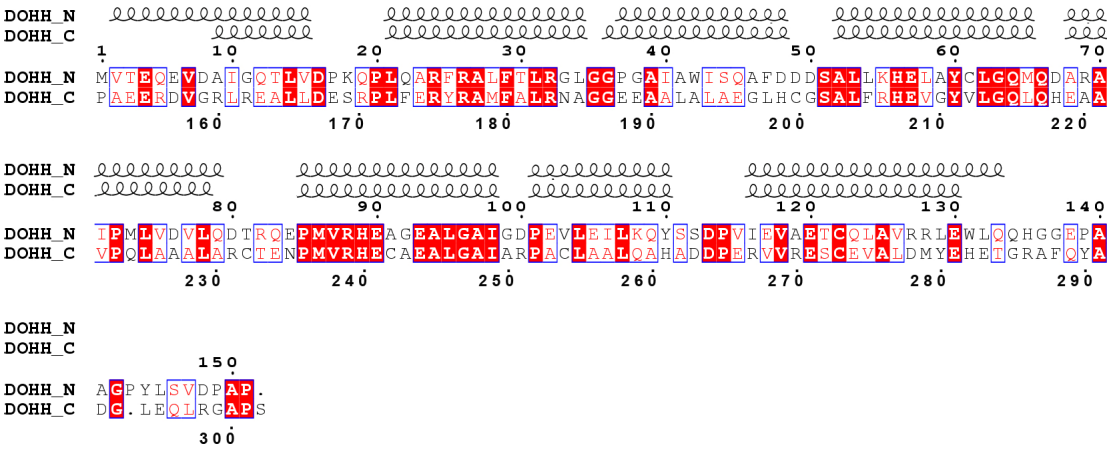

Fig. 3.10 Structure-based alignment of the amino-acid sequences of the N-terminal and C-terminal domains of hsDOHH. The secondary structure for each domain is displayed above the sequences.

In both structures, the diiron catalytic center of hsDOHH is located between the two domains, near the helix pairs α4/α6 and α12/α14, in an orientation parallel to the axis between the two staples of HEAT repeats (Fig. 3.8).

3.1.6 Diiron core of hsDOHH

Diiron centers of the POX and GLC structures share the same ligand set of amino-acid side chains. Each iron is coordinated by two histidine residues (through their Nε atoms) and one glutamate, i.e. the diiron center of hsDOHH displays a histidine-rich coordination, 4H-2E (Fig. 3.11 A). Fe1 is coordinated by H89, E90, and H207, and Fe2 is coordinated by H56, H240, and E241. In previous mutagenesis work, all of these residues were found to be essential for maintaining iron content and activity of the enzyme (Kim *et al.*, 2006). All amino-acid ligands of the Fe atoms are monodentate; distinct from other diiron enzymes (Nordlund & Eklund, 1995; Summa *et al.*, 1999), there is no bridging glutamate. The coordinative bonds to the carboxylate oxygens range from 1.99 to 2.10 Å, whereas the Fe-N bonds are between 2.18 and 2.34 Å. All four histidines coordinate to the same hemisphere of the diiron core and the four Nε atoms from histidines are approximately arranged in one plane (Fig. 3.11 B).

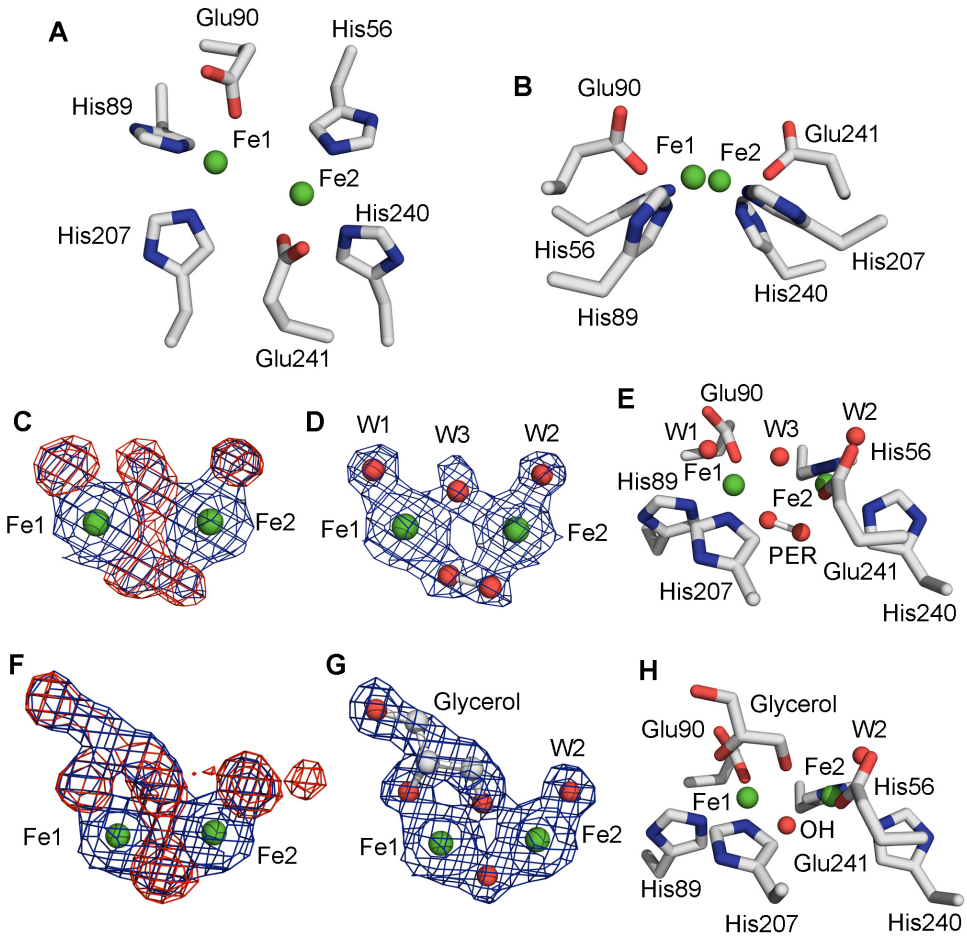

Fig. 3.11 Electron-density maps and coordination geometry of the diiron core of hsDOHH (molecule A). Carbon, nitrogen, oxygen, and iron atoms are presented in gray, blue, red, and green, respectively. W1, water coordinating to Fe1; W2, water coordinating to Fe2; W3, bridging water; PER, peroxide ion.
(A) Amino-acid residues as diiron core ligands in hsDOHH.
(B) As in (A), in another orientation (180° counter-clockwise rotation of (A), viewed from the side of His89 and His207). The histidine ligands of the diiron core occupy the lower coordination hemisphere.
(C) Electron density around the iron atoms in chain A of the POX structure, before building the non-protein ligands: magenta, F_o-F_c map (contoured at 4.0σ); blue, $2F_o$-F_c map (at 1.0σ).
(D) Electron-density map of the diiron core in chain A of the POX structure after ligand inclusion and refinement ($2F_o$-F_c map, at 1.5σ, blue mesh).
(E) The diiron core in chain A of the POX structure, with the non-protein ligands included.
(F) As in (C), for the GLC structure.
(G) As in (D), for the GLC structure.
(H) As in (E), for the GLC structure.

In the POX structure, the distance between the two Fe atoms is 3.77 and 3.68

Å in the two copies of enzyme. In a cavity within the histidine coordination hemisphere, well-defined difference density was detected that can be clearly assigned to a peroxo ligand in an orientation roughly but not exactly parallel to the Fe---Fe axis (Fig. 3.11 C & D; 3.12 A & B). This presumable O_2^{2-} species bridges the irons as a μ-1,2-ligand at distances of 2.23/2.21 Å (Fe1) and 2.18/2.17 Å (Fe2) (Fig. 3.11 E; Table 3.2). The O-O bond length is 1.54/1.52 Å (for molecules A and B, resp.), and the B factors for the individual oxygens are almost equal to one another (Table 3.2). In addition, on the opposite side of the Fe---Fe axis, in the "upper" coordination sphere of the diiron core of the structure, there are three water molecules (W1, W2, and W3) coordinating to diiron, with W3 bridging the two irons.

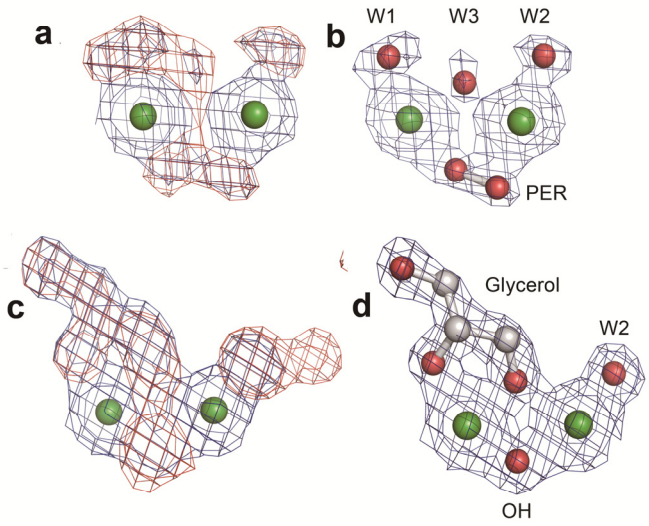

Fig. 3.12 Electron-density maps of the diiron core in molecule B of the POX and GLC structures. Carbon, nitrogen, oxygen, and iron atoms are presented in gray, blue, red, and green, respectively. W1, water coordinating to Fe1; W2, water coordinating to Fe2; W3, bridging water; PER, peroxide ion. See Fig. 3.11 for molecule A of both structures.
(A) Electron density around the iron atoms in chain B of the POX structure, before building the non-protein ligands; magenta, F_o-F_c map (contoured at 4.0 σ); blue, $2F_o$-F_c map (at 1.0 σ).
(B) Electron-density map of the diiron core in chain B of the POX structure after ligand inclusion and refinement ($2F_o$-F_c map, at 1.5 σ, blue mesh).
(C) as in (A), for the GLC structure.
(D) as in (B), for the GLC structure.

Table 3.2 Selected geometric parameters and atomic temperature factors around the diiron core of hsDOHH

		POX[1] chain A	POX chain B	GLC[2] chain A	GLC chain B
Distance, Å	Fe-Fe	3.77	3.68	3.44	3.48
	Fe1-O1, PER[3]	2.23	2.21		
	Fe2-O2, PER	2.18	2.17		
	O-O, PER	1.54	1.52		
	Fe1-O, μ-OH			2.05	1.95
	Fe2-O, μ-OH			2.21	2.22
	Fe1-N, H89	2.24	2.23	2.22	2.22
	Fe1-N, H207	2.27	2.23	2.18	2.18
	Fe1-OE2, E90	2.06	2.10	2.03	2.10
	Fe2-N, H56	2.33	2.34	2.24	2.26
	Fe2-N, H240	2.20	2.29	2.29	2.29
	Fe2-OE2, E241	2.10	1.99	2.00	1.99
	Fe1-W1[4]	2.18	2.12		
	Fe1-W3[5]	2.14	2.15		
	Fe2-W2[6]	2.16	2.18	2.09	2.02 Å
	Fe2-W3	2.38	2.19		
	Fe1-O3, GOL[7]			2.08	2.07
	Fe1-O2, GOL			2.18	2.19
	Fe2-O3 GOL			2.34	2.41
	O1, PER - OE2, E90	3.10	3.32		
	O2, PER - OE2, E241	3.02	3.06		
	O1, PER - S, M237	4.46	4.04		
	O2, PER - S, M86	4.29	4.15		
	Fe1-S, M237	5.60	5.29	4.66	5.17
	Fe2-S, M86	5.58	5.59	6.01	5.77
	S, M237 - S, M86	5.54	5.41	5.87	5.91
Angle, deg.	Fe1-O-O-Fe2 torsion angle	-58.07	-31.59		
	Fe1-O-O angle	133.39	151.30		
	Fe2-O-O angle	94.62	88.66		
	Fe1-OH-Fe2 angle			107.45	113.20
Temperature factor, Å^2	Fe1	14.36	17.62	15.27	15.75
	Fe2	16.41	20.65	17.69	18.65
	O, μ-oxo			18.93	19.15
	O1, PER	21.40	27.98		
	O2, PER	19.83	21.36		
	W1	12.15	30.29		
	W2	13.42	27.08	17.58	19.15
	W3	26.36	33.48		
	O1, GOL			24.71	22.17
	O2, GOL			16.80	19.46
	O3, GOL			20.58	20.31

[1] POX, hsDOHH in complex with peroxo intermediate.

[2] GLC, hsDOHH in complex with glycerol;

[3] PER, peroxide ion;

[4] W1, water coordinated to Fe1;

[5] W3, bridging water;

[6] W2, water coordinated to Fe2;

[7] GOL, glycerol molecule.

The Fe-Fe distances of 3.77/3.68 Å are within the range observed in structures of biomimetic complexes, where the distances vary from 3.17 to 4.00 Å (Kim & Lippard, 1996; Dong *et al*., 1996; Ookubo *et al*., 1996; Zhang *et al*., 2005). The value of ~3.7 Å for the POX structure is slightly longer than the 3.44 Å Fe-Fe distance determined for the peroxo intermediate of hsDOHH by EXAFS (Vu *et al*., 2009). The elongated Fe-Fe distance in the crystal structure is possibly due to ageing during the process of crystallization (at 10^{o}C over 48 h) that might be accompanied by protonation of a bridging hydroxyl ion to water (W3) in the diiron core of POX, which would result in a longer Fe-Fe distance. Ranging between 2.17 and 2.23 Å, the Fe-O(peroxo) distances are longer than the values of 1.86 – 1.94 Å observed in biomimetic model complexes (Kim & Lippard, 1996; Ookubo *et al*., 1996; Zhang *et al*., 2005). The elongated Fe-O(peroxo) distances in the POX structure could result from protonation of the bridging peroxo unit, as proposed for large Fe-O(peroxo) distances in the structure of the non-biological T4moH peroxo intermediate obtained by soaking crystals with H_2O_2 (Bailey & Fox, 2009). Very likely, the POX structure represents the putative secondary peroxo-diiron(III) species, which corresponds to the enzyme aged within the time window of 48 h, as characterized by UV/Vis and Mössbauer spectroscopy (Fig. 3.7 A & C).

In the GLC structure, the Fe---Fe distance has shrunk to 3.44/3.48 Å. There is no electron density consistent with the presence of a μ-1,2-bound peroxo ligand; the $2F_o$-F_c map suggests that a single oxygen atom as a bridging ligand in the lower hemisphere and a glycerol molecule bound to the "upper" hemisphere of the diiron core (Fig. 3.11 F & G; 3.12 C & D). In the refined GLC structure, the distances between Fe and μ-OH are 2.05/1.95 Å (Fe1) and 2.21/2.22 Å (Fe2) (Table 3.2). Fe-O-Fe angles are 107.45° and 113.20° in the two molecules of GLC structure which constitutes a reasonable geometry for a *μ*-hydroxo ligand at a diiron site (Kurtz, 1990). Hydroxyl group 2 (O2) of glycerol replaces W1 of the POX structure and hydroxyl group 3 (O3) replaces

the bridging W3 (Fig. 3.11 H). Hydroxyl group 1 (O1) of glycerol donates a bifurcated hydrogen bond to the carboxylates of E93 and E208.

3.1.7 Density function theory study of hsDOHH

In order to prove the diiron core structures derived from crystal structures, the density function theory (DFT) was applied to calculate all possible geometries for the diiron site of hsDOHH. The models used for the DFT calculations include iron atoms and their solvent ligands, as well as the side-chain of the iron-coordinating residues. They differ by the identity of the bridging ligands between the two iron sites (Fig. 3.13; Table 3.3). These calculations were carried out by Dr. Lars H. Böttger (Institute of Physics, University of Lübeck).

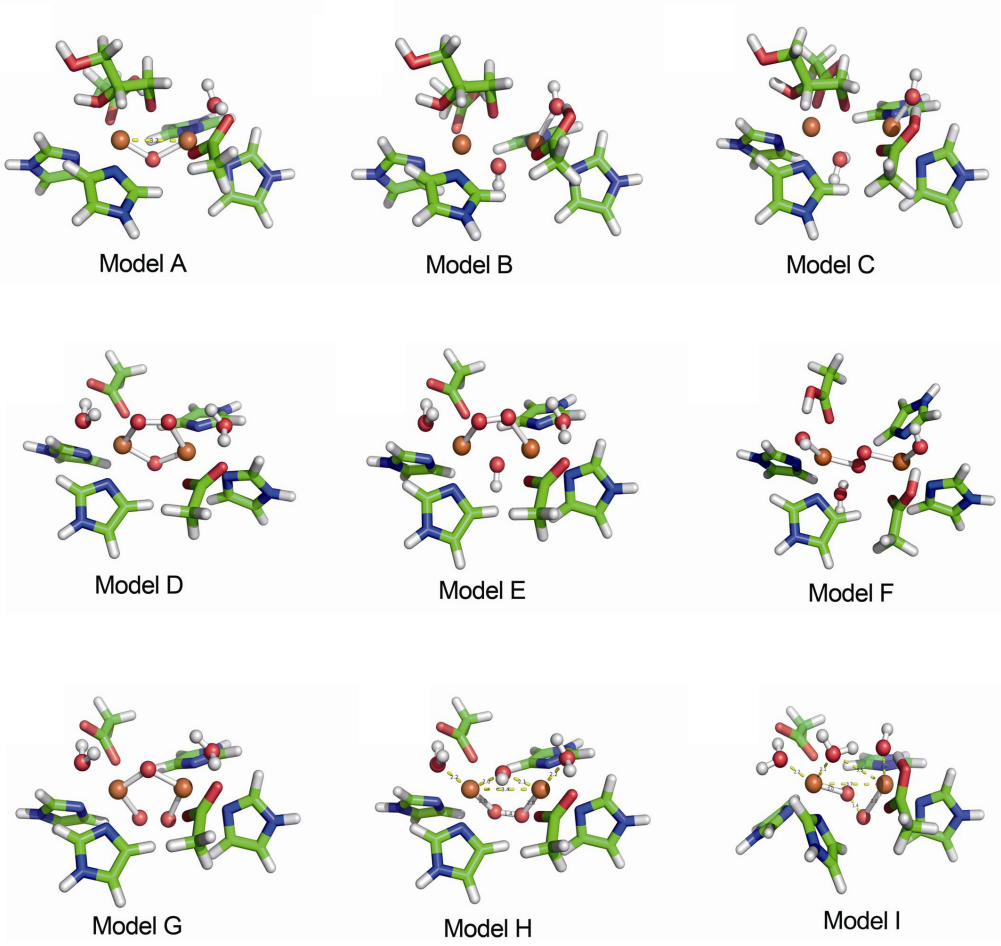

Fig. 3.13 Geometry-optimized models of the hsDOHH diiron core. Carbon, hydrogen, oxygen, nitrogen, and iron are shown in green, grey, red, blue, and brown, respectively.

Motivated by the X-ray structure of GLC, three models A - C (group 1), which represent possible structures of the diiron(III) site of glycerol-bound hsDOHH, were subjected to DFT calculation. The models D - I (groups 2 and 3) represent the diiron core structures with peroxide as bridging ligand. For all these models (A - I), the second bridging ligand is either O, OH, or H_2O. Since the X-ray structure of hsDOHH displays a non-symmetric ligand arrangement (above and below the Fe---Fe axis), the models for the peroxo intermediate with inverted bridges between the two iron sites were investigated (Fig. 3.13; Table 3.3).

Table 3.3 Calculated isomer shifts δ (mm s^{-1}), quadrupole splittings ΔE_Q (mm s^{-1}), magnetic exchange coupling constants J (mm s^{-1}), and Fe-Fe distances R (Å) for the geometry-optimized model structures

Group 1		
(A) Glycerol/O	(B) Glycerol/OH^-	(C) Glycerol/H_2O
$\delta_1 = 0.56$ $\Delta E_{Q,1} = -1.648$	$\delta_1 = 0.53$ $\Delta E_{Q,1} = 0.993$	$\delta_1 = 0.52$ $\Delta E_{Q,1} = 1.458$
$\delta_2 = 0.52$ $\Delta E_{Q,2} = 1.78$	$\delta_2 = 0.47$ $\Delta E_{Q,2} = 1.032$	$\delta_2 = 0.47$ $\Delta E_{Q,2} = 2.125$
$J = -49.59$ R = 3.218	$J = -15.00$ R = 3.514	$J = -4.47$ R = 3.990
Group 2		
(D) O-O/O	(E) O-O/OH^-	(F) O-O/H_2O
$\delta_1 = 0.58$ $\Delta E_{Q,1} = -0.588$	$\delta_1 = 0.61$ $\Delta E_{Q,1} = 1.238$	$\delta_1 = 0.49$ $\Delta E_{Q,1} = -1.325$
$\delta_2 = 0.57$ $\Delta E_{Q,2} = -0.548$	$\delta_2 = 0.62$ $\Delta E_{Q,2} = 1.411$	$\delta_2 = 0.47$ $\Delta E_{Q,2} = 1.415$
$J = -56.89$ R = 3.093	$J = -19.00$ R = 3.365	$J = 546.63$ R = 4.071
Group 3		
(G) O/O-O	(H) OH^-/O-O	(I) H_2O/O-O
$\delta_1 = 0.57$ $\Delta E_{Q,1} = -0.741$	$\delta_1 = 0.58$ $\Delta E_{Q,1} = 0.965$	$\delta_1 = 0.56$ $\Delta E_{Q,1} = -1.25$
$\delta_2 = 0.56$ $\Delta E_{Q,2} = -0.713$	$\delta_2 = 0.59$ $\Delta E_{Q,2} = 1.145$	$\delta_2 = 0.58$ $\Delta E_{Q,2} = -1.03$
$J = -62.11$ R = 3.073	$J = -36.16$ R = 3.425	$J = -14.33$ R = 3.715

Geometry optimization was carried out for all the model structures. The results indicated that the type of single O bridging ligands modulates the Fe-Fe distance of the diiron cluster. The Fe-Fe distance increases in the order O < OH^- < H_2O; for instance, 3.093 Å in model D (O-O/O), 3.073 Å in model G (O/O-O), 3.365 Å in model E (O-O/OH^-), 3.425 Å in model H (OH^-/O-O), 4.071 Å in model F (O-O/H_2O), and 3.715 Å in model I (H_2O/O-O) (Table 3.3). These results are well in agreement with the rules found in studies of biomimetic complexes (Zhang *et al.*, 2005; Fiedler *et al.*, 2008; Frisch *et al.*, 2009).

The Mössbauer parameters (isomer shift δ and quadrupole splitting ΔE_Q) and the exchange coupling constant J obtained from DFT calculations for individual models are summarized in Table 3.3. By comparing calculated and experimental spectroscopic data of hsDOHH, it can be seen that the diiron core structure of the peroxo-diiron(III) intermediate of hsDOHH is best represented by models H and I (Table 3.3; Fig. 3.13). In model H, two iron sites are bridged by *cis*-peroxo (parallel to the Fe-Fe axis) and hydroxyl ligands that are located below and above the four-histidine plane, respectively (Fig. 3.13). The Fe-Fe distance of 3.425 Å in model H is in agreement with the value (3.44 Å) determined by EXAFS (Vu *et al.*, 2009). In particular, the calculated Mössbauer parameters of model H nicely match the experimental results (Fig. 3.7 B). The calculated spectroscopic data of model I also closely fit the experimental results of hsDOHH in the peroxo intermediate except the elongated Fe-Fe distance (3.715 Å). However, the 3.715 Å Fe-Fe distance in model I is in good agreement with the Fe-Fe distances of 3.77 and 3.68 Å in the POX structure (Table 3.2). Therefore, model I likely represents the second peroxo-diiron(III) intermediate of hsDOHH, which is converted from model H through protonation of the bridging hydroxyl group.

The preferred model for the diiron site of the GLC structure is represented by model B, in which the bridging ligands are glycerol and OH^- (Fig. 3.13). The

Fe-Fe distance (3.514 Å) is fit to the value as derived from the X-ray structure (GLC) (3.44 and 3.48 Å).

3.1.8 Secondary coordination sphere of the diiron site in hsDOHH

Surrounding the 4H-2E set of ligands, a number of amino-acid side-chains constitute a secondary coordination sphere for the diiron cluster in hsDOHH. Like the iron ligands of the inner sphere, all residues in the secondary coordination sphere are present in pairs (one mate from each of the two domains) and arranged symmetrically around the diiron center (Fig. 3.14 A). The secondary coordination sphere can be divided into a hydrophilic hemisphere above the Fe---Fe axis and a hydrophobic hemisphere below the Fe---Fe axis (on the "peroxo side" of the diiron core) in Fig. 3.14 A. In the hydrophilic hemisphere, two glutamate pairs (Glu57/Glu244 and Glu93/Glu208) are located at each end of the diiron unit; a hydrogen-bonded tyrosine pair (Tyr60/Tyr211) is around 9 Å (terminal OH group to Fe) above the diiron site. Alanine substitutions of the glutamates 57, 93, and 208 do not affect the iron content (Kang *et al*., 2007), nor does the E244A mutation in this work (Fig. 3.14 B). hsDOHH harboring the mutations Y60A or Y211F retains the iron content (Fig. 3.14 B). The UV/Vis spectrum of Y60A shows remarkable differences from that of wild-type hsDOHH, but that of Y211F does not (Fig. 3.14 C). The tyrosine pair (Tyr60/Tyr211) possibly serves as a sink for highly reactive radicals adventitiously created by Fenton-type chemistry (Kurtz, 2006), although only Tyr60 is conserved whereas Tyr211 is replaced by phenylalanine in DOHH from *Plasmodium* species.

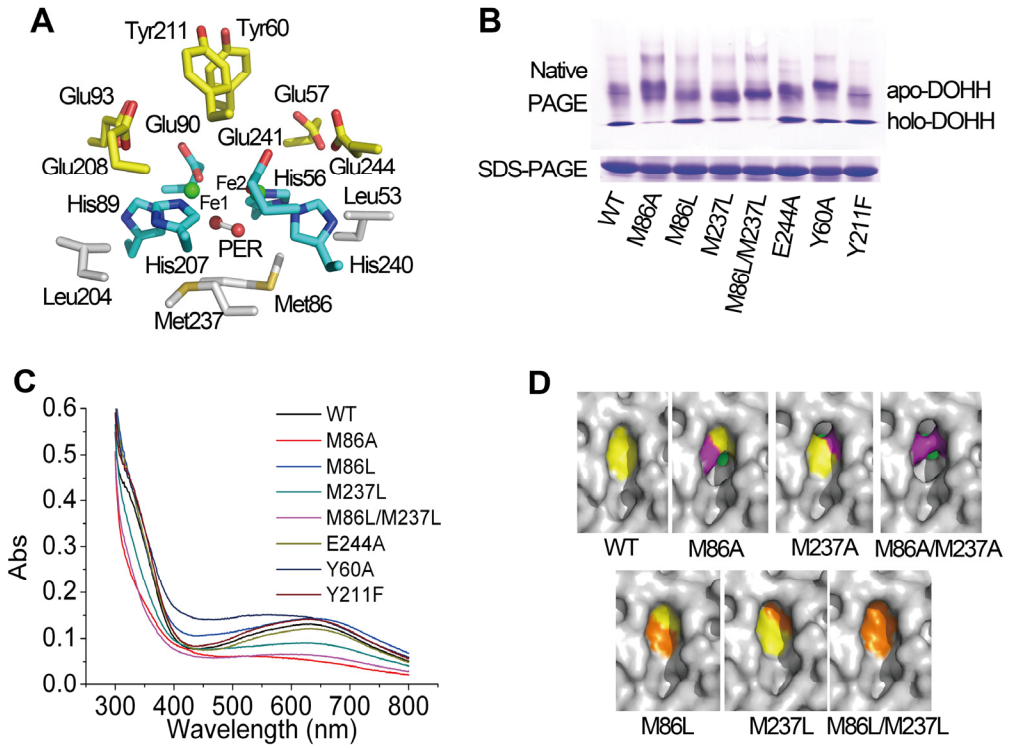

Fig. 3.14 Residues in the secondary coordination sphere of the diiron core of hsDOHH.
(A) The diiron core in hsDOHH, with the secondary coordination sphere included. The carbon atoms of residues in the primary coordination sphere are cyan, those of residues in the hydrophobic secondary hemisphere (below the Fe---Fe axis) are gray and those in the hydrophilic secondary hemisphere (above the Fe---Fe axis) are yellow.
(B) hsDOHH with residues surrounding the diiron core mutated: native electrophoresis and SDS-PAGE.
(C) UV/Vis absorption spectra of wild-type (WT) hsDOHH and mutants.
(D) Modeling of methionine mutations at positions 86 and 237. Iron, methionine, alanine, and leucine are shown in green, yellow, magenta, and orange, respectively.

In the hydrophobic hemisphere, hydrophobic residue pairs Leu53/Leu204 and Met86/Met237 as well as the four iron-coordinating histidines (His56, His89, His207, and His240) enclose the small pocket containing the peroxo ligand below the diiron unit, with Met86 and Met237 shielding the diiron core from solvent (Fig. 3.14 D). The methionine pair is absolutely conserved in DOHH. It displays 180-degree rotational symmetry and is located ~5.5 Å (Fe-S(Met) distance) away from the diiron unit (Fig. 3.14 A). The electron density maps

suggest that there are alternative conformations for the tips of the side-chains of Met86 and Met237.

Although Met237 and Met86 are located in the secondary coordination sphere of the diiron unit and are not coordinating the iron atoms directly, they influence the proper function of hsDOHH. The M237A mutation has been reported to lead to loss of iron and enzymatic activity (Kang *et al.*, 2007). In separate experiments, Met86 was replaced by alanine and one or both of the methionines by leucine. The mutations M86A and M86L/M237L lead to serious loss of iron, whereas M237L leads to partial loss of the metal ions. UV/Vis absorption spectra of the hsDOHH methionine mutants show that the absorption intensity at ~630 nm roughly reflects the iron content of the individual variants (Fig. 3.14 B & C). In addition, we also observe that for some mutants, the profile of the spectrum is different from the wild-type enzyme; for instance, M86L/M237L and M86A show a blue-shifted absorption band and the absorbance at ~ 400 - 500 nm of M86L is enhanced (Fig. 3.14 C). The different spectroscopic profiles imply that the residues in the secondary coordination sphere influence the properties of the peroxo intermediate of hsDOHH. Structural modeling of the methionine mutations shows that the alanine substitutions make the diiron core solvent-accessible, but the leucine mutants do not (Fig. 3.14 D). Yet, the presence of at least one methionine is required to retain hsDOHH in the holoenzyme state. A possible role for the methionine pair might be protection of the diiron core by scavenging reactive oxygen species.

3.1.9 The substrate-binding cavity of hsDOHH

On the surface of hsDOHH, on the "open side" between the two stacks of HEAT repeats, the mouth of a funnel-shaped access cavity to the active site is located. This opening is between 14.5 and 18 Å wide and lined by residues from α2 (Gln22, Arg26, Phe29, Arg32), α12 (Gln215, Gln217), and α16 (Asp278, Met279, His282, Glu283) as well as by Leu145 and Ser146 from the

inter-domain loop (Fig. 3.15 A). About 18 Å into the cavity, a major constriction of the funnel is reached; through the arrangement of amino-acid side-chains from helices α4 (Glu57, Tyr60), α12 (Tyr211), and α14 (Glu241, Glu244), the diameter is narrowed to 6.5 - 9.0 Å (Fig. 3.15 A). This is the entrance to the inner cavity of the enzyme, which is about 11 Å deep and harbors the diiron active site at one of its walls, in an orientation parallel to the long axis of the cavity (Fig. 3.15 B). Residues Glu93 and Glu208 are at the bottom of the inner cavity. These properties are in remarkable agreement with an early prediction based on two inhibitory catechol peptide probes anchored to the metal ions through their dihydroxybenzene groups (Abbruzzese *et al.*, 1991).

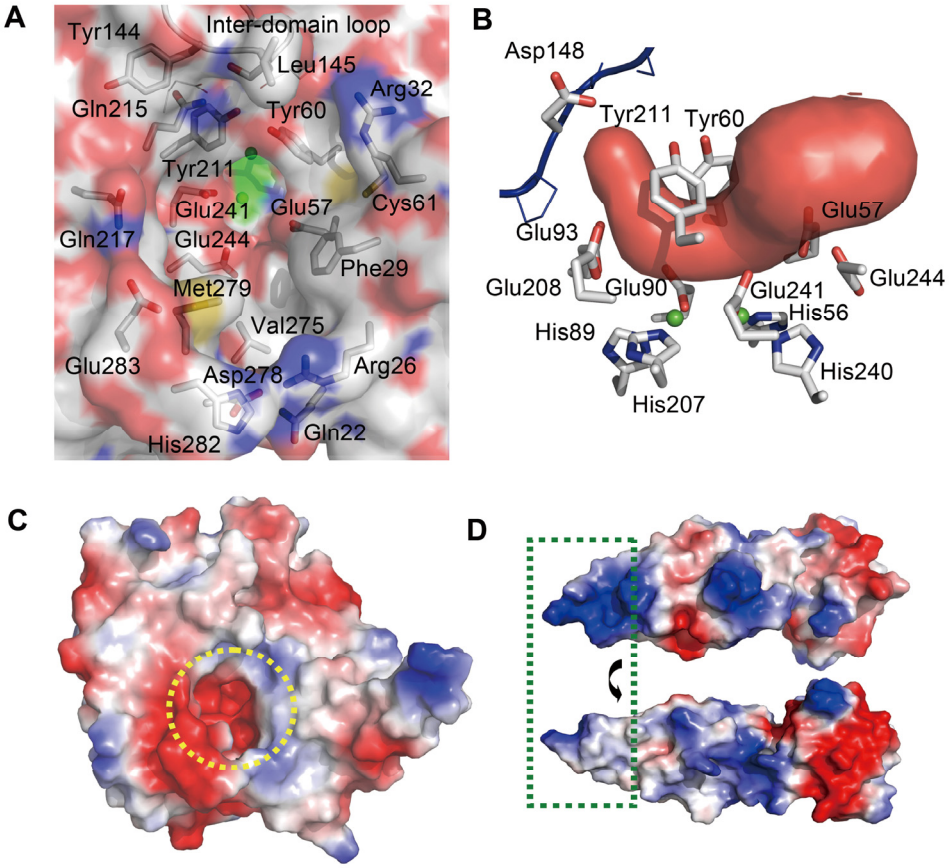

Fig. 3.15 The substrate-binding cavity of hsDOHH.
(A) View into the substrate funnel, onto the constriction at Tyr60, Tyr211, Glu241, Glu244, and Glu57, which forms the mouth of the inner cavity, the binding site for Dhp and Hpu.
(B) The shape of the cavity and its environment.
(C) Surface electrostatics of hsDOHH, colored from red (negative potential) to blue (positive potential). The yellow circle indicates the outer rim of the binding site.
(D) As in (C), for human eIF-5A (PDB code 1FH4; Facchiano *et al.*, 2001). The interacting region of eIF-5A is indicated by the green rectangle. Two orientations of the eIF-5A molecule are shown.

The dimension of the external cavity is sufficiently wide to accommodate the exposed loop of eIF-5A that carries the Dhp residue to be hydroxylated by hsDOHH. The inner cavity is perfectly suited to harbor the side-chain of the substrate, Dhp, and the product, Hpu. The electrostatic potential of the substrate-binding site is negative in both the inner and the external cavities (Fig. 3.15 C), in agreement with the long, basic side-chain of Dhp and the very basic, exposed hydrophilic loop (KTGK$_{50}$HGHAK) of the substrate, Dhp-eIF-5A

(Fig. 3.15 D).

3.1.10 A model for Dhp - eIF-5A binding to hsDOHH

In order to build a binding model of Dhp/Hpu in the active center of hsDOHH, an automated docking experiment was carried out as part of this study. Dhp and Hpu were docked to hsDOHH by using AutoDock (Morris *et al.*, 2009). The results show that the side-chain of the Dhp/Hpu residue is neatly accommodated by the inner cavity of hsDOHH (Fig. 3.16 A & B). In the modelled Dhp complex, the terminal ammonium group of the amino acid forms strong hydrogen bonds with the Oε2 atoms of Glu93 and Glu208 and its Nε atom hydrogen-bonds with Glu241 Oε2 (Fig. 3.16 A). Compared to the hsDOHH – Dhp complex, the structure of the hsDOHH – Hpu complex shows some interesting differences. The Hpu side-chain moves slightly out from the inner cavity (Fig. 3.16 B). The terminal ammonium group of Hpu switches to Glu93 Oε2 and the hydroxyl group of Hpu forms a hydrogen bond with Glu90 Oε2 (Fig. 3.16 B)). The carbon atom to be hydroxylated moves from near Fe1 in the hsDOHH – Dhp complex to a position in the middle between the two iron atoms, above the diiron site (Fig. 3.16 A & B). Such a different binding mode between Dhp – eIF-5A/Hpu – eIF-5A and hsDOHH is consistent with the results from GST-pulldown experiments that hsDOHH displays stronger interaction with the Dhp – eIF-5A than the Hpu – eIF-5A (Kang *et al.*, 2007)

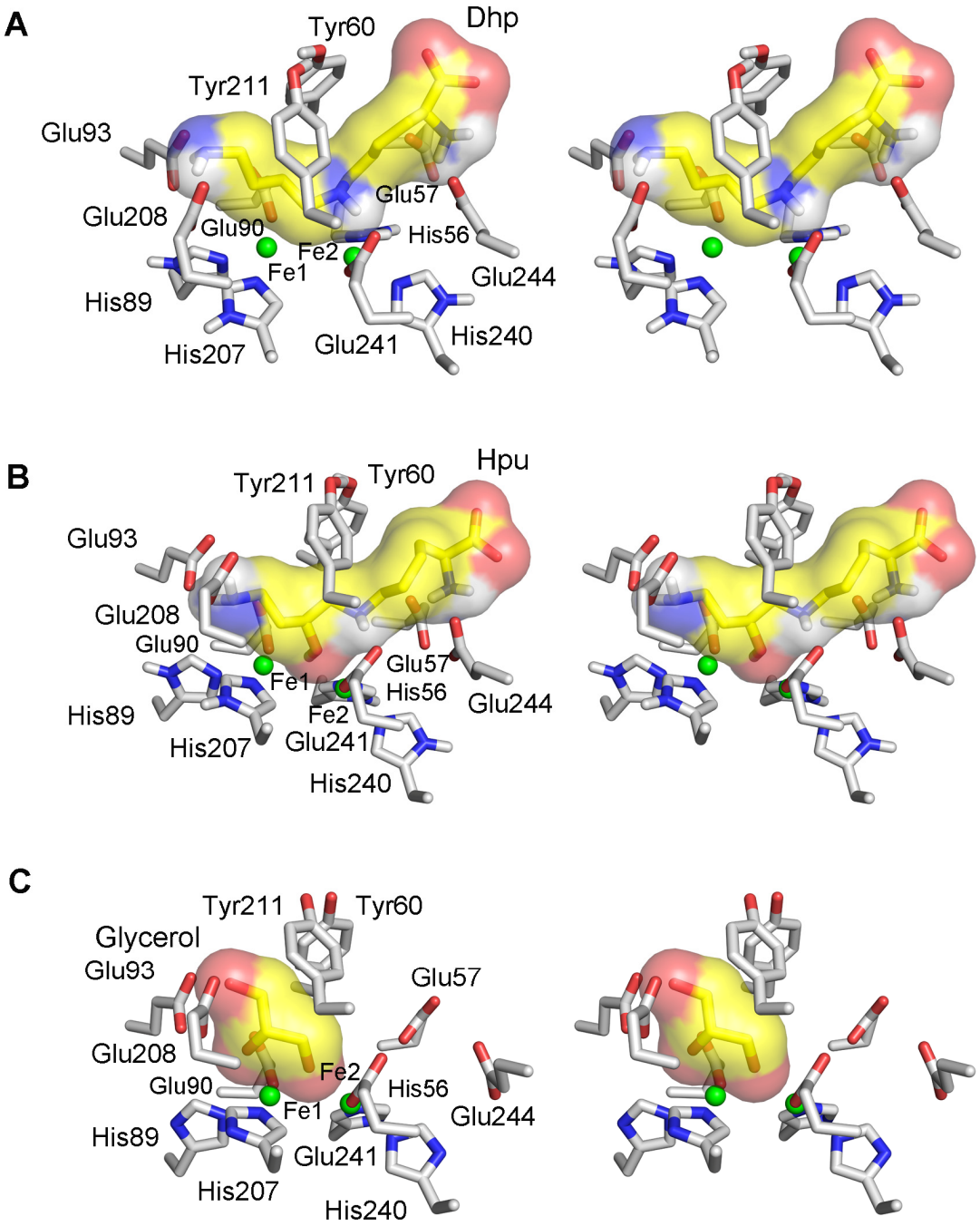

Fig. 3.16 A model of the hsDOHH – Dhp/Hpu interaction. Carbon, nitrogen, oxygen, and iron atoms are presented in gray, blue, red, and green, respectively. The carbons of ligands are presented in yellow. A surface presentation of liagnds is shown.
(A) Docking structure of the hsDOHH – Dhp complex.
(B) As in (A), for hsDOHH – Hpu.
(C) Glycerol in the substrate cavity in the GLC structure.

These docking results are also in good agreement with the previous observation of an essential role of Glu90, Glu208, and Glu241 for substrate binding (Kang *et al.*, 2007). In contrast, Glu93 was found not to be important for binding of the substrate Dhp-eIF-5A but essential for enzymatic activity (Kang *et al.*, 2007); our automated docking results suggest that this residue may be crucial to stabilize the product complex, hsDOHH - Hpu. Kang *et al*. (2007) also observed that Glu57, Gly63, and Gly214 are critical for substrate-binding. Located at the entrance of the inner cavity, Glu57 (as well as Glu244 in the position related by quasi-symmetry) likely interacts with the main-chain amide group of Dhp. An alanine substitution of Gly63 (α4) probably results in steric conflict with the side-chain of Ala94 (α6). Gly214 is located at the bottom of a side-pocket in the wall of the external cavity, which is possibly occupied by the imidazole group of a histidine residue (likely His51) on the exposed loop of Dhp-eIF-5A upon substrate-binding. The plasticity of the C-terminal α-helices, in particular α16 (observed through the comparison of our POX and GLC structures) probably facilitates the accommodation of Dhp-eIF-5A by the enzyme.

Although a large polypeptide (residues 20 - 90) around the Dhp residue in eIF-5A is needed for an effective enzyme-substrate interaction (Kang *et al.*, 2007), the docking results with Dhp and Hpu alone still provide many hints for understanding the molecular interactions between hsDOHH and its only substrate, Dhp-eIF-5A, and they are in agreement with the substrate-binding information obtained from the mutagenesis experiments and crystal structures. In addition, the binding mode of glycerol in the GLC structure superimposes perfectly with the terminus of Hpu (terminal three carbons) in the docked structure (Fig. 3.16 A, B & C); thus, glycerol can be considered a model for the product of the DOHH reaction.

3.2 Yeast deoxyhypusine hydroxylase

Multiple protein sequence alignment revealed that DOHH is highly conserved among animals (identity >80% and similarity >90%) (Fig. 3.17). However, DOHH from animals and lower organisms show significant sequence diversity (Fig. 3.17). For instance, the amino-acid sequences of DOHH from *Saccharomyces cerevisiae*, *Leishmania donovani*, *Plasmodium vivax* and *Plasmodium falciparum* are 42% (57%), 37% (52%), 27% (44%), and 21% (37%) identical (similar) to hsDOHH, respectively. Therefore, yeast DOHH (scDOHH) and *Plasmodium* DOHH were also selected for structural studies in order to compare them with hsDOHH.

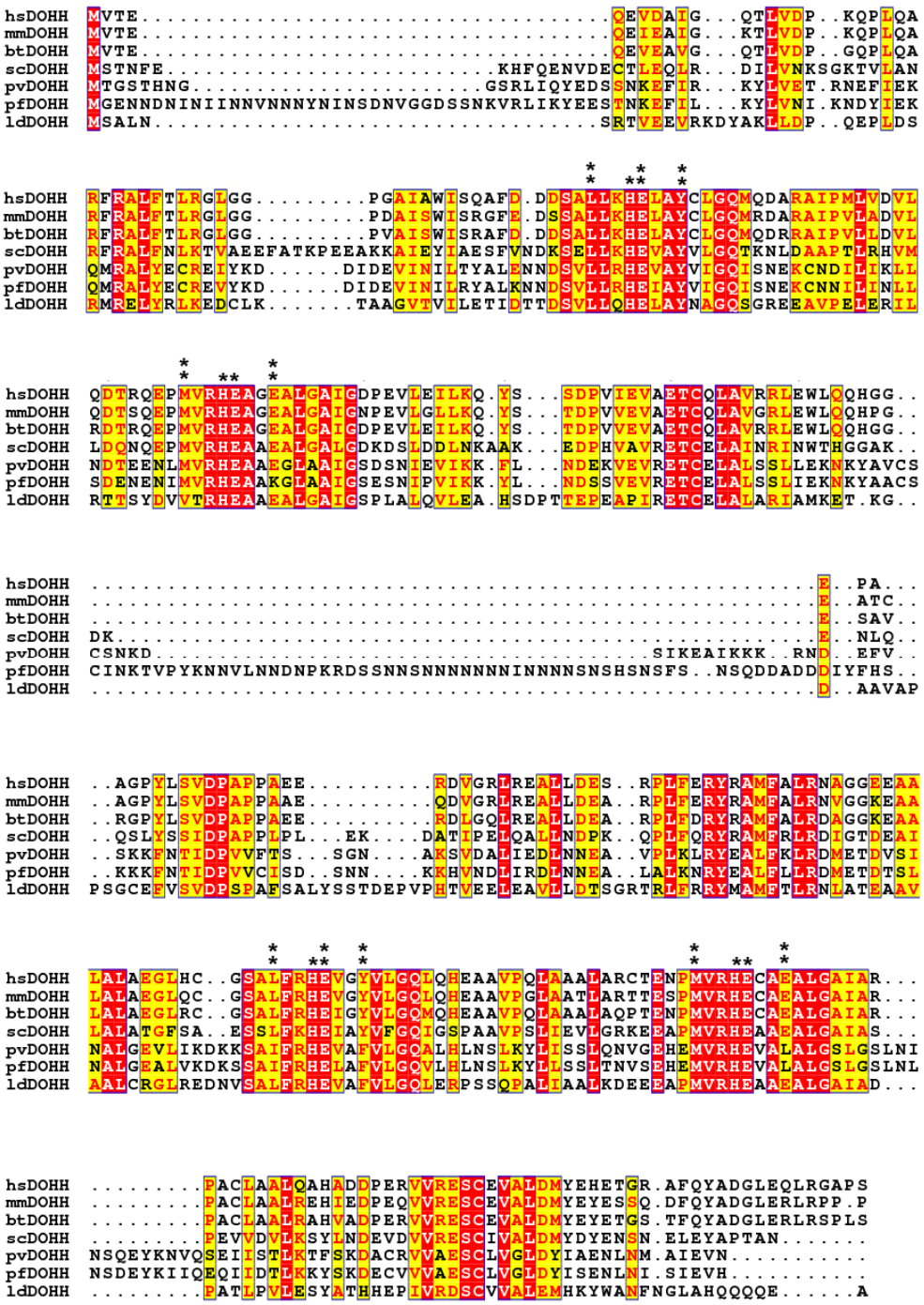

Fig. 3.17 Amino-acid sequence alignment of DOHH.
Amino-acid sequences are from the National Center for Biotechnology Information (NCBI) database: hs (*Homo sapiens*), NP_001138637.1; mm (*Mus musculus*), NP_598725.2; bt (*Bos Taurus*), NP_001069354.1; sc (*Saccharomyces cerevisiae*), P47120.1; pv (*Plasmodium vivax*), CAP62402.1; pf (*Plasmodium falciparum*), CAJ57350.3; ld (*Leishmania donovani*), ADJ39999.1. The iron-coordinating residues and the residues in the secondary coordination sphere are labeled by one and two asterisks, respectively.

3.2.1 Protein production and purification

GST-fusion scDOHH was overexpressed in *Escherichia coli*. After cleaving of the GST tag, holo-scDOHH was successfully isolated from total recombinant protein (a mixture of holo-scDOHH and apo-scDOHH) by repeated gel filtration (Fig. 3.18 A). The purification process of repeated gel filtrations was monitored by SDS-PAGE and native PAGE, in order to make sure that chromatographic fractions containing holo-scDOHH were collected (Fig. 3.18 B & C). It can be seen that highly pure holo-scDOHH was obtained for crystallization. As shown in Fig. 3.18 D, isolated scDOHH also is bluish (Fig. 3.18 D).

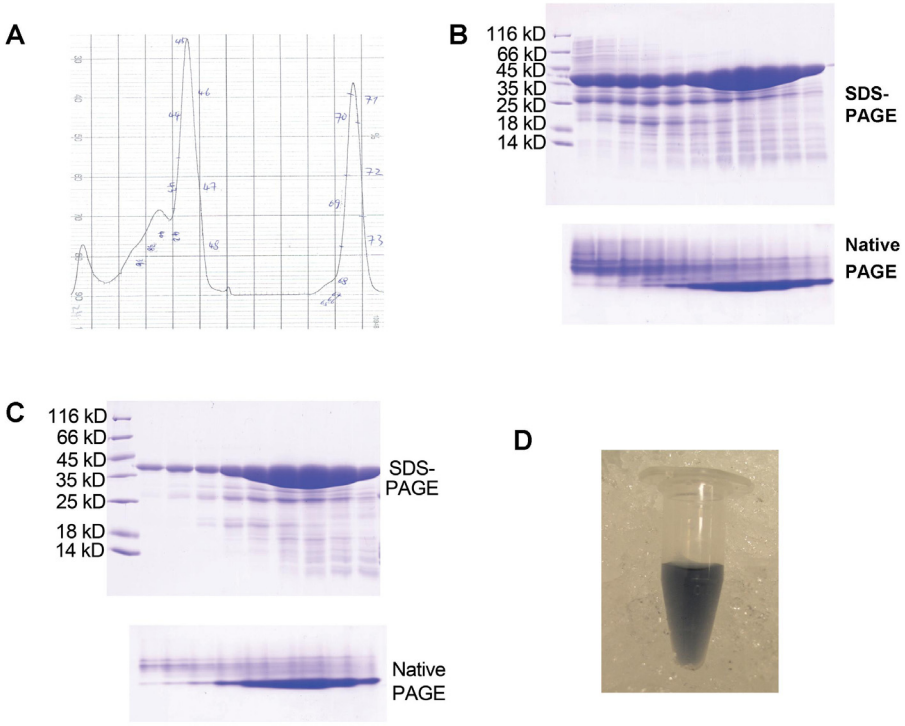

Fig. 3.18 Purification of scDOHH.
(A) Size-exclusion chromatography of scDOHH. Left: first round of gel filtration; right: fractions containing holo-scDOHH from first-round gel filtration were pooled and loaded onto a Superdex^{TM} 75 column for second-round purification.
(B) SDS-PAGE (upper PAGE gel) and native PAGE (lower PAGE gel) analysis of the first-round chromatographic fractions.
(C) SDS-PAGE (upper PAGE gel) and native PAGE (lower PAGE gel) analysis of the second-round chromatographic fractions.
(D) Purified scDOHH.

3.2.2 UV/Vis spectroscopy

Isolated recombinant scDOHH is bluish. This is the characteristic color of non-heme diiron enzymes featuring a *μ*-1,2-peroxo-diiron(III) core. The blue color of scDOHH is stable during the entire protein purification process at 4°C. Fig. 3.19 shows time-dependent UV/Vis spectra of scDOHH at room temperature. The fresh purified scDOHH (0 h in Fig. 3.19) displays a similar absorption profile as seen for hsDOHH. The intensity of the absorption band of λ_{max}~ 640 nm slowly decreases with time (recorded time, 0 - 96 h); the estimated half-life of the peroxo-diiron(III) intermediate of scDOHH is about 29 h at room temperature (Fig. 3.19). It is obvious that the decay rate of the peroxo intermediate accelerates with time. In addition, the intensity loss is coupled with a slight blue-shift of the maximum absorption (from λ_{max} ~640 nm to λ_{max} ~626 nm). Three near-isosbestic points, ~317 nm, ~360 nm, and ~421 nm, are found in the time-dependent UV/Vis spectra of scDOHH (Fig. 3.19), implying that the initial peroxo-diiron(III) core in scDOHH converted to another species, which could be either another peroxo intermediate or the resting state of the enzyme (diiron(III) core). The UV/Vis spectra of hsDOHH and scDOHH are similar but different in detail. For hsDOHH, the absorption at long wavelengths displays dramatic blue-shift and the intensity does not decrease to the half of its initial value (half-time is not available) (Fig. 3.7 A).

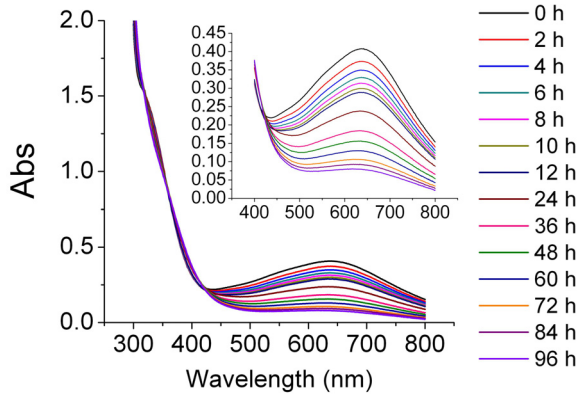

Fig. 3.19 Time-dependent UV/Vis spectra of scDOHH. The spectra were recorded at room temperature. The inset shows a magnification of the absorption peak at long wavelengths.

3.2.3 scDOHH crystallization, crystal optimization, and structure determination

scDOHH was first crystallized in a condition containing 100 mM Tris-HCl (pH 7.5), 200 mM $MgCl_2$, and 25% PEG 4000 (Fig. 3.20 A). However, the crystals were useless needles. Crystals of cubic form were obtained by adding 400 - 600 mM guanidinium chloride as crystallization additive (Fig. 3.20 B). The crystals remained blue up to one week after setting up the crystallization experiment (at 10°C) (Fig. 3.20 B) and diffracted up to 2.10 Å at beamline P11 of PETRA III, DESY, Hamburg. During diffraction-data collection (360°), the color of the crystal changed from blue to light yellow, suggesting photoreduction. The first-120° and last-120° diffraction data were processed separately for structure determination. Structures were solved by using molecular replacement with hsDOHH (POX) as the search model. There was no significant difference found between the structures determined from the first-120° and last-120° images. The diffraction data and refinement statistics for the structure solved from the first-120° images are summarized in Table 3.4.

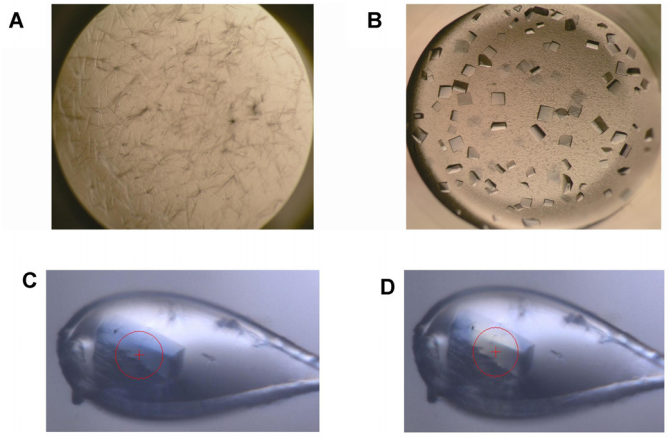

Fig. 3.20 Crystals of scDOHH.
(A) Initial crystallization hit of scDOHH.
(B) Optimized crystals. Image was taken one week after setting up the crystallization experiment.
(C) Crystal from (B) before diffraction-data collection.
(D) Same crystal as in (C) after 360° diffraction-data collection.

Table 3.4 Crystallographic data and refinement statistics of scDOHH

Diffraction data statistics	
X-ray source	P11, PETRAIII
Wavelength. Å	1.0000
Space group	$P4_122$
Unit cell parameters, Å, deg.	a = b = 74.43, c = 232.76
Resolution range, Å	47.96 - 2.10
Reflections	322,660 (41,037)
Unique reflections	39,382 (5,612)
R_{merge} [1]	0.119 (0.823)
R_{pim} [2]	0.044 (0.321)
$CC_{1/2}$ [3]	0.996 (0.687)
$I/\sigma(I)$	11.4 (2.5)
Redundancy	8.2 (7.3)
Completeness, %	100.0 (100.0)
Wilson B factor, Å^2	28.5
Refinement statistics	
Refinement resolution, Å	16.98 - 2.10
No. reflections	37,237
R_{work}/R_{free} (% of refls.) [4]	0.220/0.262 (5.0)
Average B factor, Å^2	40.40
No. of atoms	
Protein	4557
Water	208
Other	20
r.m.s. deviation	
Bond lengths, Å	0.015
Bond angles, deg.	1.652
Ramachandran favored, %	97.1
Ramachandran outlier, %	0.2
Clashscore	7.86
MolProbity score [5]	2.18

[1] $R_{merge} = \Sigma_{hkl}\Sigma_i|I_i(hkl) - \langle I_i(hkl)\rangle| / \Sigma_{hkl}\Sigma_i\, {}^{I_i(hkl)}$

[2] Precision-indicating merging R factor. R_{pim} is defined as $\Sigma_{hkl}[1/(N-1)]^{1/2}\,\Sigma_i|I_i(hkl) - \langle I(hkl)\rangle| / \Sigma_{hkl}\Sigma_i\, {}^{I_i(hkl)}$, N is redundancy (Weiss & Hilgenfeld, 1997).

[3] Correlation coefficient between two random-half data sets (Karplus & Diederichs, 2012).

[4] $R_{work} = \sum_{hkl}|F_{obs} - F_{calc}| / \sum_{hkl}F_{obs}$. R_{free} serves as cross-validation of the R-factor. 5% of the reflections were set aside for the calculation of the free R-factor (Brünger, 1992).

[5] log-weighted combination of the clashscore, percentage of non-favored Ramachandran angles, and percentage of bad side-chain rotamers (Chen *et al.*, 2010).

3.2.4 Overall structure of scDOHH

There are two copies of scDOHH in the asymmetric unit. The overall structure of scDOHH is similar to that of hsDOHH. The structures of scDOHH and hsDOHH can be superimposed with an r.m.s. difference of about 1.00 Å (GLC) and 0.92 Å (POX) (on Cα positions). Like hsDOHH, scDOHH consists of four N-terminal HEAT repeats (α1 - α8) (N-terminal domain) and four C-terminal HEAT repeats (α9 - α16) (C-terminal domain), which are linked by a long inter-domain loop (Gly158 - Ile188, 31 residues) (Fig. 3.21 A). All the α-helixes in each domain are regularly arranged as observed in hsDOHH (Fig. 3.21 A). The inter-domain loop in scDOHH is longer than the corresponding loop in hsDOHH (His135 - Val158, 24 residues) (Fig. 3.21 B). A short α-helix (α_{loop}) situated in the loop is positioned adjacent to α8 of the N-terminal domain. The inter-domain loop plays a major role in maintaining the architecture of holo-scDOHH. A large number of residues (Lys161, Glu164, Ser169, Ser173, Asp175, Thr187) of the loop are hydrogen-bonded or salt-bridged with residues from the terminal domains, in contrast to the weak interaction between the N-terminal and C-terminal domains. The conformation of the inter-domain loop is conserved between scDOHH and hsDOHH, in particular in the middle region of the loop (Fig. 3.21 B). Enclosed by the N-terminal domain, C-terminal domain, and inter-domain loop, the diiron site of scDOHH is located at the center of the protein (Fig. 3.21 A).

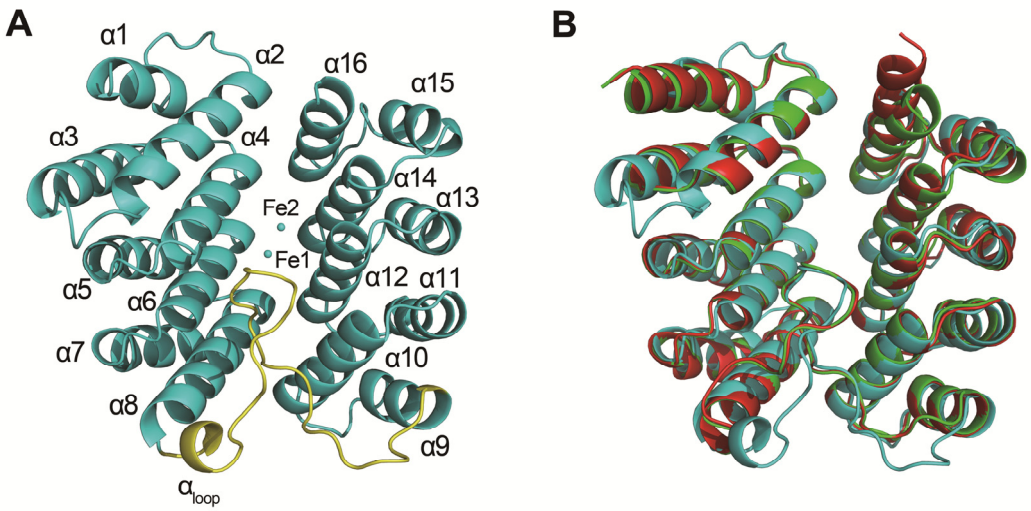

Fig. 3.21 Structure of scDOHH.
(A) Cartoon presentation of scDOHH. α-helices are labeled. Iron atoms and the inter-domain loop are presented in cyan and yellow, respectively.
(B) Superimposition of scDOHH (cyan), hsDOHH POX (red), and hsDOHH GLC (green).

3.2.5 Diiron site of scDOHH

Amino-acid residues as iron ligands in scDOHH include His79 (α4), His112 (α6), Glu113 (α6), His237 (α12), His270 (α14), and Glu271 (α14) (Fig. 3.22 A). As in hsDOHH, scDOHH also features a histidine-rich coordination (4H-2E); all histidines coordinate iron through their Nε atoms and are located in the same hemisphere of the diiron site (Fig. 3.22 B); both the glutamate residues terminally coordinate to irons in a monodentate fashion (Fig. 3.22 B). Alanine substitution of these residues gave rise to loss of the iron cofactor (Cano *et al.*, 2010).

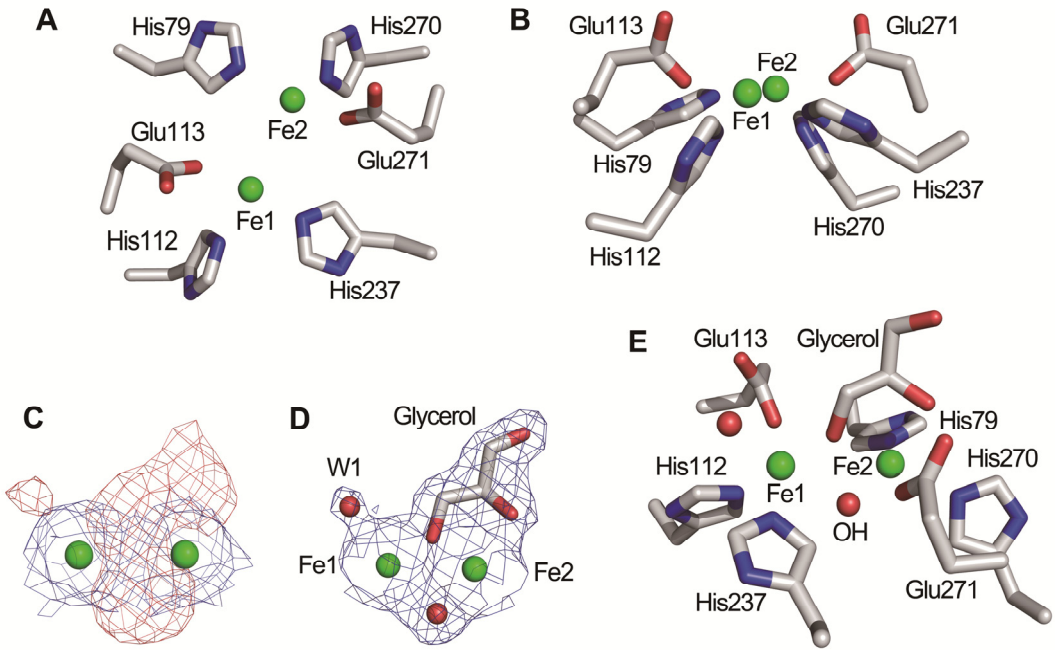

Fig. 3.22 Diiron site of scDOHH (molecule A).
(A) Amino-acid residues coordinating to iron sites.
(B) As in (A), viewed from another angle (viewed from the side of His112 and His237).
(C) Electron density around the diiron site (molecule A) before modeling of solvent ligands. Blue: $2F_o$-F_c density, 1σ; red: positive F_o-F_c density, 3σ.
(D) Electron density around the diiron site (molecule A) after modeling of solvent ligands. Blue: $2F_o$-F_c density, 1σ.
(E) Diiron site of scDOHH. Iron, oxygen, nitrogen, and carbon are shown in green, red, blue, and gray, respectively.

In addition to the ligands derived from amino-acid residues, the F_o-F_c map around the diiron site of scDOHH suggests that several solvent molecules coordinate to the iron atoms as well. As shown in Fig. 3.22 C & 3.23 A, below the Fe---Fe axis, the positive F_o-F_c density could be assigned as a hydroxyl ion or peroxide ion. Both the two possible ligands were assigned to the density during refinement. The $2F_o$-F_c maps after modeling of hydroxyl ion or peroxide ion suggested that hydroxyl ion is more reasonable (Fig. 3.22 D) (the map of peroxide ion is not shown). In the refined structure, Fe1-O (hydroxyl) distances are 2.54 and 2.60 Å (for molecules A and B, respectively) and Fe2-O (hydroxyl) distances are 2.16 and 1.97 Å (for molecule A and B, respectively). Above the Fe---Fe axis, a piece of weak positive F_o-F_c density near the Fe1 site can be

assigned as terminal water molecule coordinating to Fe1; a large piece of density can be assigned as a glycerol molecule considering that about of glycerol was used as cryoprotectant (Fig. 3.22 C & D; 3.23 A & B). Glycerol O3 bridges the two iron sites; whereas the O2 terminally coordinates to Fe2; O1 group hydrogen-bonds with Glu274 Oε1 (Fig. 3.22 D & E; 3.23 A & B). It can be seen that the glycerol binds to the diiron site in a similar mode as seen in the hsDOHH GLC structure, but the position of glycerol has changed from Fe1 site in the GLC structure to Fe2 site in scDOHH. This is not surprising, as the geometry of the diiron sites in DOHH (both the primary and secondary coordination sphere) is largely symmetric. Another possible explanation for this change is that in hsDOHH, the amino terminus of α1 from another asymmetric unit occupies the space above the Fe2 site, thereby preventing glycerol from binding to the Fe2 site in hsDOHH. This situation caused by crystal packing in hsDOHH does not occur in scDOHH crystals.

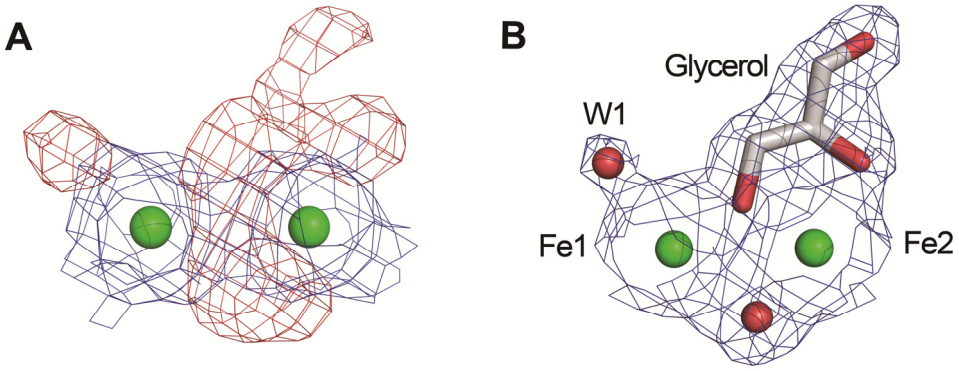

Fig. 3.23 Electron density map around the diiron site in molecule B of scDOHH.
(A) Electron density around the diiron site before modeling of solvent ligands. Blue: $2F_o$-F_c density, 1σ; red: F_o-F_c density, 3σ.
(B) Electron density around the diiron site after modeling of solvent ligands. Blue: $2F_o$-F_c density, 1σ.

Fe-Fe distances in scDOHH are 3.34 and 3.44 Å (for molecule A and B, respectively), which are similar to the value found in the glycerol-bound diiron core of hsDOHH (GLC structure).

3.2.6 Secondary coordination sphere of scDOHH

The composition and geometry of the secondary coordination sphere in the diiron core of scDOHH are similar to what is seen in hsDOHH. Above the Fe---Fe axis, the symmetrically arranged glutamate pairs Glu116/Glu238 and Glu80/Glu274 are located 4.6 – 6.1 Å (carboxylate Oε to Fe) away from the Fe1 and Fe2 sites, respectively; the tyrosine pair Tyr83/Tyr241 is ~9 Å (from the tyrosine OH groups to the irons) above the diiron site (Fig. 3.24). Below the Fe---Fe axis, the methionine pair Met109/Met267 and the leucine pair Leu234/Leu76 as well as four iron-coordinating histidines form a hydrophobic pocket with the methionine pair separating the diiron site from solvent (Fig. 3.24).

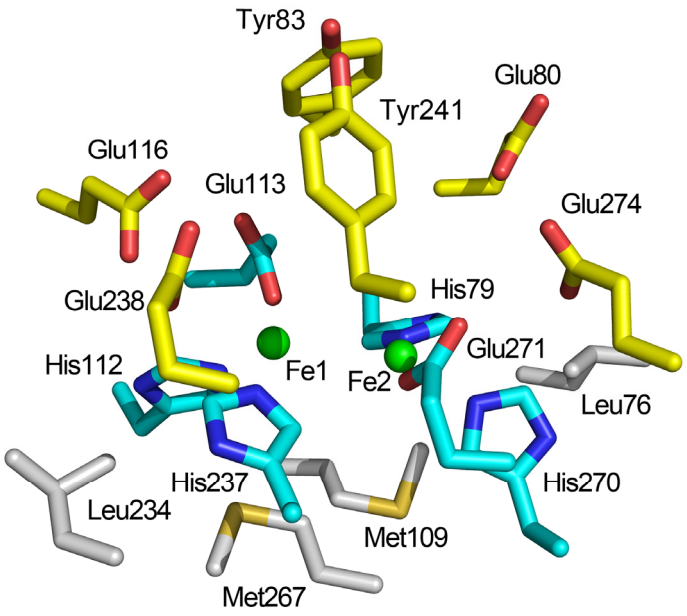

Fig. 3.24 The secondary coordination sphere of scDOHH. Oxygen, nitrogen, sulfur, and iron are shown in red, blue, yellow, and green, respectively. Carbon atoms in the primary coordination sphere are shown in cyan. Carbon atoms in the secondary coordination sphere above and below the Fe---Fe axis are shown in yellow and grey, respectively.

3.2.7 Substrate-binding pocket of scDOHH and scDOHH – Dhp-eIF5A interaction

There is only one direct path connecting the interior and the surface of scDOHH which should be the substrate-binding cavity of the enzyme. The

whole cavity can be divided into two parts, an external cavity and an inner cavity, according to their size and location. Constructed by N-terminal helices (α2, α4), C-terminal helices (α12, α14, α16), and the middle region of the inter-domain loop, the external cavity is big and located close to the surface of the protein (Fig. 3.25 A & B). At the bottom of the external cavity, the tyrosine pair Tyr83/Tyr241 and the glutamate pair Glu80/Glu274 constitute the entrance to the inner cavity which has a diameter of about 7 Å (6.86 Å from Tyr83 Cε2 to Glu274 Oε1; 7.51 Å from Tyr241 Cε1 to Glu80 Oε2) (Fig. 3.25 B). The inner cavity passes along the diiron site, and ends at the glutamate pair Glu116/Glu238 (Fig. 3.25 C). The depth of the inner cavity is around 10 Å (measured between Glu116 Oε2 and Glu80 Oε2 or between Glu238 Oε2 and Glu274 Oε1). According to the dimensions of the cavities, it can be predicted that the external and inner cavities are the binding sites for the highly positively charged exposed loop (SKTGK$_{51}$HGHAK) and the Dhp residue of yeast Dhp-eIF-5A, respectively. Similar to hsDOHH, the entire substrate-binding cavity of scDOHH is largely negatively charged (Fig. 3.25 D) consistent with the electric potential of the predicted scDOHH-binding area in yeast Dhp-eIF-5A.

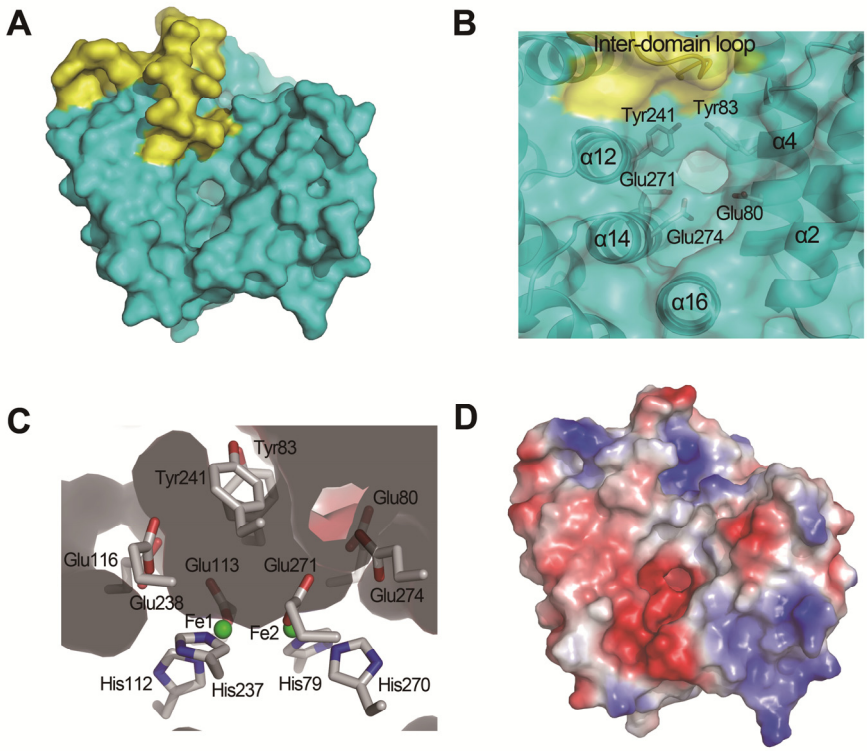

Fig. 3.25 Substrate-binding cavity of scDOHH.
(A) Cavity on the surface of scDOHH. The inter-domain loop is shown in yellow.
(B) A detailed presentation of the external cavity in scDOHH.
(C) Inner cavity and surrounding residues.
(D) Electric potential distribution of scDOHH. Red: negatively charged; blue: positively charged.

It can be seen that amino-acid residues constructing the inner cavity are mainly from the secondary coordination sphere of the diiron core above the Fe---Fe axis. Site-directed mutagenesis by Cano *et al*. (2010) revealed that alanine substitution of Glu113, Glu116, Glu238, His270, Glu271, and Glu274 impaired the substrate-binding ability of the enzyme. Aspartic acid substitution of Glu116 and Glu274 partially restored the scDOHH – Dhp-eIF-5A interaction indicating that these two glutamates of scDOHH make salt-bridge with yeast Dhp-eIF-5A. In hsDOHH, Glu57 and Glu208 were found to play a similar role as Glu116 and Glu274 in scDOHH (Kang *et al*., 2007). According to the crystal structures of scDOHH and hsDOHH, the corresponding residues for Glu80, Glu116, Glu238, and Glu274 in scDOHH are Glu57, Glu93, Glu208, and

Glu244 in hsDOHH, respectively. Therefore, on the basis of these mutagenesis studies and crystal structures, it can be concluded that all of these glutamates in the secondary coordination sphere of DOHH make salt-bridge with positively charged amino-acid residues in Dhp-eIF-5A, in particular the Dhp residue. Itself role of Glu93 in the hsDOHH – Dhp-eIF-5A interaction needs to be further investigated, since it was found to be critical for enzymatic activity of hsDOHH but not important for substrate-binding (Kang *et al*., 2007).

3.3 Structure of *Plasmodium* deoxyhypusine hydroxylase

It has been argued that *Plasmodium* DOHH is a novel potential anti-malaria target (von Koschitzky & Kaiser, 2013). This part of my work aimed at determining the atomic structure of *Plasmodium* DOHH, thereby providing a basis for the design of inhibitors.

3.3.1 Recombinant *Plasmodium falciparum* DOHH production and crystallization

His-tagged *Plasmodium falciparum* DOHH (pfDOHH) was not soluble (data not shown). In contrast, GST-fusion pfDOHH was soluble. The recombinant pfDOHH displayed blue color during the step of GST-affinity chromatography. However, the blue color vanished within 2 h at 4^{o}C. Recombinant pfDOHH (after cleaving of the N-terminal GST tag) eluted as two close peaks in size-exclusion chromatography (Fig. 3.26 A, left). SDS-PAGE analysis of chromatographic fractions revealed that only the second peak contained relatively pure recombinant protein (theoretical molecular mass: 46.9 kDa) (Fig. 3.26 B, top). Native PAGE analysis indicated that the holo-pfDOHH was present in the second peak (Fig. 3.26 B, bottom). Highly pure recombinant pfDOHH was obtained by subjecting the protein from the second peak to a gel filtration column for a second round of purification (Fig. 3.26 A, right). Fig. 3.26 C shows the SDS-PAGE and native PAGE results of the chromatographic fractions from the second round of gel filtration. The behavior of pfDOHH in non-denaturing electrophoresis is distinct from that of DOHH from man and yeast. The band corresponding to holo-pfDOHH is not compact (Fig. 3.26 B & C), suggesting that the overall structure of holo-pfDOHH is different from that of the human and yeast enzymes. Atomic absorption spectra revealed that only 30 – 35% of isolated recombinant pfDOHH was in the holo-state. *In-vitro* reconstitution of the apo-pfDOHH with iron (Fe^{2+}) did not yield holo-pfDOHH (data not shown). The DLS result indicated that the purified pfDOHH was homogeneous (Fig. 3.26 D). However, no crystallization hit was obtained from

this preparation.

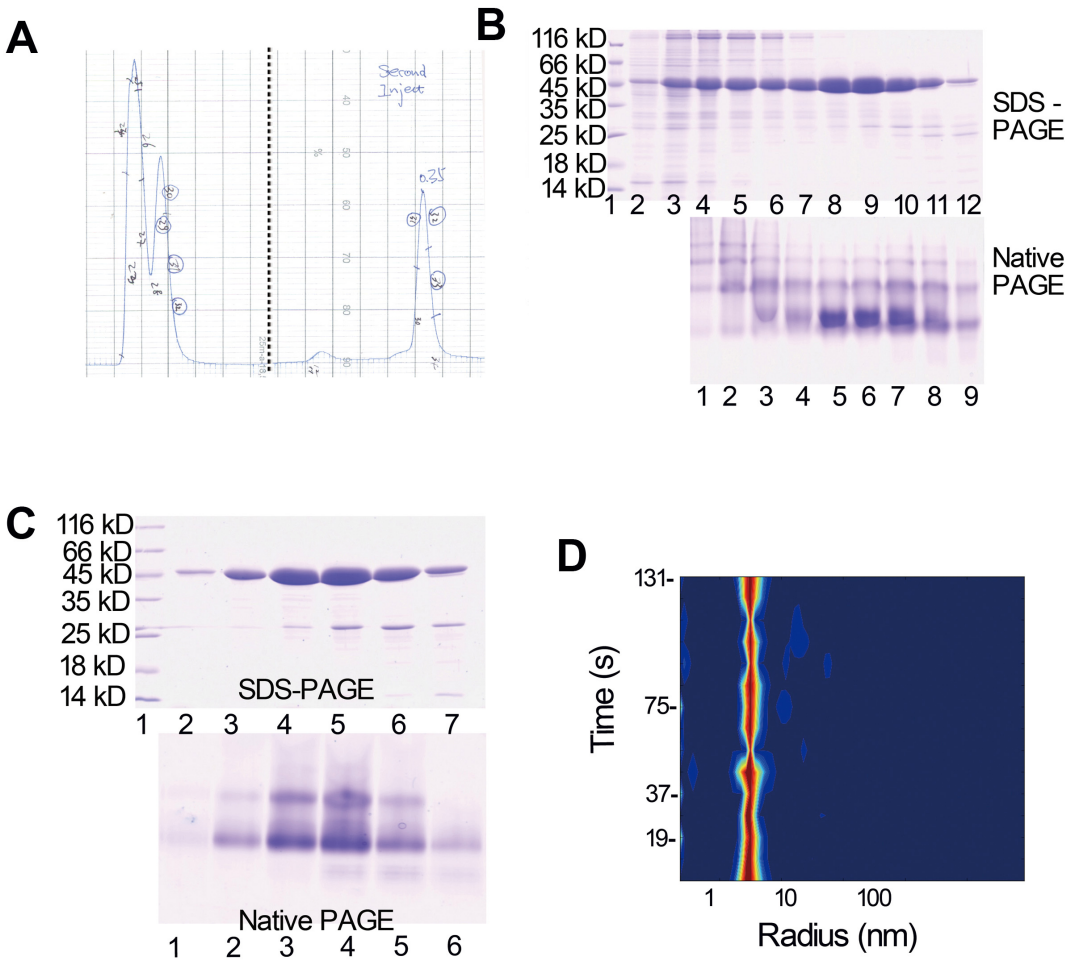

Fig. 3.26 Purification of pfDOHH.
(A) Size-exclusion chromatography of pfDOHH (46.9 kDa). Left chromatogram: first round of gel filtration; right chromatogram: second round of gel filtration.
(B) SDS-PAGE (upper panel) and native PAGE (lower panel) analysis of chromatographic fractions from first round of gel filtration. SDS-PAGE: Lane 1, protein marker (Fermentas); lanes 2 – 12, chromatographic fractions from the first round of gel filtration. Native PAGE: lanes 1 – 9, proteins corresponding to lanes 4 – 12 in the SDS-PAGE.
(C) SDS-PAGE (upper panel) and native PAGE (lower panel) analysis of chromatographic fractions from second round of gel filtration. SDS-PAGE: lane 1, protein marker (Fermentas); lanes 2 – 7, chromatographic fractions from the second round of gel filtration. Native PAGE: lanes 1 – 6, proteins corresponding to lanes 2 – 7 in the SDS-PAGE.
(D) Dynamic light-scattering (DLS) of purified pfDOHH.

Amino-acid sequence alignment suggested that there are 30 additional residues at the N-terminus of pfDOHH compared to that of human and yeast enzymes (Fig. 3.17). These residues likely correspond to signal peptide as predicted by Frommholz *et al*. (2009). Therefore, in order to increase the chance to crystallize pfDOHH, 27 or 43 residues at the N-terminus of the enzyme were deleted. The truncated recombinant proteins displayed the same behavior in size-exclusion chromatography and native electrophoresis (data not shown) as the full-length enzyme. Crystallization of these two truncated pfDOHHs was also not achieved. The failure of the crystallization experiments for pfDOHH is probably due to a long unstructured loop (the corresponding inter-domain loop in hsDOHH is about 60 residues shorter) present in the middle of the protein and impeding crystal formation.

3.3.2 *Plasmodium vivax* production and crystallization

Plasmodium vivax (pvDOHH) is also from a malaria parasite, but a sequence alignment indicated that it is closer to hsDOHH than to the enzyme from *Plasmodium falciparum* (Fig. 3.17). The putative inter-domain loop in pvDOHH is just about 20 residues longer than the corresponding loop in hsDOHH (Fig. 3.17). pvDOHH was overexpressed by using a GST-tagged expression construct. After cleavage of the GST tag, the majority of recombinant protein precipitated. The holo-form of pvDOHH could still be isolated from the remaining soluble protein by size-exclusion chromatography (Fig. 3.27 A). The isolated holo-pvDOHH showed a relatively compact band in the native electrophoresis, although it migrated much slower than holo-hsDOHH (Fig. 3.27 B & C). No crystallization hit was obtained from this preparation by screening with commercial crystallization kits.

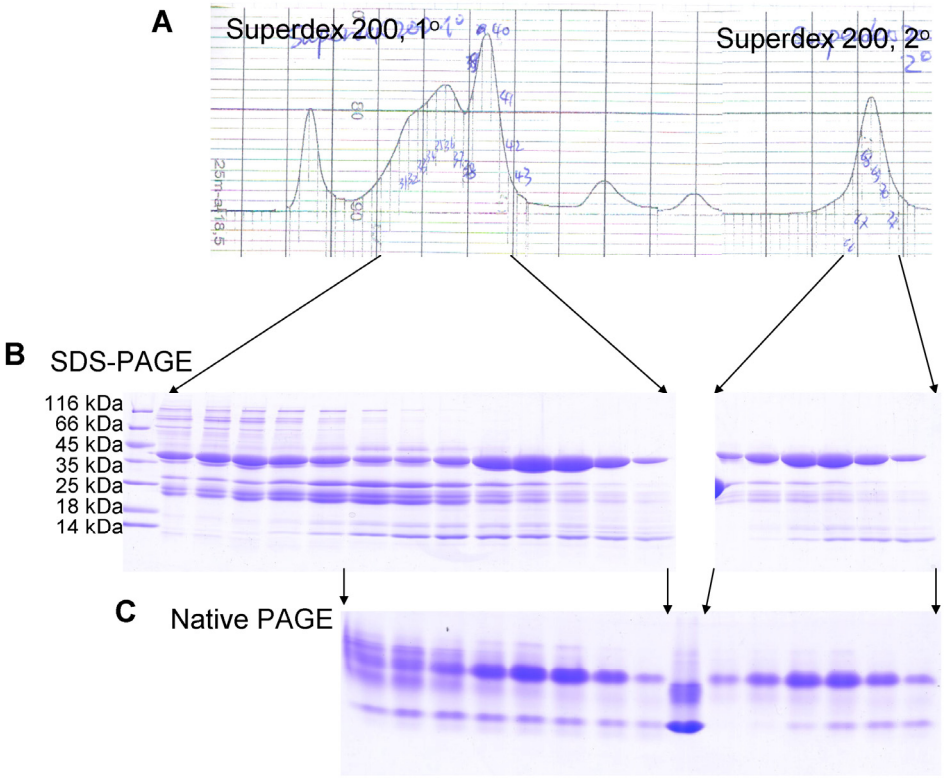

Fig. 3.27 Purification of pvDOHH.
(A) Size-exclusion chromatography of pvDOHH. Left chromatogram: first round of gel filtration; right chromatogram: second round of gel filtration.
(B) SDS-PAGE analysis of chromatographic fractions from first round (left) and second round (right) of gel filtration.
(C) Native PAGE analysis of chromatographic fractions from first round (left) and second round (right) of gel filtration. The sample in the middle of the PAGE gel is hsDOHH.

A series of N- or C-terminal truncated pvDOHHs was subjected to further crystallization trials. A construct (pvDOHH-T9, 8 residues from the N-terminus deleted) overcame the solubility issue of full-length enzyme and the truncated recombinant protein could be crystallized under many distinct conditions. The best crystals were found under a condition consisting of 8% Tacsimate (pH 8.0) and 18% PEG 3350 (Fig. 3.28). The crystals from this initial condition were tiny multi-crystals (Fig. 3.28 A). Bigger crystals were obtained by adding 1 mM $ZnCl_2$ and ~800 mM NDSB-195 (dimethylethylammonium propane sulfonate) to the initial crystallization condition. Single pvDOHH-T9 crystals were obtained by manipulating the big multi-crystals through a dissolution and

recrystallization procedure. The multi-crystals were dissolved in water and recrystallized by adding precipitant to the drop (Fig. 3.28 B).

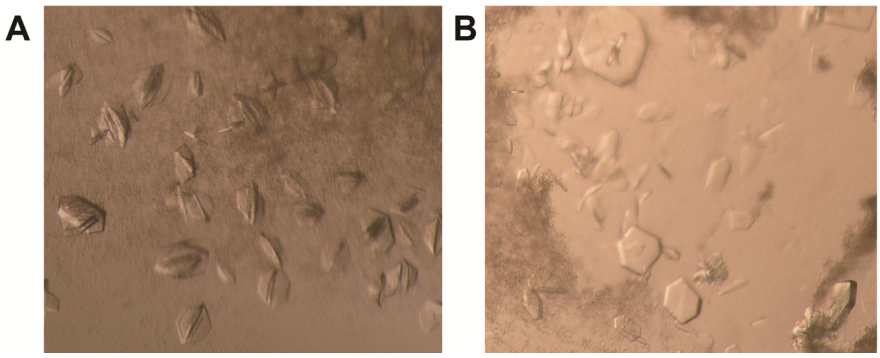

Fig.3.28 pvDOHH-T9 crystals.
(A) Crystals growing under initial crystallization condition.
(B) Crystals growing under optimized condition.

3.3.3 Spectroscopic studies

Both recombinant pfDOHH and pvDOHH displayed blue color after expression cells were broken. However, the intensity of the blue color significantly decreased within about 2 h at 4^{o}C. After completion of purification (normally within 48 h at 4^{o}C), the color of the protein became ambiguous (approximately brown) (Fig. 3.29 A). The freshly purified *Plasmodium* DOHH (pfDOHH and pvDOHH) showed weak absorption at long wavelengths (600 – 700 nm) (Fig. 3.29 B), implying that there was still a small amount of undecayed *μ*-1,2-peroxo-diiron(III) species present in the system. The absorption quickly disappeared within 2 h at room temperature (Fig. 3.29 B). These observations suggested that *Plasmodium* DOHH also features a *μ*-1,2-peroxo-diiron(III) core after exposure to O_2. However, the longevity of the *μ*-1,2-peroxo-diiron(III) species in *Plasmodium* DOHH is significantly shorter than that of hsDOHH or scDOHH.

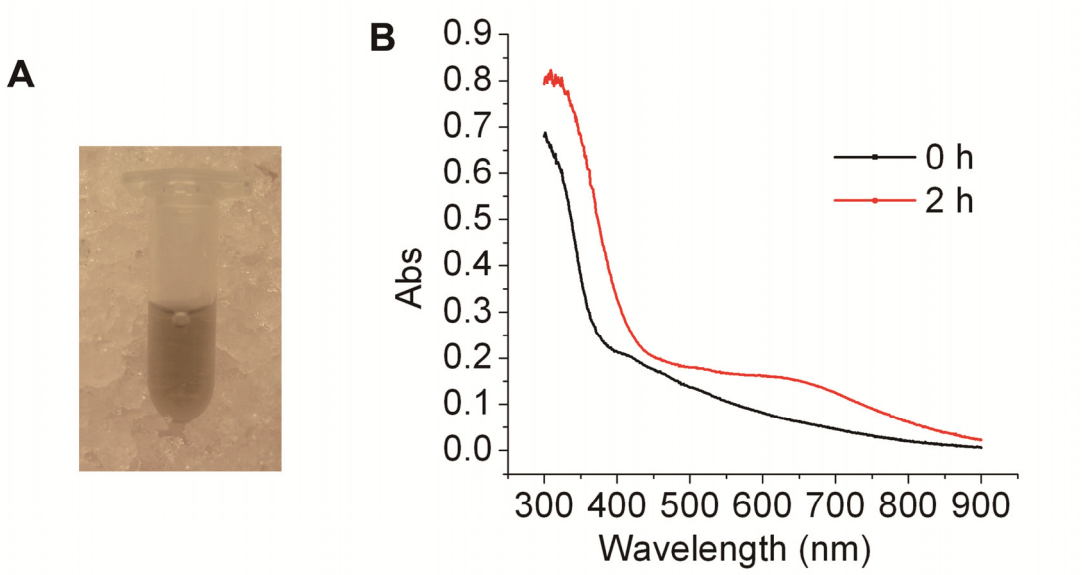

Fig. 2.29 Purified pvDOHH and UV/Vis spectra.
(A) The color of pvDOHH after completion of purification.
(B) UV/Vis spectra of pvDOHH.

3.3.4 Overall structure of pvDOHH

The structure of pvDOHH (pvDOHH-T9) was solved by molecular replacement with scDOHH as search model. Diffraction-data collection and structure refinement are summarized in Table 3.5.

Table 3.5 Crystallographic data and refinement statistics of pvDOHH

Data-collection statistics	
X-ray source	BL14.2, BESSY II
Wavelength, Å	0.91841
Space group	$P2_12_12$
Unit cell parameters, Å	a = 59.73, b = 131.66, c = 133.94
Resolution range, Å	50.40 - 2.40 (2.53 - 2.40)
Reflections	291,648 (38,252)
Unique reflections	41,751 (5742)
R_{merge} [1]	0.151 (0.815)
R_{pim} [2]	0.061 (0.339)
$CC_{1/2}$ [3]	0.995 (0.735)
$I/\sigma(I)$	7.9 (2.1)
Redundancy	7.0 (6.7)
Completeness, %	99.4 (95.7)
Wilson B factor, Å^2	31.5
Refinement statistics	
Refinement resolution, Å	19.82 - 2.40
No. reflections	39,490
R_{work}/R_{free} (% of refls.) [4]	0.206/0.248 (5%)
Average B factor, Å^2	50.90
Unmodeled residues	Chain A: 157 - 163; 192 - 195 Chain B: 154 - 176, 192 - 195;
No. of atoms	
Protein	5056
Water	79
Other	16
Bond lengths, Å	0.014
Bond angles, deg.	1.749
Ramachandran favored, %	96.30
Ramachandran outliers, %	0.16
Clashscore [5]	7.15
MolProbity score [5]	2.49

[1] $R_{merge} = \Sigma_{hkl}\Sigma_i|I_i(hkl) - \langle I_i(hkl)\rangle| / \Sigma_{hkl}\Sigma_i {}^{I_i(hkl)}$.

[2] Precision-indicating merging R factor. R_{pim} is defined as $\Sigma_{hkl}[1/(N-1)]^{1/2}$ $\Sigma_i|I_i(hkl) - \langle I(hkl)\rangle| / \Sigma_{hkl}\Sigma_i {}^{I_i(hkl)}$, N is redundancy (Weiss & Hilgenfeld, 1997).

[3] Correlation coefficient between two random-half data sets (Karplus & Diederichs, 2012).

[4] $R_{work} = \sum_{hkl}|F_{obs} - F_{calc}| / \sum_{hkl}F_{obs}$. R_{free} serves as cross-validation of the R-factor. 5% of the reflections were set aside for the calculation of the free R-factor (Brünger, 1992).

[5] log-weighted combination of the clashscore, percentage of non-favored conformations according to the Ramachandran plot, and percentage of bad side-chain rotamers (Chen *et al.*, 2010).

There are two copies of the pvDOHH monomer in the asymmetric unit (molecules A and B). The overall structure of pvDOHH is similar to that of hsDOHH and scDOHH. The pvDOHH and hsDOHH (POX) structures can be superimposed with a Cα r.m.s. deviation of about 1.35 Å (pvDOHH molecule A and POX molecule A). pvDOHH consists of N- and C-terminal α-helix stacks, which are connected by an extremely long inter-domain linker (residues 152 –199) (Fig. 3.30 A). Several regions in this linker (residues 157 – 163 in molecule A, residues 154 – 176 in molecule B, and residues 192 – 195 in both molecules) are disordered in the structure. An α-helix (α_{loop}) (residues 165 –177) is present in the inter-domain linker (Fig. 3.30 A). The α_{loop} in pvDOHH is much longer than the corresponding α-helix in the structure of scDOHH (Fig. 3.30 B).

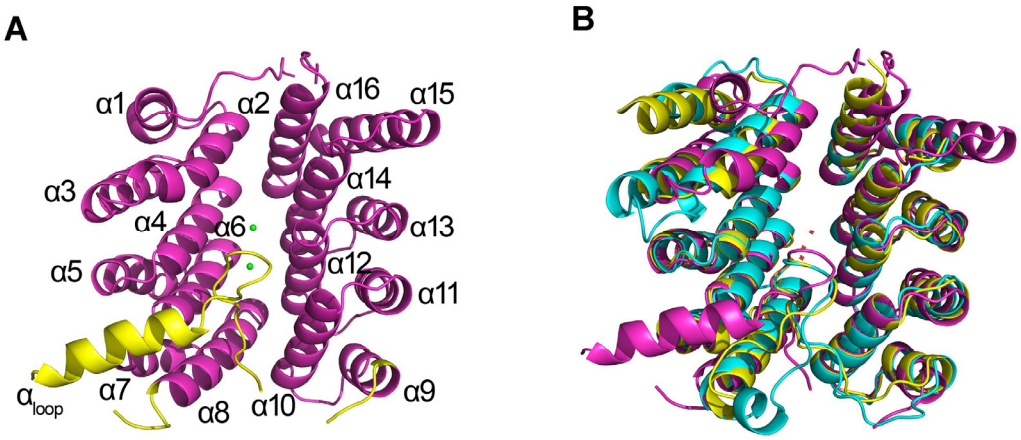

Fig. 3.30 Structure of pvDOHH.
(A) Cartoon presentation of pvDOHH. The inter-domain region is shown in yellow.
(B) Superposition of the overall structures of pvDOHH, hsDOHH (POX), and scDOHH. pvDOHH, hsDOHH, and scDOHH are shown in magenta, yellow, and cyan, respectively.

3.3.5 Diiron site of pvDOHH

The diiron site of pvDOHH is located in the interface of the N- and C-terminal α-helix stacks. Fe1 is coordinated by His108, Glu109, and His250; Fe2 is coordinated by His75, Glu76, His283, and Glu284 (Fig. 3.31 A). Thus, diiron site of pvDOHH possesses a 4H-3E ligand set. All the histidines are arranged

in the same hemisphere of the diiron site and coordinate iron atoms through their Nε atoms. All of the glutamates terminally coordinate the iron atoms in a monodentate fashion (Fig. 3.31 A). The Fe–O (carboxylate Oε2) and Fe–N (histidine Nε) distances vary from 1.61 to 1.72 Å and 2.02 to 2.23 Å, respectively (Fig. 3.31 A) (Table 3.6). The diiron site environment in pvDOHH is not as symmetric as that of hsDOHH and scDOHH, since the residues corresponding to Glu76 in hsDOHH (Glu57) and scDOHH (Glu80) are not involved in the coordination of Fe2 (Fig. 3.31 B).

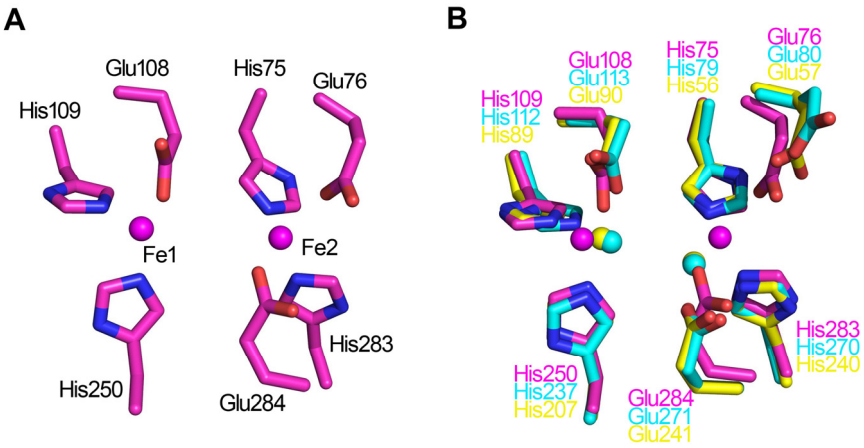

Fig. 3.31 Diiron site of pvDOHH.
(A) Diiron site of pvDOHH. Carbon, nitrogen, oxygen, and iron are shown in magenta, blue, red, and magenta, respectively.
(B) Superposition of the diiron ligand sets of pvDOHH, hsDOHH, and scDOHH. Carbon and iron atoms from pvDOHH, hsDOHH, and scDOHH are shown in magenta, yellow, and cyan, respectively.

Table 3.6 Selected geometric parameters and atomic temperature factors in pvDOHH diiron core

		Molecule A	Molecule B
Distances, Å	Fe-Fe	5.31	5.34
	Fe-N (His75)	2.06	2.12
	Fe-N (His108)	2.23	2.21
	Fe-O (Glu109 OE2)	1.66	1.61
	Fe-N (His250)	2.02	2.05
	Fe-N (His283)	2.13	2.23
	Fe-O (Glu284 OE2)	1.72	1.71
	Fe-O (Glu76 OE1)	2.35	2.30
	Glu76 OE1 - Tyr44 OH	2.99	3.00
B-factors, $Å^2$	Fe1	28.99	43.53
	Fe2	32.46	43.06

Fe-Fe distance in pvDOHH is 5.34 Å and 5.31 Å in molecule A and B, respectively (Table 3.6). The distances are much longer than known Fe-Fe distances (2.5 – 4.3 Å) for non-heme diiron proteins in the literature.

3.3.6 Secondary coordination sphere of pvDOHH

The residues in the secondary coordination sphere of the diiron site in pvDOHH are quite different from those of hsDOHH and scDOHH. From the Fe1 to the Fe2 site, residual pairs Glu112/Glu251, Tyr79/Phe254, and Tyr44/Leu287 are sequentially arranged in the hemisphere above the diiron site (Fig. 3.32 A). Glu112/Glu251 is located 3.62/5.38 Å (Glu112 Oε1/Glu251 Oε1) away from Fe1. The distances between the hydroxyl group of Tyr79 and the iron atoms are around 8 Å. In hsDOHH and scDOHH, the residue corresponding to Phe254 is a tyrosine (Fig. 3.32 B). Tyr44 and Leu287 are replaced by a phenylalanine and glutamate, respectively, in hsDOHH and scDOHH. Tyr44 and Glu76 are connected by a hydrogen bond (2.99 and 3.00 Å from the hydroxyl group of Tyr44 to Glu76 Oε1 in molecule A and B, respectively) (Fig. 3.32 A).

The residues in the hemisphere below the diiron site are similar to those of hsDOHH and scDOHH (Fig. 3.32 A & B). Ile247 and Leu72 are located near Fe1 and Fe2, respectively. The methionine pair Met105/Met280 is situated just below the diiron site (Fig. 3.32 A). The distances between the methionine residues and the iron atoms are about 6 Å (sulfur atoms of methionines to each of iron atoms). Met105 and Met280 are 4.23 and 4.94 Å from each other (measured between methionine Cγ atoms) in molecule A and B, respectively. As in hsDOHH and scDOHH, this methionine pair separates the diiron site from solvent in pvDOHH.

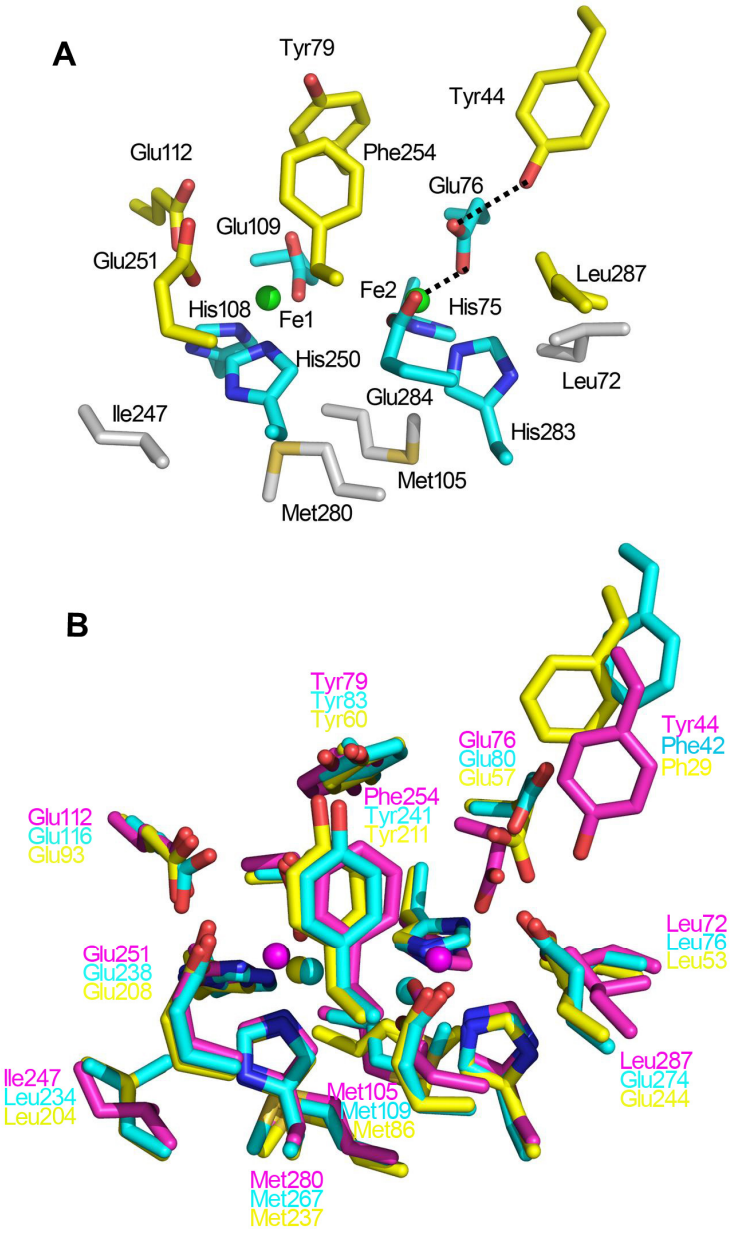

Fig. 3.32 Secondary coordination sphere of the pvDOHH diiron core.
(A) Secondary coordination sphere of the pvDOHH diiron core. The carbon atoms of residues in the primary coordination sphere are shown in cyan. Those of the residues above and below the diiron site in the secondary coordination sphere are shown in yellow and grey, respectively.
(B) Superposition of the primary and secondary coordination spheres of pvDOHH, hsDOHH, and scDOHH. Carbon atoms from pvDOHH, hsDOHH, and scDOHH are shown in magenta, yellow, and cyan, respectively.

3.3.7 Substrate-binding site of pvDOHH

The substrate-binding site of pvDOHH is located in the interface of the N- and C-terminal helical domains (Fig. 3.33 A). Residues from α2, α4, α12, α14, α16,

and the inter-domain loop constitute the external cavity. Residues Glu76, Tyr79, Phe254, and Glu284 form the entrance of the inner cavity and the glutamate pair Glu112/Glu251 is located at the bottom of the inner cavity (Fig. 3.33 B). The inner cavity is about 10 Å deep with the diiron site at one of its walls. The residues constructing the body of the inner cavity include iron ligands (His75, His108, Glu109, His250, His283, and Glu284) and the residues from the secondary coordination sphere (Tyr79 and Phe254) (Fig. 3.33 B).

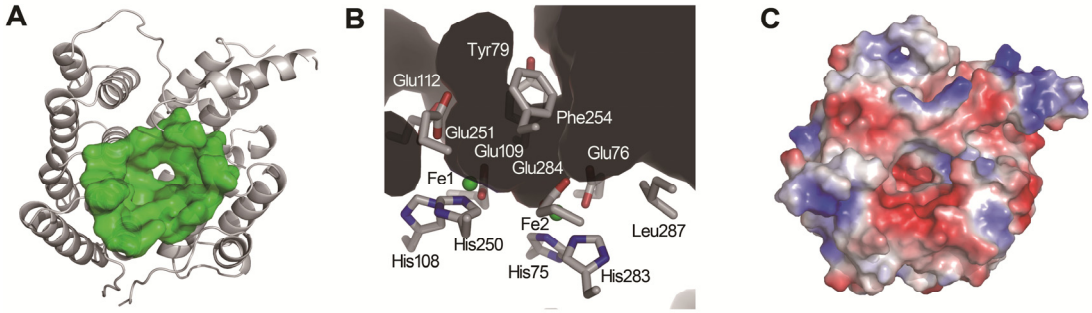

Fig. 3.33 Substrate-binding cavity in pvDOHH.
(A) The location of the substrate-binding cavity in pvDOHH. The residues constituting the external cavity are presented in green surface.
(B) The residues forming the inner cavity. Carbon, nitrogen, oxygen, and iron are presented in grey, blue, red, and green, respectively.
(C) Surface charge-distribution of pvDOHH. Red: negative; blue: positive.

Both the inner cavity and the external cavity are largely negatively charged (Fig. 3.33 C). However, compared to hsDOHH and scDOHH, the hydrophilicity of the entire cavity in pvDOHH is relatively weak because of the presence of the hydrophobic residues Phe254 and Leu287 in the cavity. Although the residue corresponding to Leu287 in scDOHH is a glutamate (Glu274), which was found to be important for substrate-binding (Cano *et al*., 2010), a negatively charged residue at this position seems not to be essential in pvDOHH.

3.4 Discussion of the DOHH results

3.4.1 Non-heme diiron proteins: diverse functions and similar diiron-core topology

The proteins harboring a non-heme diiron core display a large functional diversity. A summary of the functions of non-heme diiron proteins is shown in Table 3.7. DOHH is a recently identified non-heme diiron enzyme which specifically catalyzes the biosynthesis of Hpu. The crystal structures reveal that the diiron site of DOHH is coordinated by four histidines and two (or three) glutamates that are situated in four α-helices (α4, α6, α12, and α14) (Fig. 3.34 A - C). Such a diiron core architecture is similar to the common topology observed in many other non-heme diiron proteins. First, diiron site is coordinated by conserved histidines and glutamates (or aspatate) (Table 3.7); second, diiron site is surrounded by a four-α-helix bundle which supplies the residues as iron ligands (Fig. 3.34 D - K) (Summa *et al.*, 1999; Gomes *et al.*, 2001).

Compared to other non-heme diiron proteins, the four α-helices in the diiron core of DOHH displays several unique features, so that they cannot be superimposed with the four-α-helix bundles from the other non-heme diiron proteins. In DOHH, the four helices involved in diiron coordination are very short (12 – 13 residues) and display considerable amino-acid sequence identity. The α-helices in other non-heme diiron proteins (with an exception of Hr) are at least double the lengths of the helices in DOHH (Fig. 3.34 D - K). In DOHH, α-helices from same domain (α4/α6 and α12/α14 from the N- or C-terminal domain, respectively) are almost parallel and inter-helical angles between the helices from different domains (α4/α12, α6/α14, α2/α14, and α6/α12) vary from 67 - 72^{o} (Fig. 3.34 A - C), whereas in other non-heme diiron proteins, the four α-helices largely lengthwise pack against each other and the helix-helix angles are normally about 20^{o}.

Table 3.7 Functions of non-heme diiron proteins

Protein	Abbrev.	Diiron site	Function
Hydroxylase subunit of soluble methane monooxygenase [1]	sMMOH	2H-4E	Hydroxylation of methane to methanol
R2 subunit of ribonucleotide reductase [1]	RNR-R2	2H-4E	*de novo* synthesis of deoxyribonucleotides
Heavy-type ferritin (vertebrates) and M-type ferritin (amphibians) [2, 3]	H-ferritin M-ferritin	1H-3E	Iron storage and ferroxidase activity (conversion of iron from Fe(II) to Fe(III))
Stearoyl-acyl carrier protein Δ^9 desaturase [4]	Δ^9D	2H-4E	Creates a double bond in Stearoyl-CoA
Hydroxylase subunit of toluene monooxygenase [1, 5]	ToMOH T2moH, T3moH, T4moH	2H-4E	Hydroxylation of toluenes
Hydroxylase subunit of phenol monooxygenase [6]	PMOH	2H-4E	Hydroxylation of phenol to catechol
Hydroxylase subunit of alkene monooxygenase [7]	AMOH		Epoxidation of alkenes
p-aminobenzoate *N*-oxygenase [8]	AurF	2H-4E	Oxidation of *p*-aminobenzoate to *p*-nitrobenzoate
Aldehyde-deformylating oxygenase [9]	ADO	2H-4E	Conversion of fatty aldehydes to alkenes
Hemerythrin [10]	Hr, oxyHr, metHr	5H-2E	O_2 transport in marine invertebrates
myo-inositol oxygenase [11]	MIOX	4H-2E	Catalyzes conversion of *myo*-inositol to D-glucuronate
Rubrerythrin [12, 13]	Rr	1H-5E	Ferroxidase and peroxidase
Deoxyhypusine hydroxylase [14]	DOHH	4H-2E	Hydroxylation of Dhp-eIF5A

[1] Wallar & Lipscomb, 1996. [2] Crichton & Declercq, 2010. [3] Bertini *et al*., 2012. [4] Lindqvist *et al*., 1996. [5] McCormick *et al*., 2006. [6] McCormick & Lippard, 2011. [7] Gallagher *et al*., 1997. [8] Choi *et al*., 2008. [9] Khara *et al*., 2013. [10] Holmes *et al*., 1991. [11] Brown *et al*., 2006. [12] deMaré *et al*., 1996. [13] Coulter *et al*., 2000. [14] This work.

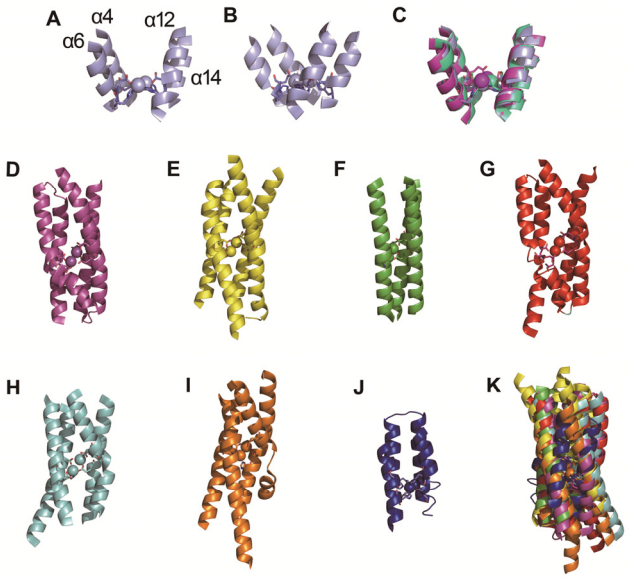

Fig. 3.34 The diiron core architecture in DOHH and the other non-heme diiron proteins.
(A) hsDOHH (POX structure)
(B) As in (A), in another orientation (90^{o} clockwise rotation of (A)).
(C) Superposition of four-α-helix bundles from hsDOHH, scDOHH, and pvDOHH. Light blue: hsDOHH; greencyan: scDOHH; magenta: pvDOHH.
(D) sMMOH (PDB code: 1MMO, Rosenzweig *et al*., 1993).
(E) RNR-R2 (PDB code: 1MXR, Högbom *et al*., 2003).
(F) Ferritin (PDB code: 3RBC, Bertini *et al*., 2012).
(G) ToMOH (PDB code: 2INC, McCormick *et al*., 2006).
(H) Δ^{9}D (PDB code: 1AFR, Lindqvist *et al*., 1996).
(I) Aurf (PDB code: 3CHH, Choi *et al*., 2008).
(J) Hr (PDB code: 1HMO, Holmes *et al*., 1991).
(K) Superposition of D – J.

The structural similarities of the diiron center between DOHH and the other non-heme diiron proteins imply that DOHH is derived from a common ancestor of those of four-α-helix bundle diiron proteins. The ancestor plays a role in protecting anaerobic organisms in aerobic environment through reduction of O_2 to water (Gomes *et al*., 2001). This primitive function is still kept in sMMO (Gassner & Lippard, 1999), RNR (Tong *et al*., 1996), and Δ^{9}D (Broadwater *et al*., 1998). Whether the oxygen reductase activity is present in DOHH is an interesting question to be investigated.

3.4.2 Nature of the peroxo-diiron(III) intermediate

In general, the reduced diiron site experiences a series of intermediate species after activation by O_2. To investigate these intermediates in the reaction cycle of diiron enzymes is an attractive topic for chemists and biologists in this field.

The peroxo-diiron(III) species is the first intermediate featuring an oxidized diiron cluster after O_2-activation (Krebs *et al*., 2011). It is a key intermediate within the oxygenation sequence since for many of the non-heme diiron proteins, the peroxo intermediate has been detected spectroscopically. So far, peroxo-diiron(III) intermediates have been found for oxyHr (Klotz & Kurtz, 1984), human H-ferritin (Treffry *et al*., 1995), sMMOH (Liu *et al.*, 1995a), RNR-R2 (Moënne-Loccoz *et al.*, 1998), bull frog M-ferritin (Moënne-Loccoz *et al.*, 1999; Krebs *et al*., 2002), Δ^9D (Broadwater *et al*., 1998, 1999), ToMOH (Murray *et al*., 2007; Song *et al*., 2009), hsDOHH (Vu *et al*., 2009), and ADO (Pandelia *et al*., 2013).

The spectroscopic properties of the hsDOHH peroxo intermediate resemble those of typical peroxo intermediates found in the reaction cycle of ferritin, RNR-R2, sMMOH, and Δ^9D, which display a series of common spectroscopic characteristics: 1) v(O-O) frequencies of 844 – 898 cm^{-1} in resonance Raman spectroscopy which is a typical O-O stretching frequency for peroxide ligands (O_2, 1561 cm^{-1}; superoxo (O_2^-), 1075 – 1165 cm^{-1}; peroxo (O_2^{2-}), 738 – 880 cm^{-1}) (Klotz & Kurtz, 1984); 2) antiferromagnetically coupled diiron cluster: Mössbauer parameters δ = 0.55 – 0.68 mm/s and ΔE_Q > 0.9 mm/s; 3) optical absorption band of 630 – 725 nm, which gives rise to the typical blue color of the intermediate (Table 3.8). The peroxo-diiron(III) intermediates in these enzymes and DOHH have been assigned as end-on, bridging peroxo-diiron(III) species (μ-1,2-peroxo-diiron(III)) (Model I in Fig. 1.9) based on the structures of biomimetic synthetic complexes displaying similar charge-transfer bands, Mössbauer parameters, and Raman bands (Table 3.9).

Table 3.8 Spectroscopic properties of peroxo-diiron(III) intermediates

Protein	λ_{max}, nm	Mössbauer		Exchange	Raman	Fe-Fe
	(ε, M-1 cm-1)	δ, mm/s	ΔE_Q, mm/s	coupling J, cm^{-1}	ν(O-O), cm^{-1}	distance,Å
sMMOH (*Mt*) [1]	725 (2500) [2]	0.67 [3]	1.51 [3]			
sMMOH (*Mc*) [4]	420 (3880), [5]	0.66 [6]	1.51 [6]			
RNR-R2 D84E	700 (1500) [7]	0.63 [7]	1.58 [7]	50 ± 10 [8]		
RNR-R2 W48F/D84E	700 [9]				870 [9]	2.50 [10]
M-ferritin	650 [11]	0.62 [11]	1.08 [11]	75 ± 10 [8]	851 [12]	2.53 [13]
H-ferritin	650 [14]	0.58, 0.55 [15]	1.07, 1.11 [15]			
Δ^9D	700 (1200) [16]	0.68, 0.64 [16]	1.90, 1.06 [16]		898 [17]	
ToMOH		0.55 [18]	0.67 [18]			
ToMOH T201S (1)		0.55 [19]	0.70 [19]			
ToMOH T201S (2)	675 [19]	0.67 [19]	1.51 [19]			
AurF	500 [20]	0.54, 0.61 [20]	-0.66, 0.35 [20]			
ADO	450 (1200) [21]	0.48, 0.55 [21]	0.45, 1.23 [21]			
oxyHr	500 [22-24]	0.51, 0.54 [22]	1.09, 1.92 [22]	-77 [23]	844 [24]	
hsDOHH (1)[25]	630 (2800) [26]	0.55, 0.58 [26]	1.16, 0.88 [26]	50 – 70 [26]	855 [26]	3.44 [26]
hsDOHH (1)[25]	630 [27]	0.55, 0.57 [27]	1.17, 0.85 [27]			
hsDOHH (2)[25]	600 [27]	0.62, 0.62 [27]	0.71, 1.25 [27]			

[1] *Methylosinus trichosporium* OB3b. [2] Lee & Lipscomb, 1999. [3] Shu *et al*., 1997. [4] *Methylococcus capsulatus* (Bath). [5] Tinberg & Lippard, 2009. [6] Liu *et al*., 1995b. [7] Bollinger *et al*., 1998. [8] Krebs *et al*., 2002. [9] Moënne-Loccoz *et al*., 1998. [10] Baldwin *et al*., 2003. [11] Pereira *et al*., 1998. [12] Moënne-Loccoz *et al*., 1999. [13] Hwang *et al*., 2000. [14] Treffry *et al*., 1995. [15] Bou-Abdallah *et al*., 2002. [16] Broadwater *et al*., 1999. [17] Broadwater *et al*., 1998. [18] Murray *et al*., 2007. [19] Song *et al*., 2009 (two peroxo intermediates were detected, $ToMOH_{peroxo}$ and $T201S_{peroxo}$). [20] Korboukh *et al*, 2009. [21] Pandelia *et al*., 2013. [22] Okamura *et al*., 1969. [23] Dawson *et al*., 1972. [24] Dunn *et al*, 1973. [25] hsDOHH (1): peroxo intermediate of hsDOHH (fresh preparation); hsDOHH (2): hsDOHH polycrystals (48 h aged hsDOHH). [26] Vu *et al*., 2009. [27] this work.

Table 3.9 Structural and spectroscopic properties of synthetic model complexes for peroxo-diiron(III) intermediates

Model complex	λ_{max}, nm (ε, M-1 cm-1)	Mössbauer		Raman v(O-O), cm^{-1}	Fe-Fe, Å	Fe-O, Å [5]	O-O, Å	Fe-O-O-Fe, Deg.
		δ, mm/s	ΔE_Q, mm/s					
$[Fe_2(\mu\text{-}O_2)(\mu\text{-}O_2CCH_2Ph)_2\{HB(pz')_3\}_2]$ [1]	694 (2650)	0.66	1.40	888	4.00	1.91	1.41	52.3
						1.88		53.5
$[Fe_2(6\text{-}Me_2\text{-}BPP)_2(O)(O_2)]$ [2]	577 (1500)	0.50	1.46	847	3.17		1.41	
$[Fe_2(6\text{-}Me_2\text{-}BPP)_2(OH)(O_2)]$ [2]	644 (3000)	0.50	1.31	908	3.40	1.87	1.40	-14.5
						1.89		
$[Fe_2(Ph\text{-}bimp)(C_6H_5COO)(O_2)]^{2+}$ [3]	500 – 800	0.58	0.74		3.33	1.94	1.43	9.9
	(1700)	0.65	1.70			1.86		
$[Fe_2(\mu\text{-}1,2\text{-}O_2)(N\text{-}Et\text{-}hptb)(Ph_3PO)_2)]^{3+}$ [4]					3.46	1.88	1.42	

[1] Kim & Lippard, 1996. [2] Zhang *et al.*, 2005. [3] Ookubo *et al.*, 1996. [4] Dong et al., 1996. [5] O is from peroxo unit.

Spectroscopic features of the hsDOHH peroxo intermediate are distinct from those of recently identified peroxo species trapped in the reaction cycle of ToMOH, AurF, and ADO. The peroxo intermediate of these proteins is devoid of absorption at long-wavelengths (> 600 nm) (AurF shows a weak absorption band at 500 nm; ADO features an absorption band at 450 nm) and shows relatively small Mössbauer parameters (Table 3.8). Moreover, the presence of the peroxo unit in the diiron site has not been observed by Raman spectroscopy for ToMOH, AurF, and ADO. The diiron core geometry of the peroxo intermediate of ToMOH, AurF, and ADO was proposed to be *μ*-1,1-peroxo-diiron(III) (Murray *et al*., 2007; Korboukh *et al*, 2009; Pandelia *et al*., 2013) (Model IV in Fig. 1.8). The O_2-binding diiron site in oxyHr was characterized early as a peroxo species (Klotz & Kurtz, 1984). The optical property and Mössbauer parameters of oxyHr are similar to those of ToMOH (Table 3.8). However, Raman spectroscopy and X-ray crystallography revealed that an end-on hydroperoxo terminally binds to the diiron site of oxyHr (Model VI in Fig. 1.8). Such a non-bridging peroxo ligand in the diiron site of oxyHr is distinct from all the other proposed geometries of the peroxo unit mentioned above.

It is obvious that not all peroxo-diiron(III) species show the typical spectroscopic properties (such as blue color) as observed for those of DOHH and sMMOH. The antimagnetically coupled diiron(III) cluster revealed by Mössbauer spectroscopy is the only spectroscopic feature shared by all peroxo-diiron(III) species (Table 3.8). Therefore, in the reaction cycle of a non-heme diiron oxygenase or oxidase, the peroxo-diiron(III) intermediate can be roughly defined by its biological nature: 1) the species is directly generated from the reaction between the diiron(II) core and O_2; 2) it is able to fulfill an enzymatic function (generate product); 3) it converts to the resting state featuring a *μ*-oxo/hydroxyl-diiron(III) core at the end of the reaction sequence.

3.4.3 Crystallographic studies of the peroxo-diiron(III) intermediate

Although the characteristics of the peroxo-diiron(III) intermediate can be investigated by spectroscopic studies, there is no better way to visualize the structure of the peroxo-diiron(III) intermediate directly. However, there are many difficulties in obtaining the X-ray structure of the peroxo form of these proteins. First, the life-time of the peroxo intermediate normally is very short. The intermediate would not survive during the crystallization procedure. Second, the peroxo ligand is a very simple, small molecule consisting of two oxygen atoms and one inter-atomic bond which is difficult to be confirmed by electron density at normal resolution (~2 Å). Therefore, interpretation of the electron density corresponding to the peroxo ligand is a big challenge. Third, the redox-sensitive nature of the diiron site results in an ambiguous assignment of the iron oxidation state when the diffraction data are collected at a synchrotron beamline. Actually, this is a common problem for structure determination of metalloproteins (Corbett *et al*., 2007). Forth, the detailed geometry of the diiron cluster more or less depends on the choice and application of restraints during structure refinement.

Even so, two X-ray structures of diiron proteins in their peroxo-diiron(III) state can be found in the literature. One structure is oxygenation form of Hr (oxyHr) which was solved almost 25 years ago (Holmes *et al*., 1991). The structure shows that the peroxo ligand terminally binds to one iron site in end-on mode, consistent with the conclusion based on spectroscopic studies. Fig. 3.35 A shows the $2F_o$-F_c map around the diiron site of oxyHr. It can be seen that the peroxo unit was built in a small piece of electron density (at 1.0σ). Another peroxo-diiron(III) structure is T4moH which was determined from the crystals soaked in 300 mM H_2O_2 (Bailey & Fox, 2009). As shown in Fig. 3.35 B, a large area of electron density below the diiron site is assigned as two peroxo ligands. According to the quality of the electron density map around the diiron site, the assigned peroxo model in these two structures is not convincing. Compared to

these two structures of a peroxo-diiron(III) intermediate, the peroxo intermediate of hsDOHH (POX structure) shows much more reasonable electron density for the assigned peroxo ligand (Fig. 3.35 C).

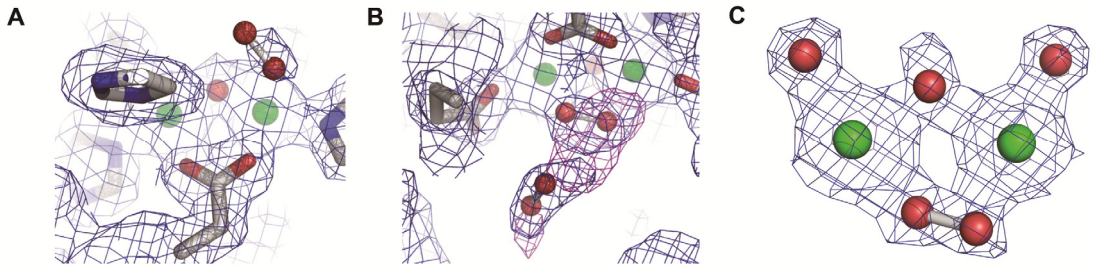

Fig. 3.35 Electron density maps around the diiron sites of peroxo-diiron(III) intermediates. Carbon, oxygen, nitrogen, and iron are shown in grey, red, blue, and green, respectively.
(A) Electron density map around the diiron site of oxyHr (PDB code: 1HMO, Holmes *et al*., 1991). Blue mesh: $2F_o$-F_c map at 1.0σ.
(B) Electron density map around the diiron site of T4moH (PDB code: 3I63, Bailey & Fox, 2009). Blue mesh: $2F_o$-F_c map at 1.5σ; magenta mesh: F_o-F_c map at 3.0σ.
(C) Electron density map around the diiron site of the hsDOHH POX structure. Blue mesh: $2F_o$-F_c map at 1.5σ.

In the hsDOHH POX structures, the Fe-O(peroxo) distances vary between 2.17 and 2.23 Å, consistent with Fe-O(peroxo) distances of 2.07 – 2.35 Å observed in the structures of oxyHr and T4moH (Holmes *et al*., 1991; Bailey & Fox, 2009). However, the distances are longer than the Fe-O(peroxo) distances observed in the structures of model complexes (Table 3.9) and the theoretical structures derived from DFT calculations (Dunietz *et al*., 2000; Skulan *et al*., 2004; Fiedler *et al*., 2008; Jensen *et al*., 2009) where the Fe-O(peroxo) bonds are normally within the range 1.80 to 1.90 Å. Our DFT structures for the diiron core of hsDOHH peroxo intermediates (Model H and I) (Fig. 3.13; Table 3.3) also show a smaller Fe-O(peroxo) distances (1.90 – 2.00 Å). A similar discrepancy between protein and model complex structures of peroxo intermediates is also found for the O-O distance (Table 3.9). These discrepancies likely become smaller if appropriate restraints were applied or can be neglected since the resolution of protein structures is much lower than

the resolution of small model complexes.

We cannot exclude that the diiron(III) site in DOHH was partially reduced during diffraction data collection. The same issue is likely also present for a large number of X-ray structures of metalloproteins. Because the crystals of scDOHH are big enough, it could be seen that the color changed from blue (peroxo intermediate) to colorless during data collection implying that iron(III) atoms were severely reduced by X-rays. Such a color change was not observed for hsDOHH crystals because their size was smaller than that of scDOHH crystals. However, the reduction effect occurring in hsDOHH crystals should be weaker than in scDOHH crystals, since the X-ray intensity at BESSY is weaker than that of PETRA III (diffraction data of hsDOHH and scDOHH were collected at BESSY and PETRA III, respectively). In order to overcome synchrotron X-ray-induced photoreduction for metalloproteins, incorporation of spectroscopic techniques into crystallographic beamlines has been proposed (Katona *et al*., 2007; Ellis *et al*., 2008).

3.4.4 Base of the extreme longevity of peroxo-diiron(III) intermediate in DOHH

The lifetime of the peoxo-diiron(III) core in enzymes of this kind is normally very short. Table 3.10 shows a summary of peoxo-diiron(III) species in enzymes. Although DOHH belongs to those typical peroxo-diiron(III) enzymes, the peroxo-diiron(III) intermediate in DOHH is unusually stable.

Table 3.10 Properties of peroxodiiron(III) in non-heme diiron enzymes

Enzyme	Peroxo geometry [1]	Coordination Ligands [2]	Half-life, s
hDOHH [3]	μ-1,2	4H-2E	Stable
Bullfrog M-ferritin [4]	μ-1,2	1H-3E	0.165 (23°C)
Human H-ferritin [5]	μ-1,2	1H-D-2E	0.25; 1.9 (25°C)
sMMOH [6]	μ-1,2	2H-4E	0.7-2.3 (4°C)
Δ^9D [7]	μ-1,2	2H-4E	1540 (RT)
RNR-R2 D84E [8]	μ-1,2	2H-4E	0.75-1.17 (5°C)
RNR-R2 W48D/D84E [9]	μ-1,2	2H-4E	2.67 (5°C)
AurF [10]	μ-1,1 ?	3H-4E	420 (20°C)
ToMOH ($ToMOH_{peroxo}$) [11]	μ-1,1 ?	2H-4E	15.4 (4°C)
ToMOH T201S ($T201S_{peroxo}$) [12]	μ-1,2	2H-4E	0.23 (4°C)
ADO [13]	μ-1,1 ?	2H-3E	400 (5°C)

[1] The peroxo geometry of hsDOHH was confirmed by spectroscopic data and X-ray crystallography (POX; this work); those of other enzymes were obtained from spectroscopic data in the literature. [2] Amino-acid ligands of the primary coordination sphere of the diiron site of hsDOHH were derived from the POX structure; those of other enzymes refer to the structures of the enzymes in the resting state. Bullfrog M-ferritin, PDB code: 3RBC (Bertini *et al*., 2012); human H-ferritin (Zn derivative), PDB code: 2CEI (Toussaint *et al*., 2007); sMMOH, PDB code: 1MMO (Rosenzweig *et al*., 1993); Δ^9D, PDB code: 1AFR (Lindqvist *et al*., 1996); RNR-R2 variants, PDB code: 1PIU (Voegtli *et al*., 2000); AurF, 3CHH (Choi *et al*., 2008); ToMOH, PDB code: 2INC (McCormick *et al*., 2006); ToMOH T201S, PDB code: 3N1Z (Song *et al*., 2010); ADO, PDB code: 2OC5. [3] hsDOHH, human deoxyhypusine hydroxylase (this work and Vu *et al*. (2009)). [4] Data from references Moënne-Loccoz *et al*., 1999 and Bertini *et al*., 2012. [5] Data from reference Bou-Abdallah *et al*., 2005. Two peroxo species were detected in the ferroxidase site of human ferritin. Peroxo species B is followed by a putative diiron(III)-hydroperoxo species B', with half-lifes of 0.25 s and 1.9 s, respectively. [6] sMMOH, soluble methane monooxygenase hydroxylase (data from references Rosenzweig *et al*., 1993, Lee *et al*., 1993a, and Liu *et al*., 1994, 1995a). [7] Δ^9D, stearoyl-acyl carrier protein Δ^9-desaturase (data from references Lindqvist *et al*., 1996 and Broadwater *et al*., 1998). RT, room temperature. [8] RNR-R2 D84E, ribonucleotide reductase subunit R2 variants (data from references Bollinger *et al*., 1998 and Voegtli *et al*., 2000). [9] RNR-R2 D84E, ribonucleotide reductase subunit R2 double mutant (data from references Moënne-Loccoz *et al*., 1998 and Voegtli *et al*., 2000). [10] AurF, *p*-aminobenzoate *N*-oxygenase (data from references Korboukh *et al*., 2009 and Choi *et al*., 2008). [11] ToMOH, toluene/*o*-xylene monooxygenase hydroxylase (data from references McCormick *et al*., 2006 and Murray *et al*., 2007). [12] ToMOH T201S, toluene/*o*-xylene monooxygenase hydroxylase variant (data from references Song *et al*., 2010 and Song & Lippard, 2011). [13] ADO, aldehyde-deformylating oxygenase (data from reference Pandelia *et al*., 2013).

Structural comparison of the diiron environment of other peroxo-diiron(III) enzymes with DOHH sheds light on the possible reasons for the extreme longevity of the peroxo-diiron(III) species in DOHH (hsDOHH and scDOHH) (Fig. 3.36). First, a histidine-rich ligand set (4H-2E) coordinates the diiron site; all histidines coordinate irons through their Nε atoms; both glutamate carboxylate groups terminally coordinate the irons in a monodentate fashion. All of these features give rise to weaker electron donor properties of the ligands. Studies with biomimetic complexes revealed that cleavage of the O-O bond is enhanced by introduction of more electron-donating, negatively charged ligands (Dong *et al.*, 1996). In contrast to DOHH, the diiron sites of sMMOH, RNR-R2, Δ^9D, and ferritin display a carboxylate-rich ligand set, histidines coordinating through their Nδ atoms, and at least one bridging carboxylate (Table 3.10; Fig. 3.36). Second, the peroxo unit in the peroxo-diiron(III) core of DOHH is shielded by a highly hydrophobic environment comprising the four hisitidines as well as the residue pairs Met86/Met237 and Leu53/Leu204. Such a unique hydrophobic ligation hemisphere does not exist in the other enzymes mentioned above. A correlation between the stability of the peroxo species and the hydrophobicity of its environment has been observed with small-molecule model-compounds. A *μ*-1,2-peroxo-diiron(III) model complex, in which the peroxo ligands are located in a hydrophobic pocket consisting of phenyl groups, shows significant thermal stability and reversible oxygenation (Ookubo *et al.*, 1996). In addition, such a hydrophobic environment for the peroxo unit avoids proton-triggered heterolytic O-O bond cleavage. A threonine residue in the secondary coordination sphere of the diiron sites of sMMOH, ToMOH, and Δ^9D has been found to be important for transferring protons to the peroxo unit (Wallar & Lipscomb, 1996; Bochevarov *et al*., 2011; Lee *et al*., 2013). It has been shown that this threonine accelerates the formation and decay rates of the peroxo intermediate of ToMOH (Song *et al*., 2010). The presumably corresponding position in DOHH is occupied by the methionine pair, Met86/Met237, which is

not a good candidate for mediating proton transfer.

The peroxo intermediate of *Plasmodium* DOHHs (pfDOHH and pvDOHH) is not as stable as that of hsDOHH and scDOHH, in particular the *μ*-1,2-peroxo-diiron(III) species since the intensity of blue color decrease faster than that of hsDOHH and scDOHH (Fig. 2.29). However, the loss of the blue color does not mean the breakdown of the peroxo species in *Plasmodium* DOHHs. Actually, the subsequent diiron species (ambiguous color, approximately brown) (Fig. 2.29) should remain in peroxo-bound state because the species is able to perform the enzymatic reaction (Frommholz *et al*. (2009) and Atemnkeng *et al*. (2013) showed that isolated recombinant *Plasmodium* DOHHs were active in the absence of a reduction system). Likely, for *Plasmodium* DOHHs, the initially formed *μ*-1,2-peroxo-diiron(III) species quickly converts to *μ*-1,1-peroxo-diiron(III) species; the latter is normally colorless or brown (Table 3.8). Compared to the diiron core of hsDOHH and scDOHH, there are two major changes in the diiron core of pvDOHH which probably facilitate the protonation and subsequent breakdown of the peroxo unit in pvDOHH. First, an additional glutamate (Glu76) is involved in iron coordination, whereas the corresponding glutamate residue in hsDOHH and scDOHH is located in the secondary coordination sphere of the diiron site (Fig. 3.31, 3.32). This additional glutamate ligand enhances the electron donor capability of the ligands in the diiron site of pvDOHH. Second, Tyr44 (a residue located in the surface of protein) in the outer sphere of the diiron site is hydrogen-bonded with Glu76, whereas the residue corresponding to Tyr44 in hsDOHH and scDOHH is a phenylalanine (Fig. 3.32). The hydrogen-bonded Tyr44 and Glu76 form a putative proton-transfer pathway, by which the protons are delivered from the exterior to the diiron site of pvDOHH (from Tyr44 to Glu76 to Fe2).

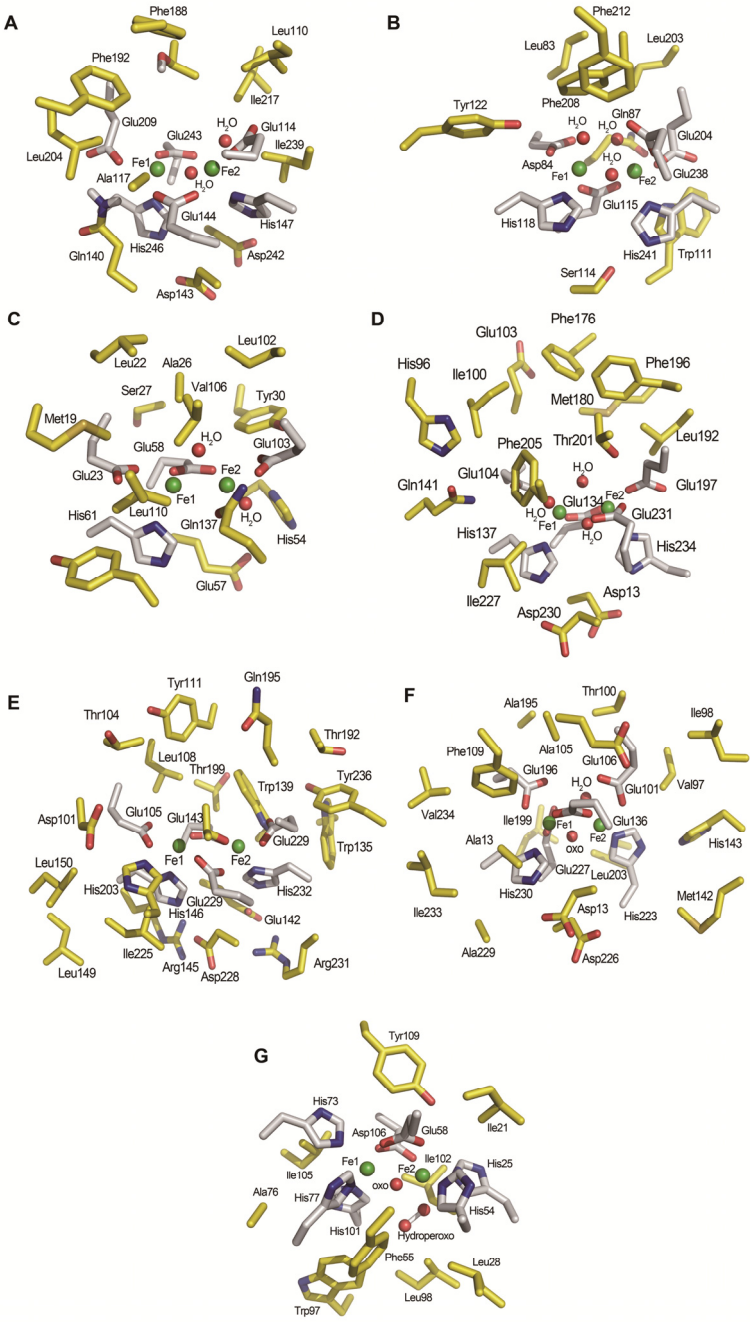

Fig. 3.36 Diiron site environments of non-heme diiron proteins. Carbon atoms in the primary and secondary coordination spheres are displayed in grey and yellow, respectively.

(A) *Methylococcus capsulatus* sMMOH (PDB code: 1MMO, Rosenzweig *et al.*, 1993).

(B) *E. coli* RNR-R2 wild type (PDB code: 1MXR, Högbom *et al.*, 2003).

(C) Bullfrog M ferritin (PDB code: 3RBC, Bertini *et al.*, 2012).

(D) *Pseudomonas stutzeri* ToMOH (PDB code: 2INC, McCormick *et al.*, 2006).

(E) *Ricinus communis* Δ^9D (PDB code: 1AFR, Lindqvist *et al.*, 1996).

(F) *Streptomyces thioluteus* AurF (PDB code: 3CHH, Choi *et al.*, 2008).

(G) *Themiste dyscritum* oxyHr (PDB code: 1HMO, Holmes *et al.*, 1991).

On the basis of these observations, it seems that the unique diiron environment in DOHH (hsDOHH and scDOHH) blocks the oxygen-activation sequence at the stage of the peroxo-diiron(III) species. This means that the catalytic core of DOHH has a very limited ability to break the O-O bond and generate a potent oxidant for C-H bond cleavage, in agreement with the observed, extremely low activity of hsDOHH *in vitro* (Vu *et al*., 2009). The decay of the peroxo-diiron(III) species in hsDOHH is accelerated in the presence of protein substrate (Vu *et al*., 2009), implying that incorporation of the Dhp side-chain into the diiron site facilitates the electron transfer. Vu *et al*. (2009) suggested that perhaps, a so-far unidentified interaction partner exists *in vivo* that assists the reaction. Alternatively, Nature perhaps chose such a slow enzyme to modulate the hypusination of eIF-5A, by which cell growth is strictly regulated (Hanauske-Abel *et al*., 1994).

Although the function of hemerythrin (Hr) is distinct from the O_2-activating non-heme diiron enzymes mentioned above, it is a good example for illustrating how a non-heme diiron protein can maintain the integrity of the O-O bond in the peroxo-diiron(III) unit. There are many similarities shared by the peroxo-diiron(III) cores of oxyHr and DOHH, although the peroxo group binds to the diiron core in different ways. The diiron unit of Hr is coordinated by five histidine ligands (through their Nε atoms) and two carboxylate groups (5H-E-D); the peroxo ion is surrounded by a hydrophobic environment consisting of two leucines, one isoleucine, one phenylalanine, and one tryptophan as well as four iron-coordinating histidines (Stenkamp, 1994), an environment similar to that in DOHH. These characteristics probably allow Hr to function as an O_2 carrier.

3.4.5 DOHH, an incomplete system

Peroxo intermediate is only one of the intermediate present in the reaction cycle of a non-heme diiron enzyme. It has been shown that the reaction cycle of sMMOH is constituted by a series of distinct intermediate (Wallar & Lipscomb, 1996; Kovaleva *et al*., 2007; Xue *et al*., 2008). As shown in Fig. 3.37, reduced form sMMOH (diiron(II)) (**H^{red}**) reacts with O_2 to yield a intermediate termed **O** (for oxygen adduct); then, peroxo intermediate (**P**) is formed resulting from the oxidation of irons; the peroxo unit in **P** experiences protonation and isomerization to yield a high-oxidation diiron species termed **Q**; abstract of a hydrogen from substrate (**RH**) by **Q** yields a radical adduct termed **R**; transfer of hydroxyl group to substrate yields a terminal adduct termed **T**; release of product (**ROH**) yields a resting species (**H^{ox}**); the reaction cycle is completed by the reduction of **H^{ox}** to **H^{red}**. The peroxo intermediate itself is able to oxidize electron-rich substrates (Tinberg & Lippard, 2010).

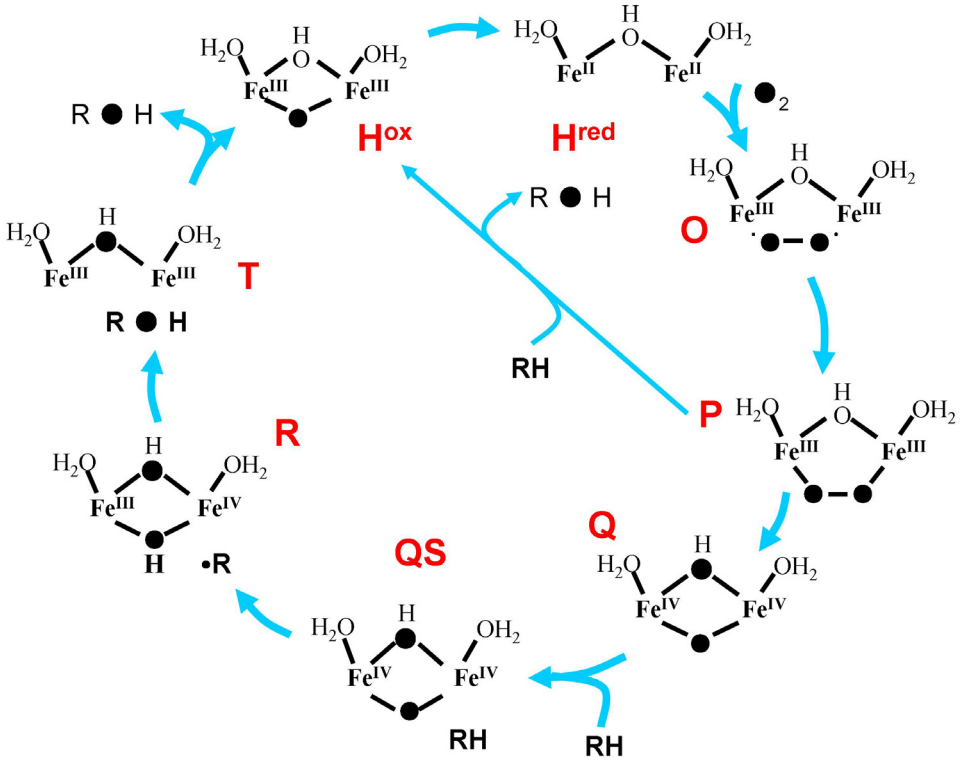

Fig.3.37 Intermediates in the reaction of sMMOH.

3.4.5.1 Resting state of DOHH

Normally, non-heme diiron enzymes are present in their resting state which possesses a *μ*-oxo/hydroxo-diiron(III) core (Fig. 3.37). The resting species is the most stable oxidation state of diiron enzymes. X-ray structures of diiron enzymes are normally determined for this species. The spectroscopic prosperities of the resting enzymes are summarized in Table. 3.11. The common spectroscopic features of this species are absence of absorption in the long-wavelength region in UV/Vis spectroscopy and a relatively small Mössbauer isomer shift (0.44 – 0.56 mm/s) (Table. 3.11). So far, the resting state of DOHH has not been detected. A yellowish hsDOHH observed after the reaction with Dhp-eIF-5A has been proposed to be the final diiron(III) species (Vu *et al.*, 2009); however, the system became cloudy after the reaction, so the structural properties of the yellowish hsDOHH remain to be characterized. In our glycerol complex structures (hsDOHH and scDOHH), the two iron atoms are bridged by a putative hydroxo group, which probably corresponds to the diiron core of DOHH in the resting state.

Table 3.11 Spectroscopic properties of resting state non-heme diiron proteins

	λ_{max}, nm (ε, M-1 cm-1)	Mössbauer	
		δ (mm/s)	ΔE_Q (mm/s)
sMMOH (*Mt*) [1]	282 [2]	0.51, 0.50 [3]	1.16, 0.87 [3]
sMMOH (*Mc*) [4]	280 [5]	0.50 [5]	1.05 [5]
RNR-R2 (act) [6]	325 (9400), 370 (7200), 412 (4100) [7]	0.53, 0.44 [8]	1.66, 2.45 [8]
RNR-R2 (met)	325 (9400), 370 (7200) [7]	0.53, 0.44 [8]	1.66, 2.45 [8]
H ferritin		0.50 [9]	1.30 [9]
Δ^9D	325, 355, 470 [10]	0.53 [10]	1.54 [10]
T4moH	282 [11]	1.51, 0.56 [11]	0.93, 1.55 [11]
AurF	360 [12]	0.54, 0.48 [12]	-1.86, 0.80 [12]
metHr	355 [13]	0.46 [14]	1.57 [14]

[1] *Methylosinus trichosporium* OB3b. [2] Fox *et al*., 1989. [3] Fox *et al*., 1993a. [4] *Methylococcus capsulatus* (Bath). [5] DeWitt *et al*., 1991. [6] Species with tyrosine radical. [7] Wallar & Lipscomb, 1996. [8] Atkin *et al*., 1973. [9] Bou-Abdallah *et al*., 2002. [10] Fox *et al*., 1993b. [11] Pikus *et al*., 1996. [12] Korboukh *et al*., 2009. [13] Dawson *et al*., 1972. [14] Okamura *et al*., 1969.

3.4.5.2 Reduction system for DOHH

The natural reaction cycle of non-heme diiron enzymes is generally initiated from the resting enzymes (Fig. 3.37). A specific reduction system adopted by enzymes reduces the *μ*-oxo/hydroxo-diiron(III) core to a diiron(II/II) cluster. Bacterial multicomponent monooxygenases, such as MMO, contain a reductase component (MMOR) which is responsible for the reduction (Solomon *et al.*, 2000). The enzymes lacking this reduction component normally utilize a physiological reduction system; for example, [2Fe-2S] ferredoxin / NADPH:ferredoxin oxidoreductase for Δ^9D (Solomon *et al*., 2000) and AurF (Choi *et al*., 2008). The reduction system for RNR-R2 is still controversial (Solomon *et al*., 2000). A physiological reduction system for DOHH has not been identified so far.

3.4.5.3 High-oxidation state diiron species of DOHH

On the electron transfer sequence of DOHH, the identity of the diiron species following peroxo-diiron(III) intermediate remains unclear. Generally, the fate of peroxo-diiron(III) species in O_2-activating non-heme diiron enzymes is cleavage of the O-O bond and then becoming a high-oxidation state diiron species such as diiron(IV/III) for RNR-R2 and diiron(IV) for sMMOH (Wallar & Lipscomb, 1996) (Fig. 3.37). These high-oxidation state diiron species are potent enough to cleave O/C-H bands (for RNR-R2 and sMMOH, resepctively) in the substrate. The spectroscopic features of the characterized high-oxidation state diiron species are summarized in Table 3.12. It is likely that DOHH shares a mechanism similar to that of sMMOH, since both of these enzymes catalyze the cleavage of a C-H bond and incorporation of a hydroxyl group into the hydrocarbon substrate. The high-oxidation state diiron species has not been detected in DOHH system.

Table 3.12 Spectroscopic properties of high-oxidation state diiron species

Protein	Diiron species	λ_{max}, nm (ε, M-1 cm-1)	Mössbauer		Exchange coupling J, cm^{-1}	Fe-Fe distance, Å
			δ, mm/s	ΔE_Q, mm/s		
sMMOH (*Mt*) [1]	diiron(IV) (Intermediate Q)	330 (7500), 430 (7500) [2]	0.17 [3]	0.53 [3]	> 60 [3]	2.46 [4]
sMMOH (*Mc*) [5]	diiron(IV) (Intermediate Q)	350, 420 [f]	0.21, 0.14 [6]	0.68, 0.55 [6]		
RNR-R2	diiron(III/IV) (Intermediate X)	360 [7]	0.26, 0.56 [8]	0.6, 0.9 [8]		2.78 [9]

[1] *Methylosinus trichosporium* OB3b. [2] Lee *et al*., 1993a. [3] Lee *et al*., 1993b. [4] Shu *et al*., 1997. [5] *Methylococcus capsulatus* (Bath). [6] Liu *et al*., 1995b. [7] Bollinger *et al*., 1991. [8] Sturgeon *et al*., 1996. [9] Dassama *et al*., 2013.

3.5 Structure of human eukaryotic translation initiation factor 5A-2

Although human eIF-5A isoforms, eIF-5A1 and eIF-5A2, share high amino-acid sequence identity (84%), these two isoforms were found to play distinct roles in cancerogenesis (Caraglia *et al*., 2013). In order to find a correlation between the functional and structural differences for human eIF-5A isoforms, the crystal structure of human eIF-5A2 was determined experimentally as a part of this work. Recombinant human eIF-5A2 production and preliminary structural analysis were presented in Janica Meine' s Bachelor thesis (2013).

3.5.1 Crystallization and structure determination

Crystallization of full-length of human eIF-5A2 was not successful. A truncated eIF-5A2 (eIF-5A2-T16, including residues 16 - 153) was crystallized under a condition consisting of 10% PEG1500 and 100 mM Bicine (pH 8.6). The structure of human eIF-5A2 was solved by molecular replacement using the N-terminal domain of eIF-5A1 (PDB code: 3CPF, Tong *et al*., 2009) as the search model (the full-length model did not give a solution). Table 3.13 shows a summary of crystallographic data collection and refinement.

Table 3.13 Crystallographic data and refinement statistics of human eIF-5A2

Diffraction data statistics	
X-ray source	P11, PETRAIII
Wavelength. Å	1.0000
Space group	$P2_12_12_1$
Unit cell parameters, Å, deg.	a = 90.19, b = 99.03, c = 152.96
Resolution range, Å	47.11 - 2.70
Reflections	249,306 (35,669)
Unique reflections	38,359 (5,531)
R_{merge} [1]	0.101 (0.872)
R_{pim} [2]	0.043 (0.369)
$CC_{1/2}$ [3]	0.998 (0.808)
$I/\sigma(I)$	12.6 (2.6)
Redundancy	6.5 (6.4)
Completeness, %	99.9 (100.0)
Wilson B factor, Å^2	50.5
Refinement statistics	
Refinement resolution, Å	19.97 - 2.70
No. reflections	36,307
R_{work}/R_{free} (% of refls.) [4]	0.217/0.247 (5.0)
Average B factor, Å^2	49.13
No. of atoms	
Protein	6,323
Water	11
R.m.s. deviations	
Bond lengths, Å	0.017
Bond angles, deg.	2.065
Ramachandran favored, %	98.1
Ramachandran outlier, %	0.2
Clashscore [5]	4.98
MolProbity score [5]	1.82

[1] $R_{merge} = \Sigma_{hkl}\Sigma_i|I_i(hkl) - \langle I_i(hkl)\rangle| / \Sigma_{hkl}\Sigma_i {}^{I_i(hkl)}$.

[2] Precision-indicating merging R factor. R_{pim} is defined as $\Sigma_{hkl}[1/(N-1)]^{1/2} \Sigma_i|I_i(hkl) - \langle I(hkl)\rangle| / \Sigma_{hkl}\Sigma_i {}^{I_i(hkl)}$, N is redundancy (Weiss & Hilgenfeld, 1997).

[3] Correlation coefficient between two random-half data sets (Karplus & Diederichs, 2012).

[4] $R_{work} = \sum_{hkl}|F_{obs} - F_{calc}| / \sum_{hkl}F_{obs}$. R_{free} serves as cross-validation of the R-factor. 5% of the reflections were set aside for the calculation of the free R-factor (Brünger, 1992).

[5] log-weighted combination of the clashscore, percentage of Ramachandran torsion angle not favored, and percentage of bad side-chain rotamers (Chen *et al.*, 2010).

3.5.2 Structure of human eIF-5A2

There are six copies of the human eIF-5A2 monomer constituting three eIF-5A2 dimers per asymmetric unit. The dimers are formed by swapping of the last β-strand in the C-terminal domain of the protein (Fig. 3.38). In the domain-swapped dimers, two eIF-5A2 molecules are arranged in an almost antiparallel manner, forming a butterfly-shaped structure with N- and C-terminal domains of the protein as the wings and body of "butterfly", respectively (Fig. 3.38). The dimer interface area is ~ 1600 $Å^2$.

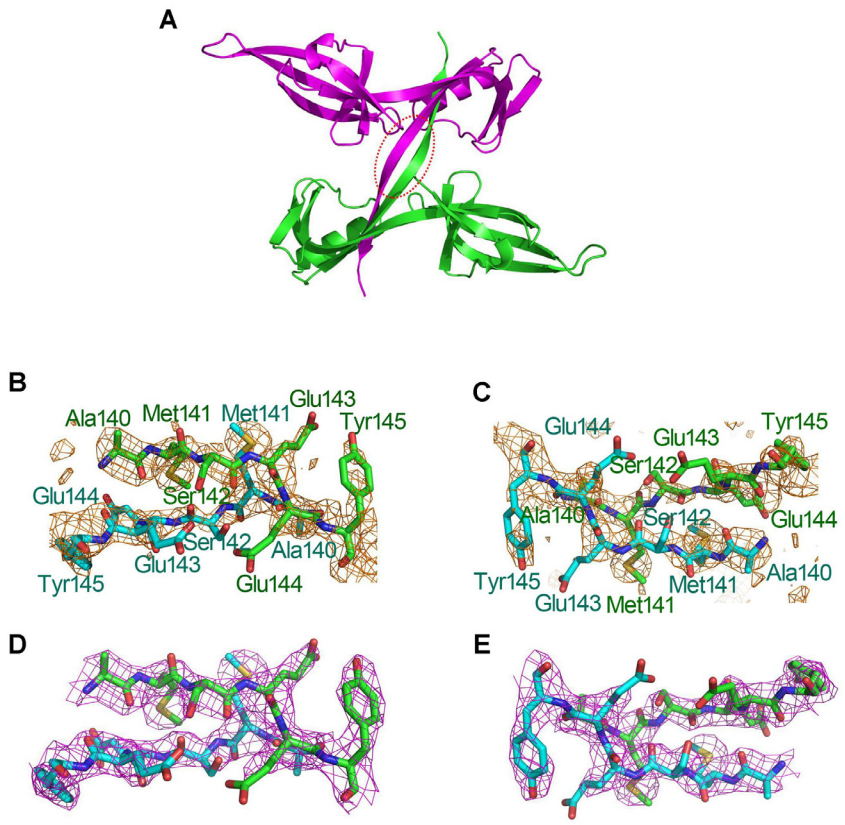

Fig. 3.38 The domain-swapped human eIF-5A2 dimer.
(A) Cartoon presentation of the domain-swapped eIF-5A2 dimer. The red ellipse indicates the hinge region (residues 140 – 145) of the domain-swapped eIF-5A2 dimer.
(B) Omit map (brown mesh: F_o-F_c, map, at 3.0 σ) of the hinge region.
(C) As for (B), another view.
(D) Electron density map (magenta mesh: $2F_o$-F_c, at 1.5 σ) of the hinge region after modeling of residues 140 – 145.
(E) As for (D), another view.

The monomeric structure of the human eIF-5A2 is similar to the reported crystal structures of eIF-5A1 (PDB code: 3CPF, Tong *et al*., 2009). It is composed of two predominantly β-sheet domains (Fig. 3.39 A). The structures of human eIF-5A2 and eIF-5A1 monomer can be superimposed with an Cα r.m.s. difference of about 1.36 Å (Fig. 3.39 B). In the structure of eIF-5A1, β6/β7 and β10/β11 are merged into two long β-strands (β6 and β9, respectively) in the structure of eIF-5A2 (Fig. 3.39 A & B). The variable residues between the human eIF-5A isoforms are mainly located in the C-terminal domain (Fig. 3.39 C & D). There are three exposed non-conserved residues in the C-terminal α-helix (changed from eIF-5A1 to eIF-5A2: Q125G, D128N, and C129A) (Fig. 3.39 C). The lysine residue (Lys50) to be modified to Hpu is located on the tip of an exposed loop linking β3 and β4 (Fig. 3.39 A). The loops disordered in the structure of eIF-5A1 (PDB code: 3CPF, Tong *et al*., 2009) are clearly observed in five of the six copies of the molecule in the structure of eIF-5A2.

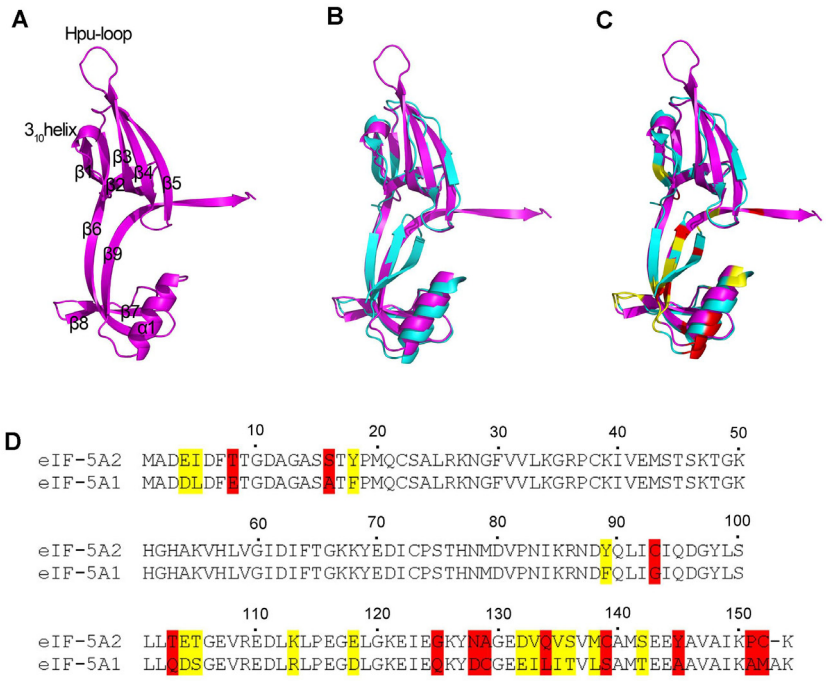

Fig. 3.39 Structural comparison of the human eIF-5A1 and eIF-5A2 monomers.
(A) Structure of the human eIF-5A2 monomer. Secondary structure elements are labeled.
(B) Structural alignment of human eIF-5A2 and eIF-5A1. The hypusine-containing loop is disordered in the structure of human eIF-5A1. Magenta: eIF-5A2; cyan: eIF-5A1 (PDB code: 3CPF, Tong *et al*., 2009).
(C) As for (B), the variable residues between the two human eIF-5A isoforms are displayed in different colors. Red: non-conservative alterations; yellow: conservative alterations.
(D) Amino-acid sequence alignment of human eIF-5A2 and eIF-5A1. Non-conservative and conservative changes are shown in red and yellow, respectively.

3.5.3 Comparison of dimeric eIF-5A2 and eIF-5A1

So far, all studies of eIF-5A suggested that the protein is present as a dimer in solution (Chung *et al*., 1991; Gentz *et al*., 2009; Dias *et al*., 2013). However, the dimerization pattern of eIF-5A remains unclear. The structure of human eIF-5A2 presented in this work shows a domain-swapped eIF-5A dimer (Fig. 3.40 A) which has not been found for eIF-5A from any other species. However, the butterfly-shaped eIF-5A dimer can be seen in the crystal structure of

human eIF-5A1 (PDB code: 3CPF, Tong *et al*., 2009) although domain-swapping does not occur in this structure (Fig. 3.40 B). In butterfly-shaped eIF-5A1 dimer, the distance between eIF-5A1 monomers is more close to one another giving rise to even more comprehensive intermolecular interaction and smaller overall dimer dimension compared to the domain-swapped eIF-5A2 dimer (Fig. 3.40 C). However, the dimer interface of eIF-5A1 (~ 930 $Å^2$) is still smaller than that of the domain-swapped eIF-5A2 dimer (~ 1600 $Å^2$). Both of the butterfly-shaped dimers (eIF-5A1 and eIF-5A2) resemble EF-P in shape (“L”), size, and surface electric potential (Fig. 3.38 D – F). The butterfly-shaped eIF-5A dimer is found in both crystal structures of the human isoforms implying that this dimerization pattern is biologically relevant.

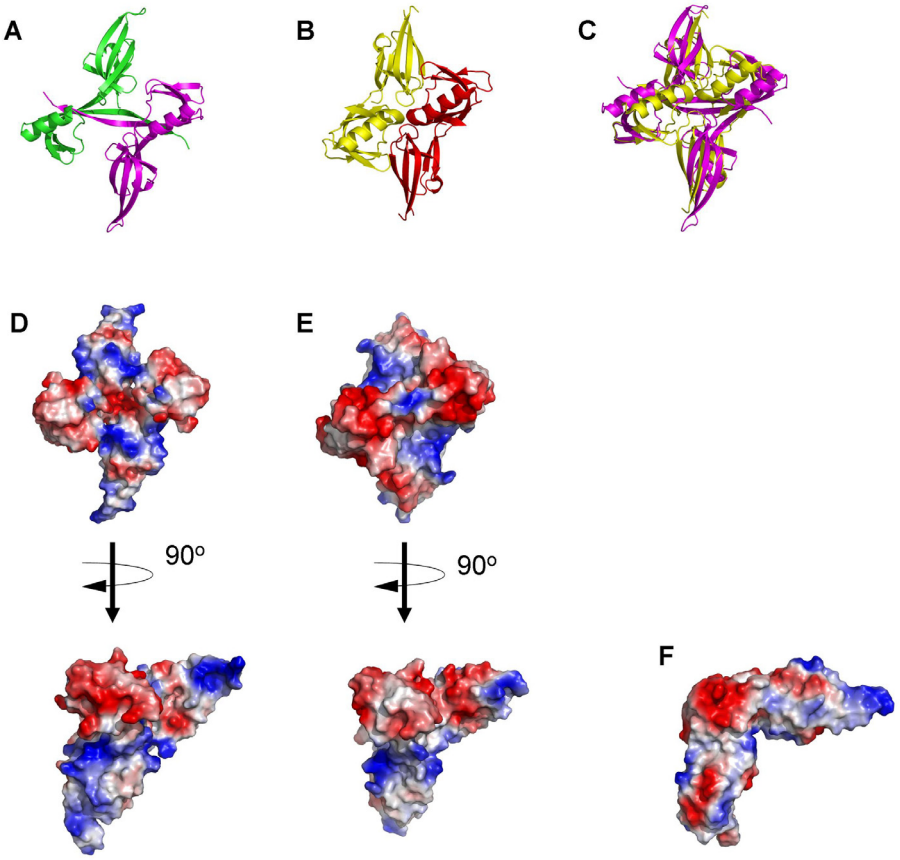

Fig. 3.40 Structural comparison of dimeric human eIF-5A2 and eIF-5A1.
(A) Structure of dimeric human eIF-5A2 (this work).
(B) Structure of dimeric human eIF-5A1 (PDB code: 3CPF, Tong *et al*., 2009).
(C) Superposition of dimeric human eIF-5A2 and eIF-5A1.
(D) Surface electrostatics of the human eIF-5A2 dimer, colored from red (negative potential) to blue (positive potential).
(E) As in (D), for the eIF-5A1 dimer.
(F) Surface electrostatics of *Thermus thermophilus* EF-P (PDB code: 1UEB; Hanawa-Suetsugu *et al*., 2004).

According to the destabilization-compensation hypothesis for protein domain-swapping (Ding *et al*., 2006), there are two possible reasons for the occurrence of domain-swapping in human eIF-5A2. First, the majority of variable residues difference between eIF-5A1 to eIF-5A2 are located in their C-terminal domains, in particular in the last two β-strands (Fig. 3.39). The changed residues in eIF-5A2 probably give rise to perturbation of the non-swapped topology of eIF-5A1 and the swap of last β-strand is a kind of compensation to stabilize the structure of eIF-5A2. Second, human eIF-5A1

and eIF-5A2 were crystallized under distinct pH conditions, pH 5.5 for eIF-5A1 (Tong *et al*., 2009) and pH 8.6 for eIF-5A2. The high pH condition possibly creates a destabilizing environment triggering domain-swapping in the eIF-5A2 dimer.

3.5.4 Comparison with other dimeric forms of eIF-5A derived from crystal structures

Dimeric forms of eIF-5A were also found in crystal structures of eIF-5A from *Arabidopsis thaliana* (PDB code: 3HKS, Teng *et al*., 2009) and *Methanococcus jannaschii* (PDB code: 1EIF, Kim *et al*., 1998) as shown in Fig. 3.41. In the *Arabidopsis thaliana* eIF-5A dimer, two copies of the eIF-5A monomer are arranged in parallel and stabilized by the interaction of β1 and the C-terminal inter-sheet loop of one molecule with the same β-sheet and loop of the other molecule (Fig. 3.41 A). The dimerization pattern of eIF-5A found in *Methanococcus jannaschii* is unique. Two eIF-5A monomers are dimerized through the hydrogen-bonded antiparallel β3 strand from each of the two molecules (Fig. 3.41 B).

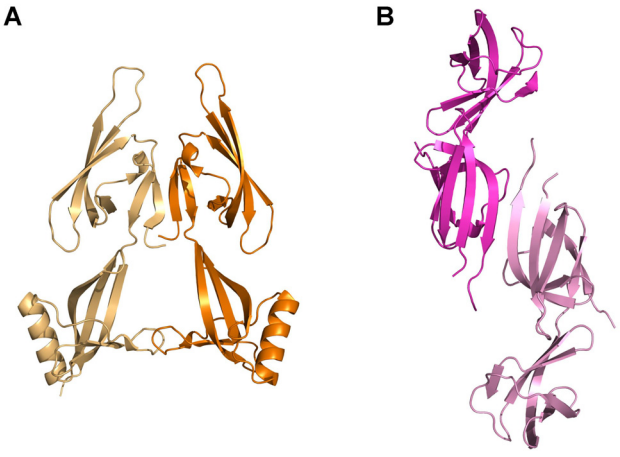

Fig. 3.41 Dimeric eIF-5A from other species.
(A) *Arabidopsis thaliana* eIF-5A dimer (PDB code: 3HKS, Teng *et al*., 2009).
(B) *Methanococcus jannaschii* eIF-5A (aIF-5A) dimer (PDB code: 1EIF, Kim *et al*., 1998).

Compared to the butterfly-shaped human eIF-5A dimer, the dimer interfaces in

these two structures are rather small (~ 570 Å^2), suggesting that association in these two dimers is very weak. In addition, in both of these two types of eIF-5A dimer, the hypusination sites (exposed loop in the N-terminal domain) are too close to each other or to the protein backbone, thereby hampering the interaction between eIF-5A precursor and DHS (or DOHH), as well as the biological functions of the Hpu residue in translation (insert into PTC on the ribosome, see Chapter 1) (Gutierrez *et al*., 2013). In the butterfly-shaped human eIF-5A dimer, both hypusination sites as well as the entire N-terminal domains are exposed.

3.5.5 Gel filtration analysis of recombinant human eIF-5A2 and eIF-5A1

In gel filtration chromatography, both recombinant human eIF-5A2 and eIF-5A1 (theoretical molecular mass of both isoforms: ~ 17.2 kDa) eluted slightly earlier than the 25 kDa standard protein (Fig. 3.42), consistent with an estimated molecular mass of ~ 26 kDa for the native human eIF-5A from red blood cells by using gel filtration (Chung *et al*., 1991). The ~ 26 kDa eIF-5A from human blood cells turned out to be the dimeric form of the protein by using analytical ultracentrifugatlon (~ 34.1 kDa) (Chung *et al*., 1991). Therefore, the recombinant human eIF-5A2 and eIF-5A1 likely also exist as a dimer in solution. In addition, the elution volume of human eIF-5A2 is smaller than that of eIF-5A1 (Fig. 3.42) indicating that the overall size of eIF-5A2 dimer is larger than that of eIF-5A1 dimer, in agreement with the more compact butterfly-shaped eIF-5A1 dimer observed in crystal structures (Fig. 3.41 B).

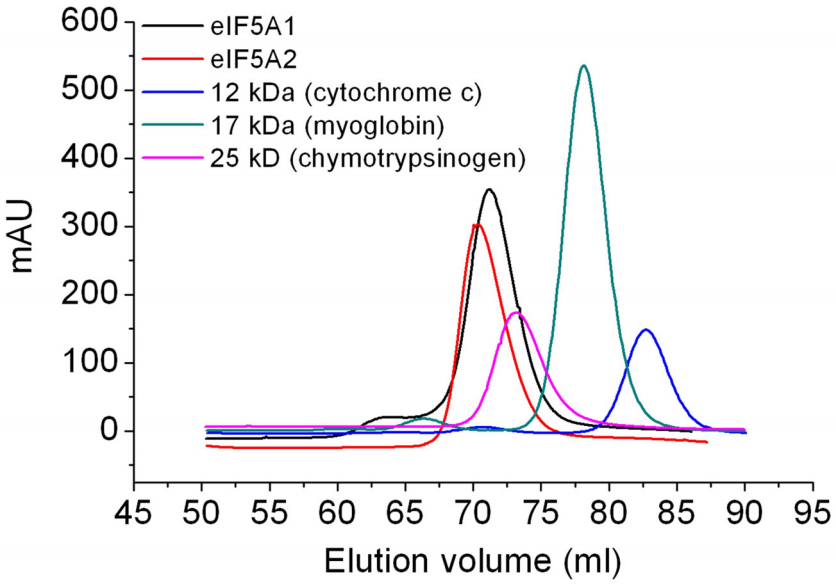

Fig. 3.42 Size-exclusion chromatography of human eIF-5A1, eIF-5A2, and molecular mass standard proteins.

Two recent studies showed that yeast eIF-5A is also present as a dimer by using size-exclusion chromatography and the dimerization is RNA-dependent. However, there were several critical conflicts between these two studies concerning the other requirements for dimerization, such as hypusination and intermolecular disulfide bond formation (Gentz *et al*., 2009; Dias *et al*., 2013). In the present work, recombinant human eIF-5A2 and eIF-5A1 treated with RNase A did not show any change of the gel filtration profiles compared to the untreated proteins suggesting that the binding of RNA is not essential for human eIF-5A dimerization (data not shown).

3.5.6 Biological implications of the human eIF-5A dimer

eIF-5A and its prokaryotic homolog, EF-P, were found to be essential in translation elongation (Saini *et al.*, 2009), in particular of polyproline stretches (Gutierrez *et al.*, 2013, Rossi *et al.*, 2014). The crystal structure of EF-P – ribosome complex revealed that EF-P binds to both subunits of the ribosome (30S and 50S subunits) through its domain I (in the N-terminal domain) and domain III (in the C-terminal domain) interacting with acceptor stem and

anticodon loop of peptidyl-tRNA in the P-site, respectively (Blaha *et al*., 2009). Compared with EF-P, domain III is absent in eIF-5A; therefore, the question rises how the absence of the domain III is complemented for. Dimerization should be the simplest way for the eIF-5A monomer to acquire a size comparable to that of EF-P. The butterfly-shaped human eIF-5A dimer (isoform 1 and 2) is the most stable and reasonable dimerization pattern found in many crystal structures. More importantly, it mimics EF-P in shape and size. Compared to the human eIF-5A1 dimer, the eIF-5A2 dimer displays a larger molecular size owning to domain-swapping. This may be alter the function of eIF-5A2 as a steric modulator in translation. Furthermore, it is possible that translational control of human eIF-5A isoforms results in distinct roles for the two isoforms in cancerogenesis.

3.6 Purification and crystallization of the human DHS – eIF-5A complex

3.6.1 Protein production

Although around 90% of recombinant DHS was insoluble, a considerable amount of soluble protein could be isolated from a large-scale expression culture (8 L culture) (Fig. 3.43 A). Recombinant eIF-5A1 displayed a band larger than its theoretical molecular mass (17.2 kDa) in SDS-PAGE (Fig. 3.43 B). The N-terminal domain of eIF-5A1 (residues 1 – 83) (eIF-5A1-N) was purified in order to increase the chance to crystallize DHS in complex with substrate (Fig. 3.43 C) since N-terminal domain of eIF-5A directly interacts with DHS (Joe & Park, 1994).

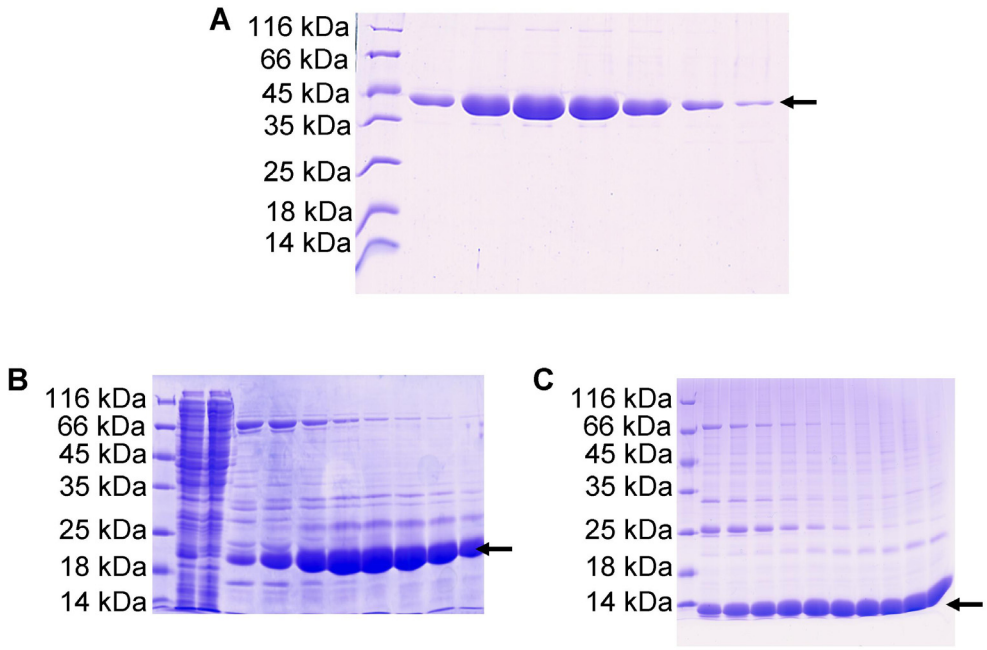

Fig. 3.43 Purification of DHS, eIF-5A, and N-terminal domain of eIF-5A. The bands corresponding to the recombinant proteins are indicated by arrows.
(A) SDS-PAGE analysis of DHS (41.3 kDa).
(B) SDS-PAGE analysis of eIF-5A (17.2 kDa).
(C) SDS-PAGE analysis of N-terminal domain of eIF-5A1 (eIF-5A1-N) (8.0 kDa).

3.6.2 The formation of the enzyme – substrate complex

Complex formation between DHS and eIF-5A was investigated by a gel mobility-shift method reported by Lee *et al*. (1999). In native electrophoresis,

the band corresponding to the DHS – eIF-5A complex migrate slower than the band of free DHS (Lee *et al*., 1999). The same amount of recombinant DHS incubated with varying amounts of eIF-5A1 and the formation of the enzyme – substrate complex was detected by native PAGE. As shown in Fig. 3.44, in the mixture of DHS and eIF-5A1 at a molar ratio of 1:1 (DHS tetramer to eIF-5A1 monomer), about half of the DHS was bound to eIF-5A1 and the other half of DHS was free. No free DHS and eIF-5A1 could be detected by native PAGE when the ratio of the two proteins in the mixture was 1:2. Free eIF-5A1 was detected when the proportion of eIF-5A1 in the mixture was further increased (Fig. 3.44). These observations indicate that the binding stoichiometry of DHS and eIF-5A1 in the complex is one DHS tetramer to two eIF-5A1 monomers. This binding ratio is not in agreement with the observation (1:1) reported by Lee *et al*. (1999) by using quantitative N-terminal sequencing. Considering that eIF-5A1 exists as a dimer, a 1:2 interaction model (one DHS tetramer to one eIF-5A1 dimer) is preferred in this work.

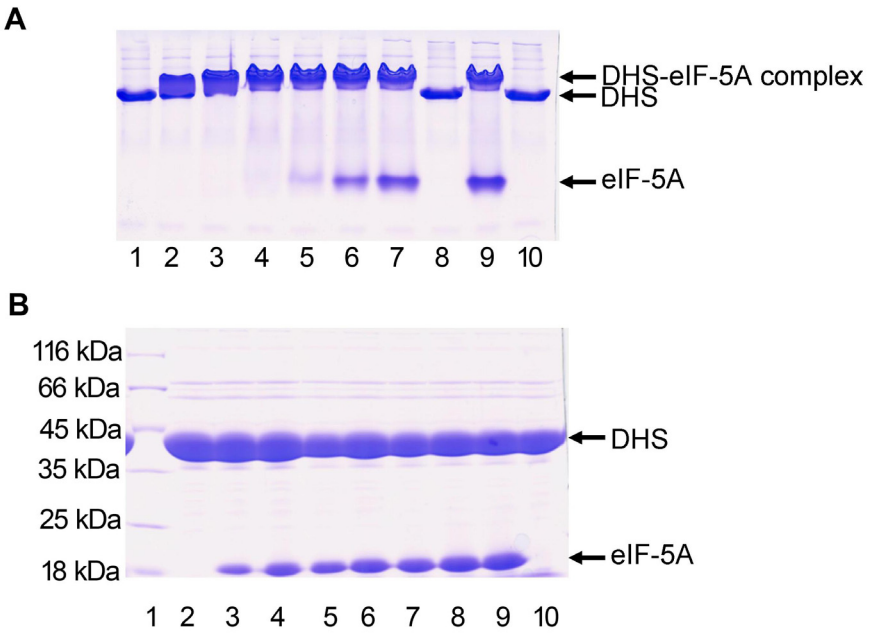

Fig. 3.44 Determination of the binding stoichiometry of DHS and eIF-5A1 in the enzyme – substrate complex.
(A) Native PAGE analysis of the mixtures of DHS and varying amounts eIF-5A1. Lane 1: DHS alone; lane 2: 1:1 ratio (molar ratio of DHS tetramer and eIF-5A1 monomer); lane 3: 1:1.5 ratio; lane 4: 1:2 ratio; lane 5: 1:2.5 ratio; lane 6: 1:3 ratio; lane 7: 1:3.5 ratio; lane 8: DHS alone; lane 9: 1:4 ratio; lane 10: DHS alone.
(B) SDS-PAGE analysis of the same samples in (A). Lane 1: protein marker; lane 2: DHS alone; lane 3: 1:1 ratio; lane 4: 1:1.5 ratio; lane 5: 1:2 ratio; lane 6: 1:2.5 ratio; lane 7: 1:3 ratio; lane 8: 1:3.5 ratio; lane 9: 1:4 ratio; lane 10: DHS alone.

Complex formation between DHS and eIF-5A1-N was investigated by native electrophoresis as well. However, the mixtures of DHS and eIF-5A1-N had a tendency to precipitate (slightly cloudy) before loaded to the PAGE gel and displayed a diffuse band in native PAGE (Fig. 3.45), suggesting that the DHS – eIF-5A1-N complex is not as stable as DHS in complex with full-length eIF-5A1. The observation implied that the C-terminal domain of eIF-5A1 also plays an important role in enzyme – substrate interaction.

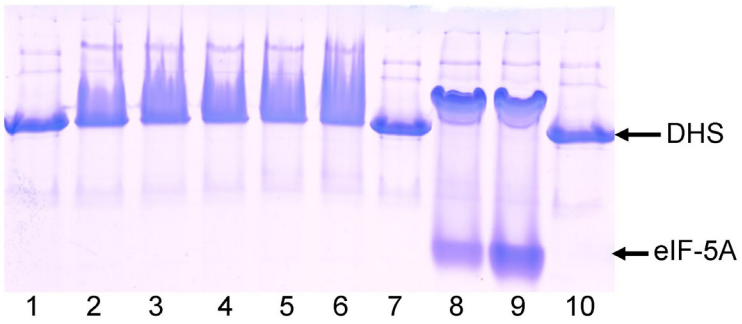

Fig. 3.45 Native electrophoresis analysis of complex formation between DHS and eIF-5A1-N. Lane 1: DHS alone; lanes 2 – 6: mixtures of DHS and varying amounts of eIF-5A1-N; lane 7: DHS alone; lane 8 and 9: mixtures of DHS and varying amounts of full-length eIF-5A1; lane 10: DHS alone.

3.6.3 Purification of the DHS - eIF-5A1 complex

A mixture of DHS and excessive amount of eIF-5A (at a ratio of one DHS tetramer to four eIF-5A1 monomers) was purified by size-exclusion chromatography (Fig. 3.46 A). SDS-PAGE analysis of the chromatographic fractions indicated that the main peak, which eluted early, corresponded to the DHS - eIF-5A1 complex and a small peak that eluted later was surplus eIF-5A1 (Fig. 3.46 A & B). In the native electrophoresis, the fractions containing DHS - eIF-5A complex displayed an obvious mobility-shift compared to DHS alone, indicating that the enzyme – substrate complex was successfully purified (Fig. 3.46 A, lower PAGE gel).

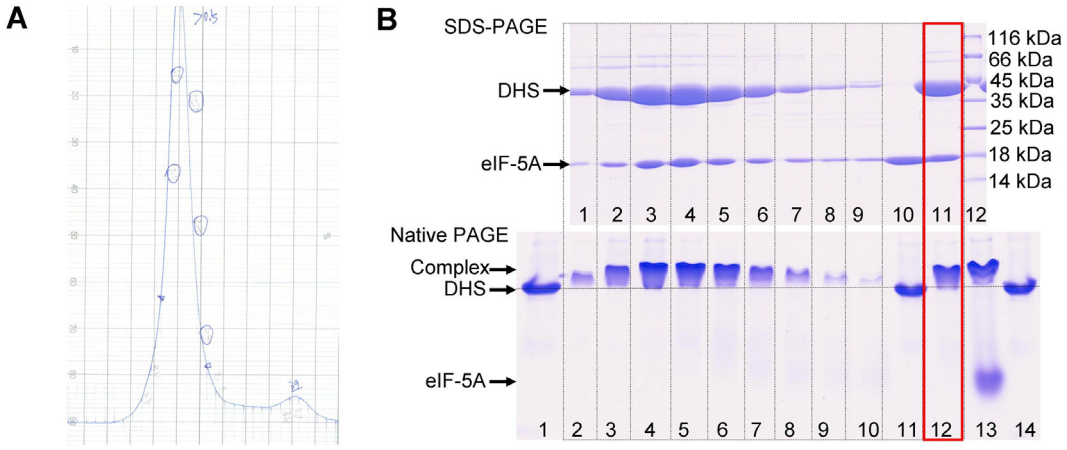

Fig. 3.46 Purification of the DHS - eIF-5A1 complex.
(A) Elution profile of a mixture of DHS and excessive eIF-5A1.
(B) SDS-PAGE (top) and native PAGE (bottom) analysis of chromatographic fractions of the gel filtration. In the top PAGE gel, lanes 1 – 9: main peak fractions in (A); lane 10: small peak fraction in (A); lane 11: pooled fractions of lanes 1 – 9; lane 12: protein marker. In the bottom PAGE gel, lane 1: DHS alone; lanes 2 – 10: corresponding to lanes 1 – 9 in the top PAGE gel; lane 11: DHS alone; lane 12: corresponding to lane 11 in the topr PAGE gel; lane 13: mixture of DHS and excessive eIF-5A1 before gel filtration; lane 14: DHS alone. The final purified DHS - eIF-5A1 complex is indicated by a red rectangular box.

3.6.4 Crystallization of the DHS – eIF-5A1 complex

Crystallization screening was performed by using three different preparations of the DHS – eIF-5A1 complex: complex purified by gel filtration, mixture of DHS and eIF-5A at a molar ratio of 1:2 (one DHS tetramer per two eIF-5A1 monomers), and mixture of DHS and eIF-5A1-N at a molar ratio of 1:2 (one DHS tetramer per two eIF-5A1-N monomers). Unexpectedly, in a large number of crystallization conditions, crystals were observed (Table 3.14). Five representative conditions (distinct pH or precipitants) were selected for crystal optimization and structure determination (Fig. 3.47). Unfortunately, the crystals growing from two conditions turned out to be free-DHS crystals after the structures were determined (Table 3.14). Structures of crystals growing from the other three conditions cannot be determined due to the poor quality of the diffraction data (not be processible) or poor diffraction (~ 9 Å) (Table 3.14).

Table 3.14 Conditions obtained from crystallization screening for the DHS – eIF-5A1 complex

Complex	Crystallization condition	Structure[1]
Purified DHS – eIF-5A1 complex [2]	4.0 M potassium formate, 0.1 M Bis-Tris propane (pH 9.0), 2% PEG 2000 MME	~ 2.10 Å, structure was solved, free DHS
	10% 2-propanol, 0.1 M HEPES sodium-salt (pH 7.5), 20% PEG 4000	~ 2.60 Å, structure was solved, free DHS
	20% 2-propanol, 0.1 M sodium citrate (pH 5.6), 20% PEG 4000	~ 2.90 Å, structure was not solved (data cannot be processed)
	0.2 M $(NH_4)_2SO_4$, 0.1 M Tris (pH 7.5), 20% PEG 5000 MME	
	0.1 M sodium cacodylate (pH 6.5), 1.4 M NaOAc	
	0.5 M $(NH_4)_2SO_4$, 0.1 M HEPES (pH 7.5), 30% MPD	
	0.1 M HEPES sodium-salt (pH 7.5), 1.5 M Li_2SO_4	
	0.1 M Tris (pH 8.5), 2.0 M $NH_4H_2PO_4$	
	0.5 M NaCl, 0.1 M sodium citrate (pH 5.6), 2% polyethylene imine	
	0.01 M $NiCl_2$, 0.1 M Tris (pH 8.5), 1.0 M Li_2SO_4	
	0.1 M Tris (pH 8.5), 25% tert-butanol	
	0.2 M $MgCl_2$, 0.1 M Tris (pH 8.5), 3.4 M 1,6-hexanediol	
	1.8 M $(NH_4)_2SO_4$, 0.1 M Bis-Tris (pH 6.5), 2% PEG 550 MME	
Mixture of DHS and eIF-5A1 [3]	4.0 M potassium formate, 0.1 M Bis-Tris propane (pH 9.0), 2% PEG 2000 MME	~ 2.10 Å, structure was solved, free DHS
	0.1 M HEPES sodium-salt (pH 7.5), 2% PEG 400, 2.0 M $(NH_4)_2SO_4$	~ 2.90 Å, structure was not solved (data cannot be processed)
	0.1 M Tris (pH 8.5), 20% ethanol	
	15% 2-propanol, 0.1 M sodium citrate (pH 5.0), 10% PEG 10,000	
	18% v/v 2-propanol, 0.1 M sodium citrate (pH 5.5), 20% PEG 4000	
Mixture of DHS – eIF-5A1-N [4]	10% ethanol or 20 mM NaCl, 10 mM Tris (pH 8.8); 30% glycerol	Complex crystals, ~ 9 Å, structure was not solved

[1] Crystals were optimized and the structures were solved.

[2] DHS – eIF-5A1 complex was purified by gel filtration.

[3] DHS and eIF-5A1 were mixed at a molar ratio of one DHS tetramer to two eIF-5A1 monomers.

[4] DHS and eIF-5A1-N were mixed at a ratio of one DHS tetramer to two eIF-5A1-N monomers.

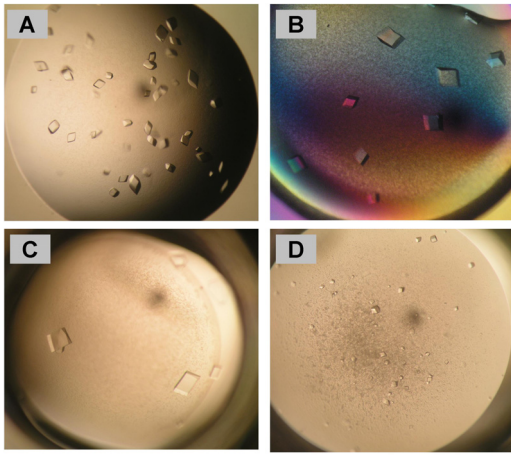

Fig. 3.47 Selected crystallization conditions and optimized crystals.
(A) Crystals grew under 4.0 M potassium formate, 0.1 M Bis-Tris propane (pH 9.0), and 2% PEG 2000 MME.
(B) Crystals grew under 10% 2-propanol, 0.1 M HEPES sodium-salt (pH 7.5), and 20% PEG 4000.
(C) Crystals grew under 20% 2-propanol, 0.1 M sodium citrate (pH 5.6), and 20% PEG 4000.
(D) Crystals grew under 0.1 M HEPES sodium-salt (pH 7.5), 2% PEG 400, and 2.0 M $(NH_4)_2SO_4$.

The crystals growing from the mixture of DHS and eIF-5A1-N were extensively optimized. The 10% ethanol in the initial crystallization condition (Table 3.14) was found to be not essential. The crystals were reproduced in low ionic-strength (less than 50 mM NaCl) and at high pH (~ 8.8) condition (Fig. 3.48 A). Big crystals were obtained by adding up to 35% glycerol (Fig. 3.48 B). The protein sample prepared from well-washed crystals displayed two expected bands in the SDS-PAGE that corresponded to DHS (41.2 kDa) and eIF-5A1-N (8.0 kDa), respectively (Fig. 3.48 C), indicating that the obtained crystals contained the DHS – eIF-5A1-N complex. Further evidence for the protein complex came from a fluorescent probe (carboxyrhodamine, Molecular Dimensions). When 10% of eIF-5A1-N was covalently labeled with fluorescent probe, the crystals of the complex could be stained under fluorescent conditions (Fig. 3.48 D). The crystals of the DHS – eIF-5A1-N complex diffracted up to 9 Å at synchrotron beamline (Fig. 3.49). Even if a high-pressure freezing system was applied (assisted by Dr. Anja Burkhardt,

P11, DESY), the diffraction could not be improved.

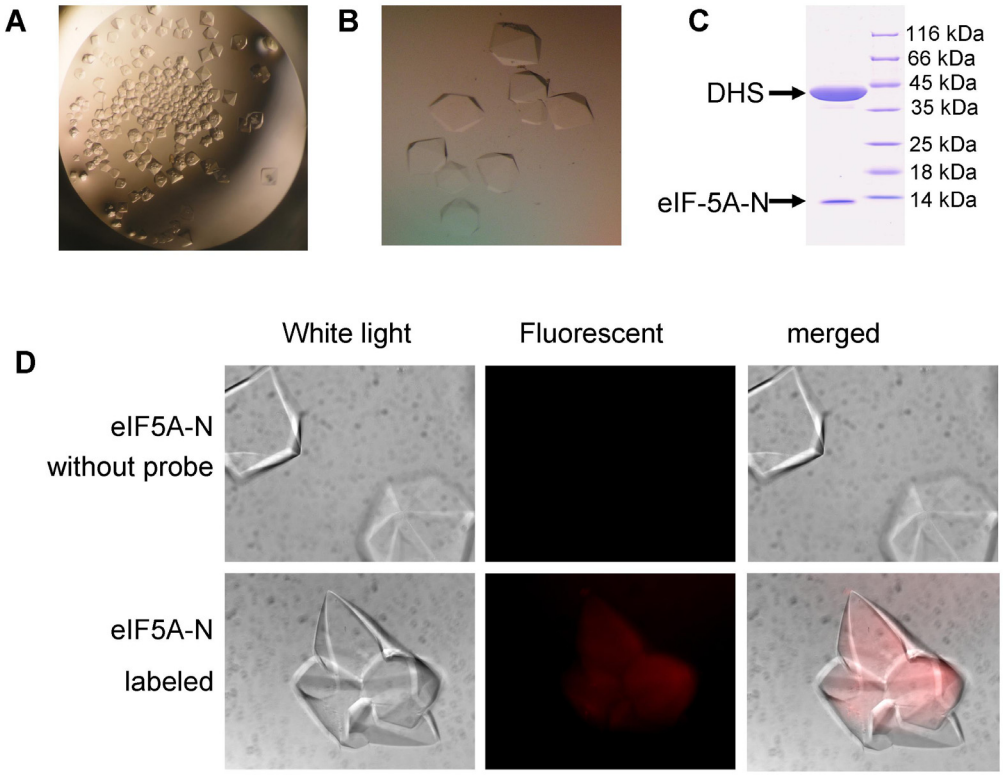

Fig. 3.48 Crystals of the DHS – eIF-5A1-N complex.
(A) Crystals of the DHS – eIF-5A1-N complex grown at low ionic-strength (less than 50 mM NaCl) and high pH (~8.8).
(B) Crystals of the DHS – eIF-5A1-N complex grown under a condition based on (A) with 35% glycerol.
(C) SDS-PAGE analysis of denatured crystal material (well-washed crystals were dissolved in a buffer containing 2% SDS).
(D) Images of the native (upper panel) and fluorescent-labeled (lower panel) complex crystals under white (left panel) and fluorescent (middle panel), and the merged light (right panel).

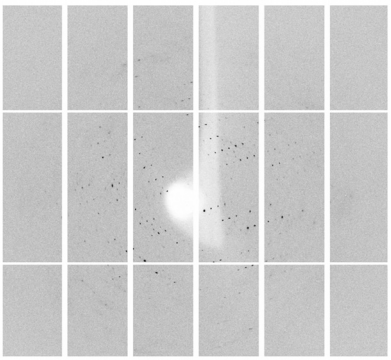

Fig. 3.49 Diffraction image of a DHS – eIF-5A1-N complex crystal.

Although the structure of the DHS – eIF-5A1-N complex could not be solved due to the poor diffraction, the successful crystallization of the complex was already a big progress after many efforts. The subsequent work should focus on improving diffraction of the crystals.

4. Summary

Hypusine is a natural amino acid discovered first in bovine brain in 1971. It is only found in eukaryotic translation initiation factor 5A (eIF-5A). Subsequent studies revealed that hypusine is afforded by a two-step posttranslational modification (termed hypusination) of the eIF-5A precursor, which is catalyzed by deoxyhypusine synthase (DHS) and deoxyhypusine hydroxylase (DOHH). In the past 45 years, the essential roles of eIF-5A and hypusine have been extensively characterized. The present understanding of eIF-5A is that the protein functions as a steric modulator or adaptor in the synthesis of polyproline-containing proteins at ribosomes and in the nuclear export of certain mRNAs such as unspliced HIV RNA and mRNA encoding inducible nitric oxide synthase. Hypusination of eIF-5A is essential for these functions. Therefore, both the enzymes DHS and DOHH are considered interesting targets for the design of novel inhibitors for the therapy of HIV infection and diabetes.

In addition, there are two eIF-5A isoforms (eIF-5A1 and eIF-5A2) present in man. The genes encoding the two are located in different regions of the genome and their protein products play distinct roles in tumorigenesis. eIF-5A2 is proposed to be an oncoprotein. So far, the structures of human eIF-5A1 and of DHS have been determined. However, the structures of eIF-5A2, DOHH, and the DHS-eIF-5A complex have not been elucidated.

By using X-ray crystallography and spectroscopic techniques, the present study aims at providing structural information on the proteins involved in the hypusination pathway. First, crystal structures of DOHH from man, yeast, and *Plasmodium vivax* are presented. For human DOHH, two crystal structures that correspond to two states of the enzyme, the peroxo intermediate (POX) and a complex of the diiron core with glycerol (GLC), are determined at high resolution. The POX structure constitutes the first visualization of a native

μ-1,2-peroxo intermediate of a diiron enzyme and is therefore guaranteed to raise the interest of the large communities of metalloenzyme researchers and bioinorganic chemists. The structures of human DOHH explain the extreme longevity of the peroxo intermediate present in this enzyme. Furthermore, the structures of DOHH illustrate the specific interaction between DOHH and its only protein substrate, deoxyhypusine-eIF-5A.

Second, the structure of human eIF-5A2 shows a novel dimerization pattern of the protein (domain swapping) which is proposed to be biologically relevant. Finally, the DHS-eIF-5A complex is successfully crystallized. The results presented in this thesis contribute to a better understanding of hypusination in eukaryotes.

5. References

Abbruzzese, A. (1988): Developmental pattern for deoxyhypusine hydroxylase in rat brain. *J. Neurochem.* **50**, 695-699.

Abbruzzese, A., Park, M.H. & Folk, J.E. (1986): Deoxyhypusine hydroxylase from rat testis. Partial purification and characterization. *J. Biol. Chem*. **261**, 3085-3089.

Abbruzzese, A., Park, M.H., Beninati, S. & Folk, J.E. (1989): Inhibition of deoxyhypusine hydroxylase by polyamines and by a deoxyhypusine peptide. *Biochim. Biophys. Acta* **997**, 248-255.

Abbruzzese, A., Hanauske-Abel, H.M., Park, M.H., Henke, S. & Folk, J.E. (1991): The active site of deoxyhypusyl hydroxylase: Use of catecholpeptides and their component chelator and peptide moieties as molecular probes. *Biochim. Biophys. Acta* **1077**, 159-166.

Andrade, M.A. & Bork, P. (1995): HEAT repeats in the Huntington's disease protein. *Nat. Genet.* **11**, 115-116.

Andrus, L., Szabo, P., Grady, R.W., Hanauske, A.R., Huima-Byron, T., Slowinska, B., Zagulska, S. & Hanauske-Abel, H.M. (1998): Antiretroviral effects of deoxyhypusyl hydroxylase inhibitors: A hypusine-dependent host cell mechanism for replication of human immunodeficiency virus type 1 (HIV-1). *Biochem. Pharmacol*. **55**, 1807-1818.

Atemnkeng, V.A., Pink, M., Schmitz-Spanke, S., Wu, X.J., Dong, L.L., Zhao, K.H., May, C., Laufer, S., Langer, B. & Kaiser, A. (2013): Deoxyhypusine hydroxylase from *Plasmodium vivax*, the neglected human malaria parasite: Molecular cloning, expression and specific inhibition by the 5-LOX inhibitor zileuton. *PLoS One* **8**, e58318.

Atkin, C.L., Thelander, L., Reichard, P. & Lang, G. (1973): Iron and free radical in ribonucleotide reductase. Exchange of iron and Mössbauer spectroscopy of the protein B2 subunit of the *Escherichia coli* enzyme. *J. Biol. Chem.* **248**, 7464-7472.

Bailey, L.J. & Fox, B.G. (2009): Crystallographic and catalytic studies of the peroxide-shunt reaction in a diiron hydroxylase. *Biochemistry* **48**, 8932-8939.

Balabanov, S., Gontarewicz, A., Ziegler, P., Hartmann, U., Kammer, W., Copland, M., Brassat, U., Priemer, M., Hauber, I., Wilhelm, T., Schwarz, G., Kanz, L., Bokemeyer, C., Hauber, J., Holyoake, T.L., Nordheim, A. & Brümmendorf, T.H. (2007): Hypusination of eukaryotic initiation factor 5A

(eIF5A): a novel therapeutic target in BCR-ABL-positive leukemias identified by a proteomics approach. *Blood* **109**, 1701-1711.

Baldwin, J., Krebs, C., Saleh, L., Stelling, M., Huynh, B.H., Bollinger, J.M. Jr. & Riggs-Gelasco, P. (2003): Structural characterization of the peroxodiiron(III) intermediate generated during oxygen activation by the W48A/D84E variant of ribonucleotide reductase protein R2 from *Escherichia coli*. *Biochemistry* **42**, 13269-13279.

Bartig, D., Schümann, H. & Klink, F. (1990): The unique posttranslational modification leading to deoxyhypusine or hypusine is a general feature of the archebacterial kingdom. *System Appl. Microbiol*. **13**, 112-116.

Battye, T.G., Kontogiannis, L., Johnson, O., Powell, H.R. & Leslie, A.G. (2011): *iMOSFLM*: a new graphical interface for diffraction-image processing with *MOSFLM*. *Acta Crystallogr. D Biol. Crystallogr.* **67**, 271-281.

Becke, A.D. (1988): Density-functional exchange-energy approximation with correct asymptotic-behavior. *Phys. Rev. A* **38**, 3098-3100.

Becke, A.D. (1993): A new mixing of hartree-fock and local density-functional theories. *J. Chem. Phys.* **98**, 1372-1377.

Behshad, E., Ruzicka, F.J., Mansoorabadi, S.O., Chen, D., Reed, G.H. & Frey, P.A. (2006): Enantiomeric free radicals and enzymatic control of stereochemistry in a radical mechanism: the case of lysine 2,3-aminomutases. *Biochemistry* **45**, 12639-12646.

Beninati, S., Nicolini, L., Jakus, J., Passeggio, A. & Abbruzzese, A. (1995): Identification of a substrate site for transglutaminases on the human protein synthesis initiation factor 5A. *Biochem. J.* **305**, 725-728.

Beninati, S., Gentile, V., Caraglia, M., Lentini, A., Tagliaferri, P. & Abbruzzese, A. (1998): Tissue transglutaminase expression affects hypusine metabolism in BALB/c 3T3 cells. *FEBS Lett.* **437**, 34-38.

Benne, R. & Hershey, J.W. (1978): The mechanism of action of protein synthesis initiation factors from rabbit reticulocytes. *J. Biol. Chem*. **253**, 3078-3087.

Bertini, I., Lalli, D., Mangani, S., Pozzi, C., Rosa, C., Theil, E.C. & Turano, P. (2012): Structural insights into the ferroxidase site of ferritins from higher eukaryotes. *J. Am. Chem. Soc.* **134**, 6169-6176.

Bevec, D., Jaksche, H., Oft, M., Wohl, T., Himmelspach, M., Pacher, A., Schebesta, M., Koettnitz, K., Dobrovnik, M., Csonga, R., Lottspeich, F. & Hauber, J. (1996): Inhibition of HIV-1 replication in lymphocytes by mutants of the Rev cofactor eIF-5A. *Science* **271**, 1858-1860.

Blaha, G., Stanley, R.E. & Steitz, T.A. (2009): Formation of the first peptide bond: The structure of EF-P bound to the 70S ribosome. *Science* **325**, 966-970.

Bochevarov, A.D., Li, J., Song, W.J., Friesner, R.A. & Lippard, S.J. (2011): Insights into the different dioxygen activation pathways of methane and toluene monooxygenase hydroxylases. *J. Am. Chem. Soc.* **133**, 7384-7397.

Bollinger, J.M. Jr. Edmondson, D.E., Huynh, B.H., Filley, J., Norton, J.R. & Stubbe, J. (1991): Mechanism of assembly of the tyrosyl radical-dinuclear iron cluster cofactor of ribonucleotide reductase. *Science* **253**, 292-298.

Bollinger, J.M. Jr., Krebs, C., Vicol, A., Chen, S., Ley, B.A., Edmondson, D.E. & Huynh, B.H. (1998): Engineering the diiron site of *Escherichia coli* ribonucleotide reductase protein R2 to accumulate an intermediate similar to H_{peroxo}, the putative peroxodiiron(III) complex from the methane monooxygenase catalytic cycle. *J. Am. Chem. Soc.* **120**, 1094-1095.

Bou-Abdallah, F., Papaefthymiou, G.C., Scheswohl, D.M., Stanga, S.D., Arosio, P. & Chasteen, N.D. (2002): *μ*-1,2-peroxobridged di-iron(III) dimer formation in human H-chain ferritin. *Biochem. J.* **364**, 57-63.

Bou-Abdallah, F., Zhao, G., Mayne, H.R., Arosio, P. & Chasteen, N.D. (2005): Origin of the unusual kinetics of iron deposition in human H-chain ferritin. *J. Am. Chem. Soc*. **127**, 3885-3893.

Broadwater, J.A., Ai, J., Loehr, T.M., Sanders-Loehr, J. & Fox, B.G. (1998): Peroxodiferric intermediate of stearoyl-acyl carrier protein Δ^9 desaturase: Oxidase reactivity during single turnover and implications for the mechanism of desaturation. *Biochemistry* **37**, 14664-14671

Broadwater, J.A., Achim, C., Münck, E. & Fox, B.G. (1999): Mössbauer studies of the formation and reactivity of a quasi-stable peroxo intermediate of stearoyl-acyl carrier protein Δ^9-desaturase. *Biochemistry* **38**, 12197-12204.

Brown, P.M., Caradoc-Davies, T.T., Dickson, J.M., Cooper, G.J., Loomes, K.M. & Baker, E.N. (2006): Crystal structure of a substrate complex of *myo*-inositol oxygenase, a di-iron oxygenase with a key role in inositol metabolism. *Proc. Natl. Acad. Sci. USA* **103**, 15032-15037.

Brünger, A.T. (1992): Free *R* value: a novel statistical quantity for assessing the accuracy of crystal structures. *Nature* **355**, 472-475.

Cano, V.S., Jeon, G.A., Johansson, H.E., Henderson, C.A., Park, J.H., Valentini, S.R., Hershey, J.W. & Park, M.H. (2008): Mutational analyses of human eIF5A-1 - Identification of amino acid residues critical for eIF5A activity and hypusine modification. *FEBS J*. **275**, 44-58.

Cano, V.S., Medrano, F.J., Park, M.H. & Valentini, S.R. (2010): Evidence for conformational changes in the yeast deoxyhypusine hydroxylase Lia1 upon iron displacement from its active site. *Amino Acids* **38**, 479-490.

Caraglia, M., Passeggio, A., Beninati, S., Leardi, A., Nicolini, L., Improta, S., Pinto, A., Bianco, A.R., Tagliaferri, P. & Abbruzzese, A. (1997): Interferon α_2 recombinant and epidermal growth factor modulate proliferation and hypusine synthesis in human epidermoid cancer KB cells. *Biochem. J.* **324**, 737-741.

Caraglia, M., Marra, M., Giuberti, G., D'Alessandro, A.M., Budillon, A., del Prete, S., Lentini, A., Beninati, S. & Abbruzzese, A. (2001): The role of eukaryotic initiation factor 5A in the control of cell proliferation and apoptosis. *Amino Acids* **20**, 91-104.

Caraglia, M., Marra, M., Giuberti, G., D'Alessandro, A.M., Baldi, A., Tassone, P., Venuta, S., Tagliaferri, P. & Abbruzzese, A. (2003): The eukaryotic initiation factor 5A is involved in the regulation of proliferation and apoptosis induced by interferon-α and EGF in human cancer cells. *J. Biochem.* **133**, 757-765.

Caraglia, M., Park, M.H., Wolff, E.C., Marra, M. & Abbruzzese, A. (2013): eIF5A isoforms and cancer: two brothers for two functions? *Amino Acids* **44**, 103-109.

Chatterjee, I., Gross, S.R., Kinzy, T.G. & Chen, K.Y. (2006): Rapid depletion of mutant eukaryotic initiation factor 5A at restrictive temperature reveals connections to actin cytoskeleton and cell cycle progression. *Mol. Genet. Genomics* **275**, 264-276.

Chawla, B., Kumar, R.R., Tyagi, N., Subramanian, G., Srinivasan, N., Park, M.H. & Madhubala, R. (2012): A unique modification of the eukaryotic initiation factor 5A shows the presence of the complete hypusine pathway in *Leishmania donovani*. *PLoS One* **7**, e33138.

Chen, W., Luo, J.H., Hua, W.F., Zhou, F.J., Lin, M.C., Kung, H.F., Zeng, Y.X., Guan, X.Y. & Xie, D. (2009): Overexpression of EIF-5A2 is an independent

predictor of outcome in patients of urothelial carcinoma of the bladder treated with radical cystectomy. *Cancer Epidemiol. Biomarkers Prev*. **18**, 400-408.

Chen, V.B., Arendall, W.B. 3rd., Headd, J.J., Keedy, D.A., Immormino, R.M., Kapral, G.J., Murray, L.W., Richardson, J.S. & Richardson, D.C. (2010): *MolProbity*: all-atom structure validation for macromolecular crystallography. *Acta Crystallogr. D Biol. Crystallogr.* **66**, 12-21.

Choi, Y.S., Zhang, H., Brunzelle, J.S., Nair, S.K. & Zhao, H. (2008): *In vitro* reconstitution and crystal structure of *p*-aminobenzoate N-oxygenase (AurF) involved in aureothin biosynthesis. *Proc. Natl. Acad. Sci. USA* **105**, 6858-6863.

Chung, S.I., Park, M.H., Folk, J.E. & Lewis, M.S. (1991): Eukaryotic initiation factor 5A: the molecular form of the hypusine-containing protein from human erythrocytes. *Biochim. Biophys. Acta* **1076**, 448-451.

Clement, P.M., Hanauske-Abel, H.M., Wolff, E.C., Kleinman, H.K. & Park, M.H. (2002): The antifungal drug ciclopirox inhibits deoxyhypusine and proline hydroxylation, endothelial cell growth and angiogenesis *in vitro*. *Int. J. Cancer*. **100**, 491-498.

Clement, P.C., Henderson, C.A., Jenkins, Z.A., Smit-McBride, Z., Wolff, E.C., Hershey, J.W.B., Park, M.H. & Johansson, H.E. (2003): Identification and characterization of eukaryotic initiation factor 5A-2. *Eur. J. Biochem*. **147**, 4254-4263.

Clement, P.M., Johansson, H.E., Wolff, E.C. & Park, M.H. (2006): Differential expression of eIF5A-1 and eIF5A-2 in human cancer cells. *FEBS J.* **273**, 1102-1114.

Cooper, H.L., Park, M.H. & Folk, J.E. (1982): Posttranslational formation of hypusine in a single major protein occurs generally in growing cells and is associated with activation of lymphocyte growth. *Cell* **29**, 791-797.

Cooper, H.L., Park, M.H., Folk, J.E., Safer, B. & Braverman, R. (1983): Identification of the hypusine-containing protein hy^+ as translation initiation factor eIF-4D. *Proc. Natl. Acad. Sci. USA* **80**, 1854-1857.

Corbett, M.C., Latimer, M.J., Poulos, T.L., Sevrioukova, I.F., Hodgson, K.O. & Hedman, B. (2007): Photoreduction of the active site of the metalloprotein putidaredoxin by synchrotron radiation. *Acta Crystallogr. D Biol. Crystallogr.* **63**, 951-960.

Coulter, E.D., Shenvi, N.V., Beharry, Z.M., Smith, J.J., Prickril, B.C. & Kurtz,

D.M. Jr. (2000): Rubrerythrin-catalyzed substrate oxidation by dioxygen and hydrogen peroxide. *Inorganica. Chimica. Acta* **297**, 231-241.

Cracchiolo, B.M., Heller, D.S., Clement, P.M., Wolff, E.C., Park, M.H. & Hanauske-Abel, H.M. (2004): Eukaryotic initiation factor 5A-1 (eIF5A-1) as a diagnostic marker for aberrant proliferation in intraepithelial neoplasia of the vulva. *Gynecol. Oncol*. **94**, 217-222.

Crichton, R.R. & Declercq, J.P. (2010): X-ray structures of ferritins and related proteins. *Biochim. Biophys. Acta* **1800**, 706-718.

Dassama, L.M., Silakov, A., Krest, C.M., Calixto, J.C., Krebs, C., Bollinger, J.M. Jr. & Green, M.T. (2013): A 2.8 Å Fe-Fe separation in the $Fe2^{III/IV}$ intermediate, X, from *Escherichia coli* ribonucleotide reductase. *J. Am. Chem. Soc.* **135**, 16758-16761.

Daugherty, M.D., Liu, B. & Frankel, A.D. (2010): Structural basis for cooperative RNA binding and export complex assembly by HIV Rev. *Nat. Struct. Mol. Biol*. **17**, 1337-1342.

Dawson, J.W., Gray, H.B., Hoenig, H.E., Rossman, G.R., Schredder, J.M. & Wang, R.H. (1972): A magnetic susceptibility study of hemerythrin using an ultrasensitive magnetometer. *Biochemistry* **11**, 461-465.

De Benedetti, A. & Harris, A.L. (1999): eIF4E expression in tumors: its possible role in progression of malignancies. *Int. J. Biochem*. *Cell Biol*. **31**, 59-72.

DeMaré, F., Kurtz, D.M. Jr. & Nordlund, P. (1996): The structure of *Desulfovibrio vulgaris* rubrerythrin reveals a unique combination of rubredoxin-like FeS_4 and ferritin-like diiron domains. *Nat. Struct. Biol.* **3**, 539-546.

DeWitt, J.G., Bentsen, J.G., Rosenzweig, A.C., Hedman, B., Green, J., Pilkington, S., Papaefthymiou, J.C., Dalton, H., Hodgson, K.O. & Lippard, S.J. (1991): X-ray absorption, Mössbauer, and EPR studies of the dinuclear iron center in the hydroxylase component of methane monooxygenase. *J. Am. Chem. Soc.* **113**, 9219-9235.

Dias, C.A., Gregio, A.P., Rossi, D., Galvão, F.C., Watanabe, T.F., Park, M.H., Valentini, S.R. & Zanelli, C.F. (2012): eIF5A interacts functionally with eEF2. *Amino Acids* **42**, 697-702.

Dias, C.A., Garciam W., Zanelli, C.F. & Valentini, S.R. (2013): eIF5A dimerizes not only *in vitro* but also *in vivo* and its molecular envelope is similar to the

EF-P monomer. *Amino Acids* **44**, 631-644.

Ding, F., Prutzman, K.C., Campbell, S.L. & Dokholyan, N.V. (2006): Topological determinants of protein domain swapping. *Structure* **14**, 5-14.

Doerfel, L.K., Wohlgemuth, I., Kothe, C., Peske, F., Urlaub, H. & Rodnina, M.V. (2013): EF-P is essential for rapid synthesis of proteins containing consecutive proline residues. *Science* **339**, 85-88.

Dong, Y., Yan, S., Young, V.G. Jr. & Que, L. Jr. (1996): Crystal structure analysis of a synthetic non-heme diiron-O_2 adduct: Insight into the mechanism of oxygen activation. *Angew. Chem. Int. Ed. Engl.* **35**, 618-620.

Dong, Z., Arnold, R.J., Yang, Y., Park, M.H., Hrncirova, P., Mechref, Y., Novotny, M.V. & Zhang, J.T. (2005): Modulation of differentiation-related gene 1 expression by cell cycle blocker mimosine, revealed by proteomic analysis. *Mol. Cell Proteomics* **4**, 993-1001.

Dunietz, B.D., Beachy, M.D., Cao, Y., Whittington, D.A., Lippard, S.J. & Friesner, R.A. (2000): Large scale ab initio quantum chemical calculation of the intermediates in the soluble methane monooxygenase catalytic cycle. *J. Am. Chem. Soc.* **122**, 2828-2839.

Dunn, J.B., Shriver, D.F. & Klotz, I.M. (1973): Resonance Raman studies of the electronic state of oxygen in hemerythrin. *Proc. Natl. Acad. Sci. USA* **70**, 2582-2584.

Ellis, M.J., Buffey, S.G., Hough, M.A. & Hasnain, S.S. (2008): On-line optical and X-ray spectroscopies with crystallography: An integrated approach for determining metalloprotein structures in functionally well defined states. *J. Synchrotron Radiat.* **15**, 433-439.

Emsley, P., Lohkamp, B., Scott, W.G. & Cowtan, K. (2010): Features and development of *Coot. Acta Crystallogr. D Biol. Crystallogr.* **66**, 486-501.

Evans, P. (2006): Scaling and assessment of data quality. *Acta Crystallogr. D Biol. Crystallogr.* **62**, 72-87.

Facchiano, A.M., Stiuso, P., Chiusano, M.L., Caraglia, M., Giuberti, G., Marra, M., Abbruzzese, A. & Colonna, G. (2001): Homology modelling of the human eukaryotic initiation factor 5A (eIF-5A). *Prot. Eng.* **14**, 881-890.

Fernandes, J., Jayaraman, B. & Frankel, A. (2012): The HIV-1 Rev response element: an RNA scaffold that directs the cooperative assembly of a

homo-oligomeric ribonucleoprotein complex. *RNA Biol*. **9**, 6-11.

Fiedler, A.T., Shan, X., Mehn, M.P., Kaizer, J., Torelli, S., Frisch, J.R., Kodera, M. & Que, L. Jr. (2008): Spectroscopic and computational studies of (*μ*-oxo)(*μ*-1,2-peroxo)diiron(III) complexes of relevance to nonheme diiron oxygenase intermediates. *J. Phys. Chem. A* **112**, 13037-13044.

Fox, B.G., Froland, W.A., Dege, J.E. & Lipscomb, J.D. (1989): Methane monooxygenase from *Methylosinus trichosporium* OB3b. Purification and properties of a three-component system with high specific activity from a type II methanotroph. *J. Biol. Chem.* **264**, 10023-10033.

Fox, B.G., Hendrich, M.P., Surerus, K.K., Andenson, K.K., Froland, W.A., Lipscomb, J.D. & Münck, E. (1993a): Mössbauer, EPR, and ENDOR studies of the hydroxylase and reductase components of methane monooxygenase from *Methylosinus trichosporium* OB3b. *J. Am. Chem. Soc.* **115**, 3688-3701.

Fox, B.G., Shanklin, J., Somerville, C. & Münck, E. (1993b): Stearoyl-acyl carrier protein Δ^9 desaturase from *Ricinus communis* is a diiron-oxo protein. *Proc. Natl. Acad. Sci. USA* **90**, 2486-2490.

Frisch, J.R., Vu, V.V., Martinho, M., Münck, E. & Que, L. Jr. (2009): Characterization of two distinct adducts in the reaction of a nonheme diiron(II) complex with O_2. *Inorg. Chem.* **48**, 8325-8336.

Frommholz, D., Kusch, P., Blavid, R., Scheer, H., Tu, J.M., Marcus, K., Zhao, K.H., Atemnkeng, V., Marciniak, J. & Kaiser, A.E. (2009): Completing the hypusine pathway in *Plasmodium*. *FEBS J.* **276**, 5881-5891.

Fukuchi-Shimogori, T., Ishii, I., Kashiwagi, K., Mashiba, H., Ekimoto, H. & Igarashi, K. (1997): Malignant transformation by overproduction of translation initiation factor eIF4G. *Cancer Res*. **57**, 5041-5044.

Gallagher, S.C., Cammack, R. & Dalton, H. (1997): Alkene monooxygenase from *Nocardia corallina* B-276 is a member of the class of dinuclear iron proteins capable of stereospecific epoxygenation reactions. *Eur. J. Biochem.* **247**, 635-641.

Gassner, G.T. & Lippard, S.J. (1999): Component interactions in the soluble methane monooxygenase system from *Methylococcus capsulatus* (Bath). *Biochemistry* **38**, 12768-12785.

Gentz, P.M., Blatch, G.L. & Dorrington, R.A. (2009): Dimerization of the yeast eukaryotic translation initiation factor 5A requires hypusine and is RNA

dependent. *FEBS J*. **276**, 695-706.

Gherman, B.F., Baik, M.H., Lippard, S.J. & Friesner, R.A. (2004): Dioxygen activation in methane monooxygenase: A theoretical study. *J. Am. Chem. Soc.* **126**, 2978-2990.

Glick, B.R. & Ganoza, M.C. (1975): Identification of a soluble protein that stimulates peptide bond synthesis. *Proc. Natl. Acad. Sci. USA* **72**, 4257-4260.

Goebel, T., Ulmer, D., Projahn, H., Kloeckner, J., Heller, E., Glaser, M., Ponte-Sucre, A., Specht, S., Sarite, S.R., Hoerauf, A., Kaiser, A., Hauber, I., Hauber, J. & Holzgrabe, U. (2008): In search of novel agents for therapy of tropical diseases and human immunodeficiency virus. *J. Med. Chem*. **51**, 238-250.

Gomes, C.M., Le Gall. J., Xavier, A.V. & Teixeira, M. (2001): Could a diiron-containing four-helix-bundle protein have been a primitive oxygen reductase? *Chembiochem*. **2**, 583-587.

Greganova, E., Altmann, M. & Bütikofer, P. (2011): Unique modifications of translation elongation factors. *FEBS J*. **278**, 2613-2624.

Gregio, A.P., Cano, V.P., Avaca, J.S., Valentini, S.R. & Zanelli, C.F. (2009): eIF5A has a function in the elongation step of translation in yeast. *Biochem. Biophys. Res. Commun*. **380**, 785-790.

Guan, X.Y., Sham, J.S., Tang, T.C., Fang, Y., Huo, K.K. & Yang, J.M. (2001): Isolation of a novel candidate oncogene within a frequently amplified region at 3q26 in ovarian cancer. *Cancer Res*. **61**, 3806-3809.

Guan, X.Y., Fung, J.M., Ma, N.F., Lau, S.H., Tai, L.S., Xie, D., Zhang, Y., Hu, L., Wu, Q.L., Fang, Y. & Sham, J.S. (2004): Oncogenic role of *eIF-5A2* in the development of ovarian cancer. *Cancer Res*. **64**, 4197-4200.

Gutierrez, E., Shin, B.S., Woolstenhulme, C.J., Kim, J.R., Saini, P., Buskirk, A.R. & Dever, T.E. (2013): eIF5A promotes translation of polyproline motifs. *Mol. Cell* **51**, 35-45.

Hanauske-Abel, H.M., Park, M.H., Hanauske, A.R., Popowicz, A.M., Lalande, M. & Folk, J.E. (1994): Inhibition of the G1-S transition of the cell cycle by inhibitors of deoxyhypusine hydroxylation. *Biochim. Biophys. Acta* **1221**, 115-124.

Hanauske-Abel, H.M., Slowinska, B., Zagulska, S., Wilson, R.C.,

Staiano-Coico, L., Hanauske, A.R., McCaffrey, T. & Szabo, P. (1995): Detection of a sub-set of polysomal mRNAs associated with modulation of hypusine formation at the G1-S boundary. Proposal of a role for eIF-5A in onset of DNA replication. *FEBS Lett*. **366**, 92-98.

Hanawa-Suetsugu, K., Sekine, S., Sakai, H., Hori-Takemoto, C., Terada, T., Unzai, S., Tame, J.R., Kuramitsu, S., Shirouzu, M. & Yokoyama, S. (2004): Crystal structure of elongation factor P from *Thermus thermophilus* HB8. *Proc. Natl. Acad. Sci. USA* **101**, 9595-9600.

Hauber, J. (2010): Revisiting an old acquaintance: role for eIF5A in diabetes. *J. Clin. Invest.* **120**, 1806-1808.

Hauber, I., Bevec, D., Heukeshoven, J., Krätzer, F., Horn, F., Choidas, A., Harrer, T. & Hauber, J. (2005): Identification of cellular deoxyhypusine synthase as a novel target for antiretroviral therapy. *J. Clin. Invest.* **115**, 76-85.

Hausinger, R.P. (2004): Fe(II)/α-ketoglutarate-dependent hydroxylases and related enzymes. *Crit. Rev. Biochem. Mol. Biol*. **39**, 21-68.

Henderson, A. & Hershey, J.W. (2011a): The role of eIF5A in protein synthesis. *Cell Cycle* **10**, 3617-3618.

Henderson, A. & Hershey, J.W. (2011b): Eukaryotic translation initiation factor (eIF) 5A stimulates protein synthesis in *Saccharomyces cerevisiae*. *Proc. Natl. Acad. Sci. USA* **108**, 6415-6419.

Hofmann, W., Reichart, B., Ewald, A., Müller, E., Schmitt, I., Stauber, R.H., Lottspeich, F., Jockusch, B.M., Scheer, U., Hauber, J. & Dabauvalle, M.C. (2001): Cofactor requirements for nuclear export of Rev response element (RRE)- and constitutive transport element (CTE)-containing retroviral RNAs: An unexpected role for actin. *J. Cell Biol.* **152**, 895-910.

Högbom, M., Galander, M., Andersson, M., Kolberg, M., Hofbauer, W., Lassmann, G., Nordlund, P. & Lendzian, F. (2003): Displacement of the tyrosyl radical cofactor in ribonucleotide reductase obtained by single-crystal high-field EPR and 1.4-Å X-ray data. *Proc. Natl. Acad. Sci. USA* **100**, 3209-3214.

Holmes, M.A., Trong, I.L., Turley, S., Sieker, L.C. & Stenkamp, R.E. (1991): Structures of deoxy and oxy hemerythrin at 2.0 Å resolution. *J. Mol. Biol.* **218**, 583-593.

Hommes, D., van den Blink, B., Plasse, T., Bartelsman, J., Xu, C., Macpherson,

B., Tytgat, G., Peppelenbosch, M. & van Deventer, S. (2002): Inhibition of stress-activated MAP kinases induces clinical improvement in moderate to severe Crohn's disease. *Gastroenterology* **122**, 7-14.

Hoque, M., Hanauske-Abel, H.M., Palumbo, P., Saxena, D., D'Alliessi-Gandolfi, D., Park, M.H., Pe'ery, T. & Mathews, M.B. (2009): Inhibition of HIV-1 gene expression by ciclopirox and deferiprone, drugs that prevent hypusination of eukaryotic initiation factor 5A. *Retrovirology* **6**, 90.

Huang, J.K., Cui, Y., Chen, C.H., Clampitt, D., Lin, C.T. & Wen, L. (2007): Molecular cloning and functional expression of bovine deoxyhypusine hydroxylase cDNA and homologs. *Protein Expr. Purif.* **54**, 126-133.

Hwang, J., Krebs, C., Huynh, B.H., Edmondson, D.E., Theil, E.C. & Penner-Hahn, J.E. (2000): A short Fe-Fe distance in peroxodiferric ferritin: Control of Fe substrate *versus* cofactor decay? *Science* **287**,122-125.

Ignatenko, N.A., Yerushalmi, H.F., Pandey, R., Kachel, K.L., Stringer, D.E., Marton, L.J. & Gerner, E.W. (2009): Gene expression analysis of HCT116 colon tumor-derived cells treated with the polyamine analog PG-11047. *Cancer Genomics Proteomics* **6**, 161-175.

Jasiulionis, M.G., Luchessi, A.D., Moreira, A.G., Souza, P.P., Suenaga, A.P., Correa, M., Costa, C.A., Curi, R. & Costa-Neto, C.M. (2007): Inhibition of eukaryotic translation initiation factor 5A (eIF5A) hypusination impairs melanoma growth. *Cell Biochem. Funct.* **25**, 109-114.

Jenkins, Z.A., Haag, P.G. & Johansson, H.E. (2001): Human *EIF5A2* on chromosome 3q25–q27, is a phylogenetically conserved vertebrate variant of eukaryotic translation initiation factor 5A with tissue-specific expression. *Genomics* **71**, 101-109.

Jensen, K.P., Bell, C.B. 3rd, Clay, M.D. & Solomon, E.I. (2009): Peroxo-type intermediates in class I ribonucleotide reductase and related binuclear non-heme iron enzymes. *J. Am. Chem. Soc.* **131**, 12155-12171.

Joe, Y.A. & Park, M.H. (1994): Structural features of the eIF-5A precursor required for posttranslational synthesis of deoxyhypusine. *J. Biol. Chem*. **269**, 25916-25921.

Kaiser, A. (2012): Translational control of eIF5A in various diseases. *Amino Acids* **42**, 679-684.

Kang, H.A. & Hershey, J.W. (1994): Effect of initiation factor eIF-5A depletion

on protein synthesis and proliferation of *Saccharomyces cerevisiae*. *J. Biol. Chem.* **269**, 3934-3940.

Kang, K.R., Wolff, E.C., Park, M.H., Folk, J.E. & Chung, S.I. (1995): Identification of *YHR068w* in *Saccharomyces cerevisiae* chromosome VIII as a gene for deoxyhypusine synthase. Expression and characterization of the enzyme. *J. Biol. Chem.* **270**, 18408-18412.

Kang, K.R., Kim, Y.S., Wolff, E.C. & Park, M.H. (2007): Specificity of the deoxyhypusine hydroxylase - eukaryotic translation initiation factor (eIF5A) interaction. *J. Biol. Chem.* **282**, 8300-8308.

Karplus, P.A. & Diederichs, K. (2012): Linking crystallographic model and data quality. *Science* **336**, 1030-1033.

Katona, G., Carpentier, P., Nivière, V., Amara, P., Adam, V., Ohana, J., Tsanov, N. & Bourgeois, D. (2007): Raman-assisted crystallography reveals end-on peroxide intermediates in a nonheme iron enzyme. *Science* **316**, 449-453.

Kemper, W.M., Berry, K.W. & Merrick, W.C. (1976): Purification and properties of rabbit reticulocyte protein synthesis initiation factors M2Bα and M2Bβ. *J. Biol. Chem.* **251**, 5551-5557.

Khara, B., Menon, N., Levy, C., Mansell, D., Das, D., Marsh, E.N., Leys, D. & Scrutton, N.S. (2013): Production of propane and other short-chain alkanes by structure-based engineering of ligand specificity in aldehyde-deformylating oxygenase. *Chembiochem.* **14**, 1204-1208.

Kim, K. & Lippard, S.J. (1996): Structure and Mössbauer spectrum of a (*μ*-1,2-peroxo)bis(*μ*-carboxylato)diiron(III) model for the peroxo intermediate in the methane monooxygenase hydroxylase reaction cycle. *J. Am. Chem. Soc.* **118**, 4914-4915.

Kim, K.K., Hung, L.W., Yokota, H., Kim, R. & Kim, S.H. (1998): Crystal structures of eukaryotic translation initiation factor 5A from *Methanococcus jannaschii* at 1.8 Å resolution. *Proc. Natl. Acad. Sci. USA* **95**, 10419-10424.

Kim, Y.S., Kang, K.R., Wolff, E.C., Bell, J.K., McPhie, P. & Park M.H. (2006): Deoxyhypusine hydroxylase is a Fe(II)-dependent, HEAT-repeat enzyme. Identification of amino acid residues critical for Fe(II) binding and catalysis. *J. Biol. Chem*. **281**, 13217-13225.

Klotz, I.M. & Kurtz, D.M. Jr, (1984): Binuclear oxygen carriers: hemerythrin. *Acc. Chem. Res.* **17**, 16-22.

Korboukh, V.K., Li, N., Barr, E.W., Bollinger, J.M. Jr. & Krebs, C. (2009): A long-lived, substrate-hydroxylating peroxodiiron(III/III) intermediate in the amine oxygenase, AurF, from *Streptomyces thioluteus*. *J. Am. Chem. Soc.* **131**, 13608-13609.

Kovaleva EG, Neibergall MB, Chakrabarty S, Lipscomb JD. (2007): Finding intermediates in the O_2 activation pathways of non-heme iron oxygenases. *Acc. Chem. Res.* **40**, 475-483.

Krebs, C., Bollinger, J.M. Jr., Theil, E.C. & Huynh, B.H. (2002): Exchange coupling constant *J* of peroxodiferric reaction intermediates determined by Mössbauer spectroscopy. *J. Biol. Inorg. Chem.* **7**, 863-869.

Krebs, C., Bollinger, J.M. Jr. & Booker, S J. (2011): Cyanobacterial alkane biosynthesis further expands the catalytic repertoire of the ferritin-like “di-iron-carboxylate” proteins. *Curr. Opin. Chem. Biol.* **15**, 291-303.

Krissinel, E. & Henrick, K. (2007): Inference of macromolecular assemblies from crystalline state. *J. Mol. Biol.* **372**, 774-797.

Krug, M., Weiss, M.S., Heinemann, U. & Mueller, U. (2012) *XDSAPP*: a graphical user interface for the convenient processing of diffraction data using XDS. *J. Appl. Cryst*. **45**, 568-572.

Kruse, M., Rosorius, O., Krätzer, F., Bevec, D., Kuhnt, C., Steinkasserer, A., Schuler, G. & Hauber, J. (2000): Inhibition of CD83 cell surface expression during dendritic cell maturation by interference with nuclear export of CD83 mRNA. *J. Exp. Med.* **191**, 1581-1590.

Kurtz, D.M. Jr. (1990): Oxo- and hydroxo-bridged diiron complexes: A chemical perspective on a biological unit. *Chem. Rev.* **90**, 585-606.

Kurtz, D.M. Jr. (2006): Avoiding high-valent iron intermediates: Superoxide reductase and rubrerythrin. *J. Inorg. Biochem.* **100**, 679-693.

Kyrpides, N.C. & Woese, C.R. (1998): Universally conserved translation initiation factors. *Proc. Natl. Acad. Sci. USA* **95**, 224-228.

Laskowski, R.A., MacArthur, M.W., Moss, D.S. & Thornton, J.M. (1993): *PROCHECK*: a program to check the stereochemical quality of protein structures. *J. Appl. Cryst.* **26**, 283-291.

Lee, C.T., Yang, W.T. & Parr, R.G. (1988) Development of the colle-salvetti

correlation-energy formula into a functional of the electron-density. *Phys. Rev. B* **37**, 785-789.

Lee, S.K., Nesheim, J.C. & Lipscomb, J.D. (1993a): Transient intermediates of the methane monooxygenase catalytic cycle. *J. Biol. Chem.* **268**, 21569-21577.

Lee, S.K., Fox, B.G., Froland, W.A., Lipscomb, J.D. & Miinck, E. (1993b) A transient intermediate of the methane monooxygenase catalytic cycle containing an $Fe^{IV}Fe^{IV}$ cluster. *J. Am. Chem. Soc.* **115**, 6450-6451.

Lee, S.K. & Lipscomb, J.D. (1999): Oxygen activation catalyzed by methane monooxygenase hydroxylase component: proton delivery during the O-O bond cleavage steps. *Biochemistry* **38**, 4423-4432.

Lee, Y.B., Joe, Y.A., Wolff, E.C., Dimitriadis, E.K. & Park, M.H. (1999): Complex formation between deoxyhypusine synthase and its protein substrate, the eukaryotic translation initiation factor 5A (eIF5A) precursor. *Biochem. J.* **340**, 273-281.

Lee N.P., Tsang F.H., Shek F.H., Mao M., Dai H., Zhang C., Dong S., Guan X.Y., Poon R.T. & Luk J.M. (2010): Prognostic significance and therapeutic potential of eukaryotic translation initiation factor 5A (eIF5A) in hepatocellular carcinoma. *Int. J. Cancer* **127**, 968-976.

Lee, S.J., McCormick, M.S., Lippard, S.J. & Cho, U.S. (2013): Control of substrate access to the active site in methane monooxygenase. *Nature* **494**, 380-384.

Leist, M., Single, B., Naumann, H., Fava, E., Simon, B., Kuhnle, S. & Nicotera, P. (1999): Inhibition of mitochondrial ATP generation by nitric oxide switches apoptosis to necrosis. *Exp. Cell Res.* **249**, 396-403.

Li, C.H., Ohn, T., Ivanov, P., Tisdale, S. & Anderson, P. (2010): eIF5A promotes translation elongation, polysome disassembly and stress granule assembly. *PLoS One* **5**, e9942.

Liao, D.I., Wolff, E.C., Park, M.H. & Davies, D.R. (1998): Crystal structure of the NAD complex of human deoxyhypusine synthase: an enzyme with a ball-and-chain mechanism for blocking the active site. *Structure* **6**, 23-32.

Lindqvist, Y., Huang, W., Schneider, G. & Shanklin, J. (1996): Crystal structure of Δ^9 stearoyl-acyl carrier protein desaturase from castor seed and its relationship to other di-iron proteins. *EMBO J.* **15**, 4081-4092.

Lipowsky, G., Bischoff, F.R., Schwarzmaier, P., Kraft, R., Kostka, S., Hartmann, E., Kutay, U. & Gorlich, D. (2000): Exportin-4: a mediator of a novel nuclear export pathway in higher eukaryotes. *EMBO J*. **19**, 4362-4371.

Liu, K.E., Wang, D., Huynh, B.H., Edmondson, D.E., Salifoglou, A. & Lippard, S.J. (1994): Spectroscopic detection of intermediates in the reaction of dioxygen with the reduced methane monooxygenase/hydroxylase from *Methylococcus capsulatus* (Bath). *J. Am. Chem. Soc.* **116**, 7465-7466.

Liu, K.E., Valentine, A.M., Qiu, D., Edmondson, D.E., Appelman, E.H., Spiro, T.G. & Lippard, S.J. (1995a): Characterization of a diiron(III) peroxide intermediate in the reaction cycle of methane monooxygenase hydroxylase from *Methylococcus capsulatus* (Bath). *J. Am. Chem. Soc.* **117**, 4997-4998.

Liu, K.E., Valentine, A.M., Wang, D.L., Huynh, B.H., Edmondson, D.E., Salifoglou, A. & Lippard, S.J. (1995b): Kinetic and spectroscopic characterization of intermediates and component interactions in reactions of methane monooxygenase from *Methylococcus capsulatus* (Bath). *J. Am. Chem. Soc.* **117**, 10174-10185.

Liu, Y.P., Nemeroff, M., Yan, Y.P. & Chen, K.Y. (1997): Interaction of eukaryotic initiation factor 5A with the human immunodeficiency virus type 1 Rev response element RNA and U6 snRNA requires deoxyhypusine or hypusine modification. *Biol. Signals* **6**, 166-174.

Liu, J., Henao-Mejia, J., Liu, H., Zhao, Y. & He, J.J. (2011): Translational regulation of HIV-1 replication by HIV-1 Rev cellular cofactors Sam68, eIF5A, hRIP, and DDX3. *J. Neuroimmune Pharmacol.* **6**, 308-321.

Maeda, I., Kohara, Y., Yamamoto, M. & Sugimoto, A. (2001): Large-scale analysis of gene function in *Caenorhabditis elegans* by high-throughput RNAi. *Curr. Biol*. **11**, 71-176.

Magdolen, V., Klier, H., Wöhl, T., Klink, F., Hirt, H., Hauber, J. & Lottspeich, F. (1994): The function of the hypusine-containing proteins of yeast and other eukaryotes is well conserved. *Mol. Gen. Genet.* **244**, 646-652.

Maier, B., Tersey, S.A. & Mirmira, R.G. (2010a): Hypusine: a new target for therapeutic intervention in diabetic inflammation. *Discov. Med.* **10**, 18-23.

Maier, B., Ogihara, T., Trace, A.P., Tersey, S.A., Robbins, R.D., Chakrabarti, S.K., Nunemaker, C.S., Stull, N.D., Taylor, C.A., Thompson, J.E., Dondero, R.S., Lewis, E.C., Dinarello, C.A., Nadler, J.L. & Mirmira, R.G. (2010b): The

unique hypusine modification of eIF5A promotes islet β cell inflammation and dysfunction in mice. *J. Clin. Invest.* **120**, 2156-2170.

Mandal, A., Mandal, S. & Park, M.H. (2014): Genome-wide analyses and functional classification of proline repeat-rich proteins: Potential role of eIF5A in eukaryotic evolution. *PLoS One* **9**, e111800.

McCormick, M.S., Sazinsky, M.H., Condon, K.L. & Lippard, S.J. (2006): X-ray crystal structures of manganese(II)-reconstituted and native toluene/o-xylene monooxygenase hydroxylase reveal rotamer shifts in conserved residues and an enhanced view of the protein interior. *J. Am. Chem. Soc.* **128**, 15108-15110.

McCormick, M.S. & Lippard, S.J. (2011): Analysis of substrate access to active sites in bacterial multicomponent monooxygenase hydroxylases: X-ray crystal structure of xenon-pressurized phenol hydroxylase from *Pseudomonas sp*. OX1. *Biochemistry* **50**, 11058-11069.

Meents, A., Reime, B., Stuebe, N., Fischer, P., Warmer, M., Goeries, D., Roever, J., Meyer, J., Fischer, J., Burkhardt, A., Vartiainen, I., Karvinen, P. & David, C. (2013): Development of an in-vacuum X-ray microscope with cryogenic sample cooling for beamline P11 at PETRA III. *Proc. SPIE* 8851, 88510K.

Mehta, K.D., Leung, D., Lefebvre, L. & Smith, M. (1990): The *ANB1* locus of *Saccharomyces cerevisiae* encodes the protein synthesis initiation factor eIF-4D. *J. Biol. Chem*. **265**, 8802-8807.

Mémin, E., Hoque, M., Jain, M.R., Heller, D.S., Li, H., Cracchiolo, B., Hanauske-Abel, H.M., Pe'ery, T. & Mathews, M.B. (2014): Blocking eIF5A modification in cervical cancer cells alters the expression of cancer-related genes and suppresses cell proliferation. *Cancer Res*. **74**, 552-562.

Mittal, N., Subramanian, G., Bütikofer, P. & Madhubala, R. (2013): Unique posttranslational modifications in eukaryotic translation factors and their roles in protozoan parasite viability and pathogenesis. *Mol. Biochem. Parasitol.* **187**, 21-31.

Moënne-Loccoz, P., Baldwin, J., Ley, B.A., Loehr, T.M. & Bollinger, J.M. Jr. (1998): O_2 activation by non-heme diiron proteins: Identification of a symmetric *μ*-1,2-peroxide in a mutant of ribonucleotide reductase. *Biochemistry* **37**, 14659-14663.

Moënne-Loccoz, P., Krebs, C., Herlihy, K., Edmondson, D.E., Theil, E.C., Huynh, B.H. & Loehr, T.M. (1999): The ferroxidase reaction of ferritin reveals a

diferric *μ*-1,2 bridging peroxide intermediate in common with other O_2-activating non-heme diiron proteins. *Biochemistry* **38**, 5290-5295.

Monecke, T., Güttler, T., Neumann, P., Dickmanns, A., Görlich, D. & Ficner, R. (2009): Crystal structure of the nuclear export receptor CRM1 in complex with Snurportin1 and RanGTP. *Science* **324**, 1087-1091.

Morris, G.M., Huey, R., Lindstrom, W., Sanner, M.F., Belew, R.K., Goodsell, D.S. & Olson, A.J. (2009): Autodock4 and AutoDockTools4: automated docking with selective receptor flexiblity. *J. Comput. Chem.* **30**, 2785-2791.

Mueller, U., Darowski, N., Fuchs, M.R., Förster, R., Hellmig, M., Paithankar, K.S., Pühringer, S., Steffien, M., Zocher, G. & Weiss, M.S. (2012): Facilities for macromolecular crystallography at the Helmholtz-Zentrum Berlin. *J. Synchrotron Rad.* **19**, 442-449.

Murphey, R.J. & Gerner, E.W. (1987): Hypusine formation in protein by a two step process in cell lysates. *J. Biol. Chem.* **262**, 15033-15036.

Murray, L.J., Naik, S.G., Ortillo, D.O., García-Serres, R., Lee, J.K., Huynh, B.H. & Lippard, S.J. (2007): Characterization of the arene-oxidizing intermediate in ToMOH as a diiron(III) species. *J. Am. Chem. Soc.* **129**, 14500-14510.

Murshudov, G.N., Skubák, P., Lebedev, A.A., Pannu, N.S., Steiner, R.A., Nicholls, R.A., Winn, M.D., Long, F. & Vagin, A.A. (2011): *REFMAC5* for the refinement of macromolecular crystal structures. *Acta Crystallogr. D Biol. Crystallogr.* **67**, 355-367.

Neese, F. (2012): The *ORCA* program system. *Wiley Interdiscip. Rev. Comput. Mol. Sci.* **2**, 73-78.

Noodleman, L. (1981): Valence bond description of anti-ferromagnetic coupling in transition-metal dimers. *J. Chem. Phys.* **74**, 5737-5743.

Nordlund, P. & Eklund, H. (1995): Di-iron-carboxylate proteins. *Curr. Opin. Struct. Biol.* **5**, 758-766.

Ober, D. & Hartmann, T. (1999): Homospermidine synthase, the first pathway-specific enzyme of pyrrolizidine alkaloid biosynthesis, evolved from deoxyhypusine synthase. *Proc. Natl. Acad. Sci. USA* **96**, 14777-14782.

Ober, D., Harms, R., Witte, L. & Hartmann, T. (2003): Molecular evolution by change of function. Alkaloid-specific homospermidine synthase retained all properties of deoxyhypusine synthase except binding the eIF5A precursor

protein. *J. Biol. Chem.* **278**, 12805-12812.

Okamura, M.Y., Klotz, I.M., Johnson, C.E., Winter, M.R.C. & Williams, R.J.P. (1969): The state of iron in hemerythrin. A Mössbauer study. *Biochemistry* **8**, 1951-1958.

Ookubo, T., Sugimoto, H., Nagayama, T., Masuda, H., Sato, T., Tanaka, K., Maeda, Y., Ōkawa, H., Hayashi, Y., Uehara, A. & Suzuki, M. (1996): *cis-μ*-1,2-peroxo diiron complex: Structure and reversible oxygenation. *J. Am. Chem. Soc.* **118**, 701-702.

Pandelia, M.E., Li, N., Nørgaard, H., Warui, D.M., Rajakovich, L.J., Chang, W.C., Booker, S.J., Krebs, C. & Bollinger, J.M. Jr. (2013): Substrate-triggered addition of dioxygen to the diferrous cofactor of aldehyde-deformylating oxygenase to form a diferric-peroxide intermediate. *J. Am. Chem. Soc.* **135**, 15801-15812.

Panjikar, S., Parthasarathy, V., Lamzin, V.S., Weiss, M.S. & Tucker, P.A. (2005): *Auto-Rickshaw*: an automated crystal structure determination platform as an efficient tool for the validation of an X-ray diffraction experiment. *Acta Crystallogr. D Biol. Crystallogr.* **61**, 449-457.

Park, M.H. (2006): The post-translational synthesis of a polyamine-derived amino acid, hypusine, in the eukaryotic translation initiation factor 5A (eIF5A). *J. Biochem*. **139**, 161-169.

Park, M.H., Cooper, H.L. & Folk, J.E. (1981): Identification of hypusine, an unusual amino acid, in a protein from human lymphocytes and of spermidine as its biosynthetic precursor. *Proc. Natl. Acad. Sci. USA* **78**, 2869-2873.

Park, M.H., Cooper, H.L. & Folk, J.E. (1982): The biosynthesis of protein-bound hypusine (N^{ε}-(4-amino-2-hydroxybutyl)lysine). Lysine as the amino acid precursor and the intermediate role of deoxyhypusine (N^{ε}-(4-aminobutyl)lysine). *J. Biol. Chem*. **257**, 7217-7222.

Park, M.H., Joe, Y.A. & Kang, K.R. (1998): Deoxyhypusine synthase activity is essential for cell viability in the yeast *Saccharomyces cerevisiae*. *J. Biol. Chem*. **273**, 1677-1683.

Park, J.H., Wolff, E.C., Folk, J.E. & Park, M.H. (2003): Reversal of the deoxyhypusine synthesis reaction. Generation of spermidine or homospermidine from deoxyhypusine by deoxyhypusine synthase. *J. Biol. Chem*. **278**, 32683-32691.

Park, J.H., Aravind, L., Wolff, E.C., Kaevel, J., Kim, Y.S. & Park, M.H. (2006): Molecular cloning, expression, and structural prediction of deoxyhypusine hydroxylase: A HEAT-repeat-containing metalloenzyme. *Proc. Natl. Acad. Sci. USA* **103**, 51-56.

Park, M.H., Nishimura, K., Zanelli, C.F. & Valentini, S.R. (2010): Functional significance of eIF5A and its hypusine modification in eukaryotes. *Amino Acids* **38**, 491-500.

Patel, P.H., Costa-Mattiolo, M., Schulze, K.L. & Bellen, H.J. (2009): The *Drosophila* deoxyhypusine hydroxylase homologue *nero* and its target eIF5A are required for cell growth and the regulation of autophagy. *J. Cell. Biol.* **185**, 1181-1194.

Pavlov, M.Y., Watts, R.E., Tan, Z., Cornish, V.W., Ehrenberg, M. & Forster, A.C. (2009): Slow peptide bond formation by proline and other N-alkylamino acids in translation. *Proc. Natl. Acad. Sci. USA* **106**, 50-54.

Peil, L., Starosta, A.L., Virumäe, K., Atkinson, G.C., Tenson, T., Remme, J. & Wilson, D.N. (2012): Lys34 of translation elongation factor EF-P is hydroxylated by YfcM. *Nat. Chem. Biol*. **8**, 695-697.

Perdew, J.P. (1986): Density-functional approximation for the correlation-energy of the inhomogeneous electron-gas. *Phys. Rev. B* **33**, 8822-8824.

Pereira, A.S., Small, W., Krebs, C., Tavares, P., Edmondson, D.E., Theil, E.C. & Huynh, B.H. (1998): Direct spectroscopic and kinetic evidence for the involvement of a peroxodiferric intermediate during the ferroxidase reaction in fast ferritin mineralization. *Biochemistry* **37**, 9871-9876.

Pikus, J.D., Studts, J.M., Achim, C., Kauffmann, K.E., Münck, E., Steffan, R.J., McClay, K. & Fox, B.G. (1996): Recombinant toluene-4-monooxygenase: Catalytic and Mössbauer studies of the purified diiron and rieske components of a four-protein complex. *Biochemistry* **35**, 9106-9119.

Preukschas, M., Hagel, C., Schulte, A., Weber, K., Lamszus, K., Sievert, H., Pällmann, N., Bokemeyer, C., Hauber, J., Braig, M. & Balabanov, S. (2012): Expression of eukaryotic initiation factor 5A and hypusine forming enzymes in glioblastoma patient samples: Implications for new targeted therapies. *PLoS One* **7**, e43468.

Rinaldo, D., Philipp, D.M., Lippard, S.J. & Friesner, R.A. (2007): Intermediates in dioxygen activation by methane monooxygenase: A QM/MM study. *J. Am.*

Chem. Soc. **129**, 3135-3147.

Robbins, R.D., Tersey, S.A., Ogihara, T., Gupta, D., Farb, T.B., Ficorilli, J., Bokvist, K., Maier, B. & Mirmira, R.G. (2010): Inhibition of deoxyhypusine synthase enhances islet β cell function and survival in the setting of endoplasmic reticulum stress and type 2 diabetes. *J. Biol. Chem.* **285**, 39943-39952.

Rosenzweig, A.C., Frederick, C.A., Lippard, S.J. & Nordlund, P. (1993): Crystal structure of a bacterial non-haem iron hydroxylase that catalyses the biological oxidation of methane. *Nature* **366**, 537-543.

Rosorius, O., Reichart, B., Krätzer, F., Heger, P., Dabauvalle, M.C. & Hauber, J. (1999): Nuclear pore localization and nucleocytoplasmic transport of eIF-5A: Evidence for direct interaction with the export receptor CRM1. *J. Cell. Sci.* **112**, 2369-2380.

Rossi, D., Kuroshu, R., Zanelli, C.F. & Valentini, S.R. (2014): eIF5A and EF-P: two unique translation factors are now traveling the same road. *Wiley Interdiscip. Rev. RNA* **5**, 209-222.

Rossmann, M.G. (1990): The molecular replacement method. *Acta Crystallogr. A Foundations Crystallogr.* **46**, 73-82.

Ruggero, D. (2013): Translational control in cancer etiology. *Cold Spring Harb. Perspect. Biol.* **5**, a012336.

Ruhl, M., Himmelspach, M., Bahr, G.M., Hammerschmid, F., Jaksche, H., Wolff, B., Aschauer, H., Farrington, G.K., Probst, H., Bevec, D. & Hauber, J. (1993): Eukaryotic initiation factor 5A is a cellular target of the human immunodeficiency virus type 1 Rev activation domain mediating *trans*-activation. *J. Cell Biol.* **123**, 1309-1320.

Saini, P., Eyler, D.E., Green, R. & Dever, T.E. (2009): Hypusine-containing protein eIF5A promotes translation elongation. *Nature* **459**, 118-121.

Schäfer, A., Horn, H. & Ahlrichs, R. (1992): Fully optimized contracted gaussian-basis sets for atoms Li to Kr. *J. Chem. Phys*. **97**, 2571-2577.

Schäfer, A., Huber, C. & Ahlrichs, R. (1994): Fully optimized contracted gaussian-basis sets of triple zeta valence quality for atoms Li to Kr. *J. Chem. Phys*. **100**, 5829-5835.

Schatz, O., Oft, M., Dascher, C., Schebesta, M., Rosorius, O., Jaksche, H.,

Dobrovnik, M., Bevec, D. & Hauber, J. (1998): Interaction of the HIV-1 rev cofactor eukaryotic initiation factor 5A with ribosomal protein L5. *Proc. Natl. Acad. Sci. USA* **95**, 1607-1612.

Schnier, J., Schwelberger, H.G., Smit-McBride, Z., Kang, H.A. & Hershey, J.W. (1991): Translation initiation factor 5A and its hypusine modification are essential for viability in the yeast *Saccharomyces cerevisiae*. *Mol. Cell. Biol.* **11**, 3105-3114.

Schrader, R., Young, C., Kozian, D., Hoffmann, R. & Lottspeich, F. (2006): Temperature-sensitive eIF5A mutant accumulates transcripts targeted to the nonsense-mediated decay pathway. *J. Biol. Chem.* **281**, 35336-35346.

Schreier, M.H., Erni, B. & Staehelin, T. (1977): Initiation of mammalian protein synthesis. I. Purification and characterization of seven initiation factors. *J. Mol. Biol.* **116**, 727-753.

Schüttelkopf, A.W. & van Aalten, D.M. (2004): *PRODRG*: a tool for high-throughput crystallography of protein-ligand complexes. *Acta Crystallogr. D Biol. Crystallogr.* **60**, 1355-1363.

Scuoppo, C., Miething, C., Lindqvist, L., Reyes, J., Ruse, C., Appelmann, I., Yoon, S., Krasnitz, A., Teruya-Feldstein, J., Pappin, D., Pelletier, J. & Lowe, S.W. (2012): A tumour suppressor network relying on the polyamine-hypusine axis. *Nature* **487**, 244-248.

Shek, F.H., Fatima, S. & Lee, N.P. (2012): Implications of the use of eukaryotic translation initiation factor 5A (eIF5A) for prognosis and treatment of hepatocellular carcinoma. *Int. J. Hepatol.* Article ID 760928.

Shi, X.P., Yin, K.C., Ahern, J., Davis, L.J., Stern, A.M. & Waxman, L. (1996): Effects of N1-guanyl-1,7-diaminoheptane, an inhibitor of deoxyhypusine synthase, on the growth of tumorigenic cell lines in culture. *Biochim. Biophys. Acta* **1310**, 119-126.

Shiba, T., Mizote, H., Kaneko, T., Nakajima, T. & Kakimoto, Y. (1971): Hypusine, a new amino acid occurring in bovine brain. Isolation and structural determination. *Biochim. Biophys. Acta* **244**, 523-531.

Shu, L., Nesheim, J.C., Kauffmann, K., Münck, E., Lipscomb, J.D. & Que, L. Jr. (1997): An $Fe_2^{IV}O_2$ diamond core structure for the key intermediate Q of methane monooxygenase. *Science* **275**, 515-518.

Sievert, H., Pällmann, N., Miller, K.K., Hermans-Borgmeyer, I., Venz, S.,

Sendoel, A., Preukschas, M., Schweizer, M., Boettcher, S., Janiesch, P.C., Streichert, T., Walther, R., Hengartner, M.O., Manz, M.G., Brümmendorf, T.H., Bokemeyer, C., Braig, M., Hauber, J., Duncan, K.E. & Balabanov, S. (2014): A novel mouse model for inhibition of DOHH-mediated hypusine modification reveals a crucial function in embryonic development, proliferation and oncogenic transformation. *Dis. Model Mech.* **7**, 963-976.

Silvera, D., Formenti, S.C. & Schneider, R.J. (2010): Translational control in cancer. *Nat. Rev. Cancer* **10**, 254-266.

Skulan, A.J., Brunold, T.C., Baldwin, J., Saleh, L., Bollinger, J.M. Jr. & Solomon, E.I. (2004): Nature of the peroxo intermediate of the W48F/D84E ribonucleotide reductase variant: Implications for O_2 activation by binuclear non-heme iron enzymes. *J. Am. Chem. Soc.* **126**, 8842-8855.

Smit-McBride, Z., Dever, T.E., Hershey, J.W. & Merrick, W.C. (1989): Sequence determination and cDNA cloning of eukaryotic initiation factor 4D, the hypusine-containing protein. *J. Biol. Chem*. **264**, 1578-1583.

Solomon, E.I., Brunold, T.C., Davis, M.I., Kemsley, J.N., Lee, S.K., Lehnert, N., Neese, F., Skulan, A.J., Yang, Y.S. & Zhou, J. (2000): Geometric and electronic structure/function correlations in non-heme iron enzymes. *Chem. Rev.* **100**, 235-350.

Song, W.J., Behan, R.K., Naik, S.G., Huynh, B.H. & Lippard, S.J. (2009): Characterization of a peroxodiiron(III) intermediate in the T201S variant of toluene/o-xylene monooxygenase hydroxylase from *Pseudomonas* sp. OX1. *J. Am. Chem. Soc.* **131**, 6074-6075.

Song, W.J., McCormick, M.S., Behan, R.K., Sazinsky, M.H., Jiang, W., Lin, J., Krebs, C. & Lippard, S.J. (2010): Active site threonine facilitates proton transfer during dioxygen activation at the diiron center of toluene/o-xylene monooxygenase hydroxylase. *J. Am. Chem. Soc.* **132**, 13582-13585.

Song, W.J. & Lippard, S.J. (2011): Mechanistic studies of reactions of peroxodiiron(III) intermediates in T201 variants of toluene/*o*-xylene monooxygenase hydroxylase. *Biochemistry* **50**, 5391-5399.

Spradling, A.C., Stern, D., Beaton, A., Rhem, E.J., Laverty, T., Mozden, N., Misra, S. & Rubin, G.M. (1999): The Berkeley *Drosophila* genome project gene disruption project: Single *P*-element insertions mutating 25% of vital *Drosophila* genes. *Genetics* **153**, 135-177.

Steinkasserer, A., Jones, T., Sheer, D., Koettnitz, K., Hauber, J. & Bevec, D.

(1995): The eukaryotic cofactor for the human immunodeficiency virus type 1 (HIV-1) rev protein, eIF-5A, maps to chromosome 17p12-p13: three eIF-5A pseudogenes map to 10q23.3, 17q25, and 19q13.2. *Genomics* **25**, 749-752.

Stenkamp, R.E. (1994): Dioxygen and hemerythrin. *Chem. Rev.* **94**, 715-726.

Stephens, P.J. (1994): Ab-initio calculation of vibrational absorption and circular-dichroism spectra using density-functional force-fields. *J. Phys. Chem.* **98**, 11623-11627.

Sturgeon, B.E., Burdi, D., Chen, S., Huynh, B.H., Edmondson, D.E., Stubbe, J. & Hoffman, B.M. (1996): Reconsideration of X, the diiron intermediate formed during cofactor assembly in *E. coli* ribonucleotide reductase. *J. Am. Chem. Soc.* **118**, 7551-7557.

Suhasini, M. & Reddy, T.R. (2009): Cellular proteins and HIV-1 Rev function. *Curr. HIV Res*. **7**, 91-100.

Summa, C.M., Lombardi, A., Lewis, M. & DeGrado, W.F. (1999): Tertiary templates for the design of diiron proteins. *Curr. Opin. Struct. Biol.* **9**, 500-508.

Tang, D.J., Dong, S.S., Ma, N.F., Xie, D., Chen, L., Fu, L., Lau, S.H., Li, Y., Li, Y. & Guan, X.Y. (2010): Overexpression of eukaryotic initiation factor 5A2 enhances cell motility and promotes tumor metastasis in hepatocellular carcinoma. *Hepatology* **51**, 1255-1263.

Taylor, C.A., Liu, Z., Tang, T.C., Zheng, Q., Francis, S., Wang, T.W., Ye, B., Lust, J.A., Dondero, R. & Thompson, J.E. (2012): Modulation of eIF5A expression using SNS01 nanoparticles inhibits NF-*κ*B activity and tumor growth in murine models of multiple myeloma. *Mol. Ther*. **20**, 1305-1314.

Teng, Y.B., He, Y.X., Jiang, Y.L., Chen, Y.X. & Zhou, C.Z. (2009): Crystal structure of *Arabidopsis* translation initiation factor eIF-5A2. *Proteins* **77**, 736-740.

Thomas, A., Goumans, H., Amesz, H., Benne, R. & Voorma, H.O. (1979): A comparison of the initiation factors of eukaryotic protein synthesis from ribosomes and from the postribosomal supernatant. *Eur. J. Biochem*. **98**, 329-337.

Thompson, G.M., Cano, V.S. & Valentini, S.R. (2003): Mapping eIF5A binding sites for Dys1 and Lia1: *In vivo* evidence for regulation of eIF5A hypusination. *FEBS Lett*. **555**, 464-468.

Tinberg, C.E. & Lippard, S.J. (2009): Revisiting the mechanism of dioxygen activation in soluble methane monooxygenase from *M. capsulatus* (Bath): Evidence for a multi-step, proton-dependent reaction pathway. *Biochemistry* **48**, 12145-12158.

Tinberg, C.E. & Lippard, S.J. (2010): Oxidation reactions performed by soluble methane monooxygenase hydroxylase intermediates H_{peroxo} and Q proceed by distinct mechanisms. *Biochemistry* **49**, 7902-7912.

Tome, M.E. & Gerner, E.W. (1997): Cellular eukaryotic initiation factor 5A content as a mediator of polyamine effects on growth and apoptosis. *Neurosignals* **6**, 150-156.

Tong, W.H., Chen, S., Lloyd, S.G., Edmondson, D.E., Huynh, B.H. & Stubbe, J. (1996): Mechanism of assembly of the diferric cluster−tyrosyl radical cofactor of *Escherichia coli* ribonucleotide reductase from the diferrous form of the R2 subunit. *J. Am. Chem. Soc.* **118**, 2107-2108.

Tong, Y., Park, I., Hong, B.S., Nedyalkova, L., Tempel, W. & Park, H.W. (2009): Crystal structure of human eIF5A1: Insight into functional similarity of human eIF5A1 and eIF5A2. *Proteins* **75**, 1040-1045.

Toussaint, L., Bertrand, L., Hue, L., Crichton, R.R. & Declercq, J.P. (2007). High-resolution X-ray structures of human apoferritin H-chain mutants correlated with their activity and metal-binding sites. *J. Mol. Biol.* **365**, 440-52.

Treffry, A., Zhao, Z., Quail, M.A., Guest, J.R. & Harrison, P.M. (1995): Iron(II) oxidation by H chain ferritin: Evidence from site-directed mutagenesis that a transient blue species is formed at the dinuclear iron center. *Biochemistry* **34**, 15204-15213.

Ude, S., Lassak, J., Starosta, A.L., Kraxenberger, T., Wilson, D.N. & Jung, K. (2013): Translation elongation factor EF-P alleviates ribosome stalling at polyproline stretches. *Science* **339**, 82-85.

Umland, T.C., Wolff, E.C., Park, M.H. & Davies, D.R. (2004): A new crystal structure of deoxyhypusine synthase reveals the configuration of the active enzyme and of an enzyme·NAD·inhibitor ternary complex. *J. Biol. Chem.* **279**, 28697-28705.

Vagin, A. & Teplyakov, A. (1997): *MOLREP*: an automated program for molecular replacement. *J. Appl. Crystallogr.* **30**, 1022-1025.

Valentini, S.R., Casolari, J.M., Oliveira, C.C., Silver, P.A. & McBride, A.E.

(2002): Genetic interactions of yeast eukaryotic translation initiation factor 5A (eIF5A) reveal connections to poly(A)-binding protein and protein kinase C signaling. *Genetics* **160**, 393-405.

Voegtli, W.C., Khidekel, N., Baldwin, J., Ley, B.A., Bollinger, J.M. Jr. & Rosenzweig, A.C. (2000): Crystal structure of the ribonucleotide reductase R2 mutant that accumulates a *μ*-1,2-peroxodiiron(III) intermediate during oxygen activation. *J. Am. Chem. Soc.* **122**, 3255-3261.

von Koschitzky, I. & Kaiser, A. (2013): Chemical profiling of deoxyhypusine hydroxylase inhibitors for antimalarial therapy. *Amino Acids* **45**, 1047-1053.

Vonrhein, C., Flensburg, C., Keller, P., Sharff, A., Smart, O., Paciorek, W., Womack, T. & Bricogne, G. (2011): Data processing and analysis with the *autoPROC* toolbox. *Acta Crystallogr. D Biol. Crystallogr.* **67**, 293-302.

Vu, V.V., Emerson, J.P., Martinho, M., Kim, Y.S., Münck, E., Park, M.H. & Que L. Jr. (2009): Human deoxyhypusine hydroxylase, an enzyme involved in regulating cell growth, activates O_2 with a nonheme diiron center. *Proc. Natl. Acad. Sci. USA* **106**, 14814-14819.

Wallar, B.J. & Lipscomb, J.D. (1996): Dioxygen activation by enzymes containing binuclear non-heme iron clusters. *Chem. Rev.* **96**, 2625-2658.

Walsh, C.T., Garneau-Tsodikova. S. & Gatto, G.J. (2005): Protein posttranslational modifications: The chemistry of proteome diversifications. *Angew. Chem. Int. Ed. Engl.* **44**, 7342-7372.

Wang, F.W., Guan, X.Y. & Xie, D. (2013) Roles of eukaryotic initiation factor 5A2 in human cancer. *Int. J. Biol. Sci.* **9**, 1013-1020.

Weiss, M.S. & Hilgenfeld, R. (1997): On the use of the merging *R* factor as a quality indicator for X-ray data. *J. Appl. Cryst.* **30**, 203-205.

Wöhl, T., Klier, H. & Ammer, H. (1993): The *HYP2* gene of *Saccharomyces cerevisiae* is essential for aerobic growth: Characterization of different isoforms of the hypusine-containing protein Hyp2p and analysis of gene disruption mutants. *Mol. Gen. Genet.* **241**, 305-311.

Wolff, E.C., Park, M.H. & Folk, J.E. (1990): Cleavage of spermidine as the first step in deoxyhypusine synthesis. The role of NAD. *J. Biol. Chem.* **265**, 4793-4799.

Wolff, E.C., Lee, Y.B., Chung, S.I., Folk, J.E. & Park, M.H. (1995):

Deoxyhypusine synthase from rat testis: purification and characterization. *J. Biol. Chem.* **270**, 8660-8666.

Wolff, E.C., Folk, J.E. & Park, M.H. (1997): Enzyme-substrate intermediate formation at lysine 329 of human deoxyhypusine synthase. *J. Biol. Chem.* **272**, 15865-15871.

Wolff, E.C., Wolff, J. & Park, M.H. (2000): Deoxyhypusine synthase generates and uses bound NADH in a transient hydride transfer mechanism. *J. Biol. Chem.* **275**, 9170-9177.

Wolff, E.C., Kang, K.R., Kim, Y.S. & Park, M.H. (2007): Posttranslational synthesis of hypusine: evolutionary progression and specificity of the hypusine modification. *Amino Acids* **33**, 341-350.

Woolstenhulme, C.J., Parajuli, S., Healey, D.W., Valverde, D.P., Petersen, E.N., Starosta, A.L., Guydosh, N.R., Johnson, W.E., Wilson, D.N. & Buskirk, A.R. (2013): Nascent peptides that block protein synthesis in bacteria. *Proc. Natl. Acad. Sci. USA* **110**, E878-E887.

Xie, D., Ma, N.F., Pan, Z.Z., Wu, H.X., Liu, Y.D., Wu, G.Q., Kung, H.F. & Guan, X.Y. (2008): Overexpression of EIF-5A2 is associated with metastasis of human colorectal carcinoma. *Hum. Pathol.* **39**, 80-86.

Xu, A. & Chen, K.Y. (2001): Hypusine is required for a sequence-specific interaction of eukaryotic initiation factor 5A with postsystematic evolution of ligands by exponential enrichment RNA. *J. Biol. Chem.* **276**, 2555-2561.

Xu, A., Jao, D.L. & Chen, K.Y. (2004): Identification of mRNA that binds to eukaryotic initiation factor 5A by affinity co-purification and differential display. *Biochem. J.* **384**, 585-590.

Xue, G., Fiedlera, A.T., Martinho, M., Münck, E. & Que, L. Jr. (2008): Insights into the P-to-Q conversion in the catalytic cycle of methane monooxygenase from a synthetic model system. *Proc. Natl. Acad. Sci. USA* **105**, 20615-20620.

Yanagisawa, T., Sumida, T., Ishii, R., Takemoto, C. & Yokoyama, S. (2010): A paralog of lysyl-tRNA synthetase aminoacylates a conserved lysine residue in translation elongation factor P. *Nat. Struct. Mol. Biol.* **17**, 1136-1143.

Yang, G.F., Xie, D., Liu, J.H., Luo, J.H., Li, L.J., Hua, W.F., Wu, H.M., Kung, H.F., Zeng, Y.X. & Guan, X.Y. (2009): Expression and amplification of *eIF-5A2* in human epithelial ovarian tumors and overexpression of EIF-5A2 is a new independent predictor of outcome in patients with ovarian carcinoma. *Gynecol.*

Oncol. **112**, 314-318.

Yao, M., Ohsawa, A., Kikukawa, S., Tanaka, I. & Kimura, M. (2003): Crystal structure of hyperthermophilic archaeal initiation factor 5A: A homologue of eukaryotic initiation factor 5A (eIF-5A). *J. Biochem.* **133**, 75-81.

Zanelli, C.F. & Valentini, S.R. (2007): Is there a role for eIF5A in translation? *Amino Acids* **33**, 351-358.

Zender, L., Xue, W., Zuber, J., Semighini, C.P., Krasnitz, A., Ma, B., Zender, P., Kubicka, S., Luk, J.M., Schirmacher, P., McCombie, W.R., Wigler, M., Hicks, J., Hannon, G.J., Powers, S. & Lowe, S.W. (2008): An oncogenomics-based in *vivo* RNAi screen identifies tumor suppressors in liver cancer. *Cell* **135**, 852-864.

Zhang, X., Furutachi, H., Fujinami, S., Nagatomo, S., Maeda, Y., Watanabe, Y., Kitagawa, T. & Suzuki, M. (2005): Structural and spectroscopic characterization of (*μ*-hydroxo or *μ*-oxo)(*μ*-peroxo) diiron(III) complexes: Models for peroxo intermediates of non-heme diiron proteins. *J. Am. Chem. Soc.* **127**, 826-827.

Ziegler, P., Chahoud, T., Wilhelm, T., Pällman, N., Braig, M., Wiehle, V., Ziegler, S., Schröder, M., Meier, C., Kolodzik, A., Rarey, M., Panse, J., Hauber, J., Balabanov, S. & Brümmendorf, T.H. (2012): Evaluation of deoxyhypusine synthase inhibitors targeting BCR-ABL positive leukemias. *Invest. New Drugs* **30**, 2274-2283.

Zuk, D. & Jacobson, A. (1998): A single amino acid substitution in yeast eIF-5A results in mRNA stabilization. *EMBO J.* **17**, 2914-2925.

6. Acknowledgements

The first person that I should mention here is my supervisor Prof. Dr. rer. nat. Dr. h.c. Rolf Hilgenfeld who gave me the opportunity to work and study in Lübeck. I cannot forget his preciseness on science and excellent lectures (Biochemistry II, Rational Drug Design, and Anti-microbial Therapy and Prophylaxis). I appreciate his supports and cares in my work and life in Germany.

I also give many thanks to my group leader Dr. Naoki Sakai who gave me help on crystallography.

Equally important, I appreciate the helps and suggestions from my colleagues in Lübeck: Dr. Daizong Lin, Doris Mutschall, Friedrich Kohlmann, Hans-Joachim Kraus, Janica Meine, Dr. Jeroen R. Mesters, Dr. Jian Lei, Dr. Jinzhi Tan, Caroline Haase, Linlin Zhang, Dr. Margret Schwab, Petra Rosenfeld, Dr. Qingjun Ma, Raffaele Ciriello, Dr. Sebastián Klinke, Dr. Shuai Chen, Silke Schmidtke, Prof. Dr. Stefan Anemüller, Dr. Yibei Xiao.

I specially thank Prof. Alfred X. Trautwein and Dr. Lars H. Böttger (Institute of Physics, University of Lübeck) for providing the precious ^{57}Fe foil and performing the Mössbauer spectra and density function theory studies. I also thank Prof. Joachim Hauber and Prof. Annette Kaiser for providing the DNA materials used in this thesis.

Finally, I appreciate the supports from my parents, parents-in-law and two most important people in my life: my wife Huijuan Hu and my daughter Yumo Han (nickname: Ji-ling, German name: Greta). I LOVE YOU.

Zhenggang Han

Lübeck, 2015